Kinetics of Disorder→Order Transformations in Highly Nonequilibrium Materials

Thesis by

Lawrence Anthony

In Partial Fulfillment of the Requirements
for the Degree of
Doctor of Philosophy

California Institute of Technology
Pasadena, California

1993

(Submitted 24 May 1993)

for my parents

Acknowledgments

It gives me great pleasure to acknowledge the guidance and support of my advisor, Brent Fultz. It is also a pleasure to acknowledge collaborative discussions with Professor Ryo Kikuchi as part of the MITI/NEDO collaboration. My first contact with Professor Kikuchi, however, came when I sent him a preliminary write-up of my work using the master equation method in the point approximation (Section 2.1). He wrote back asking me why I was not using his path probability method instead. The reader may assess for himself the success of my attempt to address his criticism in the work carried out using the path probability method in the pair approximation (Section 2.2). Being a junior member of the MITI/NEDO collaboration proved to be especially valuable as it brought me into personal contact with the top researchers in the field. In particular, Professors Tetsuo Mohri and Juan Sanchez offered valuable advice and suggestions during the nascent development of the hybrid Monte Carlo–cluster variation method (Chapter 4).

I must also acknowledge Carol Garland and Channing Ahn for their selfless assistance and guidance in the use of the Transmission Electron Microscopy facility in Keck. That no high resolution or analytical microscopy results made it into this thesis is my fault entirely. Special words of thanks and appreciation go to my office mate Tab Stephens, who put up my idiosyncrasies.

The research described in this thesis was supported by the United States Department of Energy under contract DE–FG03–86ER45270. Additional support was provided by a Grant for International Research from the Ministry of Trade and Industry, Japan. I am also grateful to the Charles Lee Powell Foundation and the California Institute of Technology for additional financial support during my graduate tenure.

Abstract

Of late, there has been need for rigorous first-principles theoretical considerations of materials that are far removed from equilibrium. This is especially true as nonequilibrium materials of all shapes (*e.g.*, thin film structures) and sizes (*e.g.*, nanocrystalline composites) gain ever-increasing technological importance. To this end, the main contribution of this dissertation is to the study of the kinetics of disorder→order transformations in highly nonequilibrium binary alloys, specifically body-centered cubic alloys exhibiting B2, $D0_3$, and/or B32 order at equilibrium. This study takes several independent approaches. Chapter 2 presents two analytical methods. The first of these, a master equation method, is formulated in the Bragg-Williams or point approximation. The second analytical technique employs the path probability method of Kikuchi in the Bethe or pair approximation. Chapter 3 employs kinetic Monte Carlo simulations instead. Apart from the presentation of individual results using these three different techniques, the thermodynamic and kinetic trends exhibited by these different approaches are compared and discussed. One of the more compelling features exhibited by all three of these diverse approaches is the appearance, during ordering, of certain well-developed transient states, which do not persist at equilibrium, *e.g.*, the transient appearance of B2 order during ordering in an alloy that exhibits equilibrium B32 order. These transient states are discussed within the context of *pseudostability*. Central to the notion of pseudostability is the concept of a free energy

surface or manifold in order parameter space. While it is quite straightforward to obtain a closed-form, analytical (albeit approximate) expression for the configurational entropy and free energy in the master equation method and the path probability method, there is no simple, direct means of obtaining the same in the kinetic Monte Carlo simulations. Chapter 4 seeks to remedy this limitation of the Monte Carlo method and introduces a hybrid Monte Carlo–cluster variation method approach to order-disorder kinetics. This method is used to reexamine some of the results of Chapter 3 in the context of the time evolution of the free energy. Chapter 5 summarizes the results of the preceeding chapters and suggests avenues for further investigation.

List of Publications

Parts of this thesis have been or will be published under the following titles:

Chapter 2

L. Anthony, "A kinetic path theory of B2 and $D0_3$ ordering," The Minerals, Metals, and Materials Society Outstanding Student Paper Award Winner (1989).

L. Anthony and B. Fultz, "Kinetic paths of B2 and $D0_3$ order parameters: Theory," *J. Mater. Res.* **4**, 1132 (1989).

L. Anthony and B. Fultz, "Kinetics of B2 and $D0_3$ ordering: Theory," in *Alloy Phase Stability and Design*, edited by G. M. Stocks, D. P. Pope, and A. F. Giamei, *Mater. Res. Soc. Symp. Proc.* **186**, 181 (Materials Research Society, Pittsburgh, Pennsylvania, 1991).

L. Anthony and B. Fultz, "Kinetics of B2, $D0_3$, and B32 ordering: Results from pair approximation calculations and Monte Carlo simulations," *J. Mater. Res.*, submitted.

Chapter 3

B. Fultz and L. Anthony, "Suppression of vacancy diffusion during short-range ordering," in *Diffusion in High Technology Materials*, edited by D. Gupta, A. D. Romig, Jr., and M. A. Dayananda, (The Minerals, Metals, and Materials Society, Warrendale, Pennsylvania, 1988).

B. Fultz and L. Anthony, "Vacancy trapping on lattices with different coordination numbers," *Philos. Mag. Lett.* **59**, 237 (1989).

L. Anthony and B. Fultz, "Kinetics of B2 and $D0_3$ ordering: Theory," in *Alloy Phase Stability and Design*, edited by G. M. Stocks, D. P. Pope, and A. F. Giamei, *Mater. Res. Soc. Symp. Proc.* **186**, 181 (Materials Research Society, Pittsburgh, Pennsylvania, 1991).

L. Anthony and B. Fultz, "Kinetics of B2, $D0_3$, and B32 ordering: Results from pair approximation calculations and Monte Carlo simulations," *J. Mater. Res.*, submitted.

Chapter 4

L. Anthony and B. Fultz, "CVM-based free energy estimates in Monte Carlo simulations," in *Diffusion in ordered alloys*, edited by B. Fultz, R. W. Cahn, and D. Gupta (The Minerals, Metals and Materials Society, Warrendale, Pennsylvania, 1993).

L. Anthony and B. Fultz, "Cluster variation method based free energy estimates in Monte Carlo kinetics," in preparation for submission to *J. Mater. Res.*

Chapter 5

L. Anthony, "Kinetics of long-range ordering in Fe_3Al," The Minerals, Metals, and Materials Society Outstanding Student Paper Award Winner (1988).

L. Anthony and B. Fultz, "Kinetic paths of B2 and $D0_3$ order parameters: Experiment," *J. Mater. Res.* **4**, 1140 (1989).

B. Fultz, Z. Q. Gao, and L. Anthony, "Kinetics of ordering in Fe_3Al: Experiment," in *Alloy Phase Stability and Design*, edited by G. M. Stocks, D. P. Pope, and A. F. Giamei, *Mater. Res. Soc. Symp. Proc.* **186**, 187 (Materials Research Society, Pittsburgh, Pennsylvania, 1991).

Publications based on research carried out by the author during his graduate tenure at Caltech but not directly related to the subject of this thesis are listed below:

C. W. Nieh, L. Anthony, J. Y. Josefowicz, and F. G. Krajenbrink, "Microstructure of epitaxial $YBa_2Cu_3O_{7-x}$ thin films," *Appl. Phys. Lett.* **56**, 2138 (1990).

L. Anthony, J. K. Okamoto, and B. Fultz, "Vibrational entropy of ordered and disordered Ni_3Al," *Phys. Rev. Lett.* **70**, 1128 (1993).

Contents

Acknowledgments **iv**

Abstract **vi**

List of Publications **viii**

List of Figures **xiv**

List of Tables **xxi**

1 Introduction **1**

1.1 A Brief History of the Study of Nonequilibrium Thermodynamics and Kinetics 2

1.2 Spinodal Decomposition 5

1.3 Stability, Metastability, and Instability 14

1.4 Pseudostability 18

References 24

2 Analytical Theories of Disorder→Order Transformations **27**

2.1 The Master Equation Method in the Point Approximation 27

2.1.1 Introduction 28

2.1.2 Theory 29

2.1.3 Numerical Computations 40

2.1.4 Results and Discussion 41

2.1.5 Conclusions 61

2.2 The Path Probability Method in the Pair Approximation 62

2.2.1 Introduction 63

2.2.2 Theory 64

2.2.3 Results and Discussion 72

Kinetic and Thermodynamic Trends 72

Transient B32 and B2 order 77

2.2.4 Conclusions 79

References 80

3 Monte Carlo Simulations of Disorder→Order Transformations 82

3.1 Introduction 83

3.2 Theory 84

3.3 Results and Discussion 86

3.3.1 Kinetic and Thermodynamic Trends 86

3.3.2 Transient B32 and B2 order 89

3.4 Conclusions 96

References 99

4 The Hybrid Monte Carlo–Cluster Variation Method 100

4.1 The Cluster Variation Method 104

4.1.1 The Cluster Configurational Entropy 105

4.1.2 Computer Calculation of Cluster Entropy Expressions . . . 108

4.2 The Choice of Base Clusters 111

4.3 The Hybrid Monte Carlo–Cluster Variation Method 111

4.4 Results and Discussion 114

4.5 Conclusions 122

References 123

5 Summary and Perspective **125**

5.1 Comparison of Analytical and Monte Carlo Results 125

5.2 Experimental Evidence 127

5.2.1 Temperature Dependence of Kinetic Paths in Fe_3Al 127

5.2.2 Transient B32 Order in Fe_3Al 131

5.3 Future Efforts 133

References 137

List of Figures

1.1 Helmholtz free energy F as a function of composition c at some temperature T for a mixture exhibiting phase separation. 6

1.2 Excess Helmholtz free energy F as a function of composition ρ for a fixed value of $\frac{J}{k_BT}$ for the two-dimensional triangular lattice Ising model. The results shown are for the pair, 1-triangle, and 3-triangle approximations as well as the exact solution. 8

1.3 $T_{\mathrm{pb}} - T_{\mathrm{s}}$ as a function of $\frac{1}{n+1}$ for $M = 0.80$ and $M = 0.85$, where T_{pb} is the temperature corresponding to the phase boundary, T_{s} is the temperature corresponding to the spinodal point, n is the number of triangles in the cluster approximation, and M is the magnetization. 10

1.4 Excess Helmholtz free energy F as a function of composition ρ for the two-dimensional triangular lattice Ising model. The results shown are for the pair, 1-triangle, and 3-triangle approximations as well as the exact solution. The lower and upper sets of curves represent the excess free energy before and after a high temperature (T_{h}) to low temperature (T_{l}) quench, respectively. 13

1.5 The work W required for the formation of a spherical nucleus of radius r. 16

1.6 Helmholtz free energy F as a function of composition c at some temperature T for a system exhibiting a stationary point of inflection. 19

1.7 Contour plot of the free energy function in the pair approximation for a binary equiatomic bcc alloy exhibiting B2 order (left) with the main features of the the free energy surface indicated (right). The random disordered state is labeled 'D', the absolute (global) minima by 'm1' and 'm2', the absolute maximum by 'M', and the saddle point by 'P'. 20

2.1 The four fcc sublattices of the bcc lattice (left) and the interconnections between them (right). The arrows indicate the possible interchanges of an atom and a vacancy among these sublattices. . 32

2.2 The B2 (top), $D0_3$ (middle), and B32 (bottom) structures for a binary bcc alloy of composition AB_3. 33

2.3 The ground state structures for binary bcc alloys of composition AB_3 (top) and AB (bottom). 34

2.4 Kinetic path of an initially disordered alloy exhibiting B2 ordering ($V^1_{\mathrm{AA}} = V^1_{\mathrm{BB}} = V^2_{\mathrm{AA}} = 0.90$; $T = 0.74T_c^{\mathrm{B2}} = 1.11T_c^{\mathrm{D0_3}}$). The end-points of the i–j curves are our best estimates of the equilibrium end-points. The values of k and l decreased to near zero at equilibrium. 42

2.5 Kinetic path of an initially disordered alloy exhibiting B2 and $D0_3$ ordering ($V^1_{\mathrm{AA}} = V^1_{\mathrm{BB}} = V^2_{\mathrm{AA}} = 1.10$; $T = 0.61T_c^{\mathrm{B2}} = 0.91T_c^{\mathrm{D0_3}}$). The end-points of the i–j curves are our best estimates of the equilibrium end-points. The values of k and l decreased to near zero at equilibrium. 43

2.6 Kinetic paths exhibiting the transition from initial B2 ordering to initial D0$_3$ ordering. Labels indicate values of V^1_{BB} ($V^1_{\mathrm{AA}} = V^2_{\mathrm{AA}} = 1.60$; $V^1_{\mathrm{BB}} = 0.40 \Rightarrow T = 1.21T_c^{\mathrm{B2}} = 0.70T_c^{\mathrm{D0_3}}$; $V^1_{\mathrm{BB}} = 1.20 \Rightarrow T = 0.53T_c^{\mathrm{B2}} = 0.61T_c^{\mathrm{D0_3}}$). See text for further explanation. 46

2.7 Kinetic paths depicting the dependence of the relative rates of B2 and D0$_3$ ordering on temperature. Labels indicate values of V, where $V \equiv V^1_{\mathrm{AA}} = 2V^1_{\mathrm{BB}} = V^2_{\mathrm{AA}}$ ($V = 1.40 \Rightarrow T = 0.84T_c^{\mathrm{B2}} = 0.76T_c^{\mathrm{D0_3}}$; $V = 1.60 \Rightarrow T = 0.74T_c^{\mathrm{B2}} = 0.67T_c^{\mathrm{D0_3}}$; $V = 1.80 \Rightarrow T = 0.65T_c^{\mathrm{B2}} = 0.59T_c^{\mathrm{D0_3}}$; $V = 2.00 \Rightarrow T = 0.59T_c^{\mathrm{B2}} = 0.54T_c^{\mathrm{D0_3}}$). 48

2.8 Critical potentials for B2 and D0$_3$ order as a function of V^2_{AA}/V, where $V^1_{\mathrm{AA}} = V^1_{\mathrm{BB}} \equiv V$. The dashed parts of the curves for V_c(B2) indicate the critical potentials at which incipient B2 ordering occurs *without simultaneous* D0$_3$ ordering. 50

2.9 Critical potentials for B2 and D0$_3$ order as a function of V^1_{BB}/V, where $V^1_{\mathrm{AA}} = V^2_{\mathrm{AA}} \equiv V$. The dashed parts of the curves for V_c(B2) indicate the critical potentials at which incipient B2 ordering occurs *without simultaneous* D0$_3$ ordering. 51

2.10 Evolution of B2, D0$_3$, and B32 order parameters ($V^1_{\mathrm{AA}} = V^2_{\mathrm{AA}} = 1.60$; $T = 3.38T_c^{\mathrm{B2}} = 0.67T_c^{\mathrm{D0_3}}$). 52

2.11 Evolution of the internal energy, configurational entropy, and the free energy for the system of Fig. 2.10 ($V^1_{\mathrm{AA}} = V^2_{\mathrm{AA}} = 1.60$; $T = 3.38T_c^{\mathrm{B2}} = 0.67T_c^{\mathrm{D0_3}}$). 54

2.12 Surface plot of the free energy as a function of i and k for the system of Fig. 2.10 ($V^1_{\mathrm{AA}} = V^2_{\mathrm{AA}} = 1.60$; $T = 3.38T_c^{\mathrm{B2}} = 0.67T_c^{\mathrm{D0_3}}$). 55

2.13 Contour plot of the free energy as a function of i and k for the system of Fig. 2.10 ($V^1_{\mathrm{AA}} = V^2_{\mathrm{AA}} = 1.60$; $T = 3.38T_c^{\mathrm{B2}} = 0.67T_c^{\mathrm{D0_3}}$). 56

2.14 Evolution of B2, $D0_3$, and B32 order parameters ($V^1_{\mathrm{AA}} = V^2_{\mathrm{AA}} = 1.60$; $T = 3.38T_c^{\mathrm{B2}} = 0.67T_c^{\mathrm{D0_3}}$ for the first 10 000 steps and $V^1_{\mathrm{AA}} = V^2_{\mathrm{AA}} = 0.00$; $T = \infty$ thereafter). 59

2.15 Evolution of the internal energy, configurational entropy, and the free energy for the system of Fig. 2.14 ($V^1_{\mathrm{AA}} = V^2_{\mathrm{AA}} = 1.60$; $T = 3.38T_c^{\mathrm{B2}} = 0.67T_c^{\mathrm{D0_3}}$ for the first 10 000 steps and $V^1_{\mathrm{AA}} = V^2_{\mathrm{AA}} = 0.00$; $T = \infty$ thereafter). 60

2.16 Critical potentials V_c^{B2} and $V_c^{\mathrm{D0_3}}$ at the AB_3 stoichiometry as a function of V^2_{AA}/V, where $V \equiv V^1_{\mathrm{AA}} = V^1_{\mathrm{BB}}$, for two different kinetic models: a. point approximation and b. pair approximation. 73

2.17 Kinetic paths depicting the temperature-dependence of order evolution in $(S_{\mathrm{D0_3}}, S_{\mathrm{B2}})$-space at the AB_3 stoichiometry. Curves were obtained using the pair approximation. Labels indicate values of V, where $V \equiv V^1_{\mathrm{AA}} = V^1_{\mathrm{BB}} = \frac{4}{3}V^2_{\mathrm{AA}}$ ($V^2_{\mathrm{AA}}/V = 0.75$). 76

2.18 Time dependence of B2, $D0_3$, and B32 order parameters obtained using the pair approximation at the AB_3 stoichiometry ($V^1_{\mathrm{AA}} = V^2_{\mathrm{AA}} = 1.60$). 78

3.1 Critical potentials V_c^{B2} and $V_c^{\mathrm{D0_3}}$ at the AB_3 stoichiometry as a function of V^2_{AA}/V, where $V \equiv V^1_{\mathrm{AA}} = V^1_{\mathrm{BB}}$, for three different kinetic models: a. point approximation, b. pair approximation, and c. Monte Carlo simulation. 87

3.2 Time dependence of $D0_3$ and B32 order parameters obtained using Monte Carlo simulation at the AB_3 (1 : 3) stoichiometry ($V^1_{\mathrm{AA}} = V^1_{\mathrm{BB}} = 1.00$, $V^2_{\mathrm{AA}} = 2.00$). The curves were obtained from the integrated intensities of the ($\frac{1}{2}\frac{1}{2}\frac{1}{2}$) and (100) superlattice peaks and the (110) fundamental peak using Eqs. 3.3 – 3.5 90

3.3 Time dependence of B2 and B32 order parameters obtained using Monte Carlo simulation at the AB (1 : 1) stoichiometry ($V^1_{\mathrm{AA}} = V^1_{\mathrm{BB}} = 1.00$, $V^2_{\mathrm{AA}} = 1.40$). The curves were obtained from the integrated intensities of the ($\frac{1}{2}\frac{1}{2}\frac{1}{2}$) and (100) superlattice peaks and the (110) fundamental peak using Eqs. 3.6 and 3.7 91

3.4 Surface plot of [110] zone axis diffraction pattern obtained from the Monte Carlo simulated lattice of Fig. 3.3 at 0 Monte Carlo steps. 92

3.5 Surface plot of [110] zone axis diffraction pattern obtained from the Monte Carlo simulated lattice of Fig. 3.3 at 300 Monte Carlo steps. 93

3.6 Surface plot of [110] zone axis diffraction pattern obtained from the Monte Carlo simulated lattice of Fig. 3.3 at 3000 Monte Carlo steps. 94

3.7 Maximum quantity of transient and equilibrium order as a function of $\frac{V^2}{V^1}$ obtained using Monte Carlo simulations at the AB (1 : 1) stoichiometry ($V^1_{\mathrm{AA}} = V^1_{\mathrm{BB}} = 1.00$, V^2_{AA} variable). The curves were obtained from the integrated intensities of the ($\frac{1}{2}\frac{1}{2}\frac{1}{2}$) and (100) superlattice peaks and the (110) fundamental peak using Eqs. 3.6 and 3.7 97

4.1 A portion of the bcc lattice showing (from left to right) the a) point, b) pair, c) tetrahedron, d) octahedron, and e) cube clusters. . . . 112

4.2 Graph showing the growth of the (100) superlattice diffraction intensity (diamonds) as a function of Monte Carlo step for an initially disordered equiatomic binary alloy with $V^1_{\mathrm{AA}} = V^1_{\mathrm{BB}} = 1.00$ (in units of $k_B T$). Also shown, on the same horizontal axis, are the point (solid line), tetrahedron (dotted line), octa-hedron (dashed line), and octahedron–cube (dotted dashed line) approximations to the free energy density (in units of $k_B T$). 116

4.3 Graph showing the variation of the $(\frac{1}{2}\frac{1}{2}\frac{1}{2})$ (circles) and (100) (diamonds) superlattice diffraction intensities as a function of Monte Carlo step for an initially disordered equiatomic binary alloy with $V^1_{\mathrm{AA}} = V^1_{\mathrm{BB}} = 1.00$; $V^2_{\mathrm{AA}} = V^2_{\mathrm{BB}} = 0.70$ (in units of $k_B T$). Also shown, on the same horizontal axis, is the octahedron–cube (dotted dashed line) approximation to the free energy density (in units of $k_B T$). 118

4.4 Graph showing the variation of the $(\frac{1}{2}\frac{1}{2}\frac{1}{2})$ (circles) and (100) (diamonds) superlattice diffraction intensities as well as the octahedron–cube (dotted dashed line) approximation to the free energy density (in units of $k_B T$) as a function of Monte Carlo step. The data were obtained under conditions identical to those of Fig. 4.3 except that 8 independent simulations were performed using a crystal lattice $\frac{1}{8}$ the size of that in Fig. 4.3 , and their results averaged. 121

5.1 Dependence of kinetic paths through $(S_{\mathrm{D0}_3}, S_{\mathrm{B2}})$ order parameter space on annealing temperature for initially disordered Fe_3Al powders. Lines shown are linear fits to data obtained at a given temperature [2] 130

5.2 Growth of the $(\frac{1}{2}\frac{1}{2}\frac{1}{2})$ (left) and (100) (right) superlattice diffraction peaks in an initially piston-anvil quenched foil of Fe_3Al annealed at 300 °C for various lengths of time [4] 132

5.3 Hyperfine magnetic field distributions for Fe_3Al foils as piston-anvil quenched and after annealing at 300 °C for various lengths of time. The numbers at the top of the figure identify resonances from ^{57}Fe atoms with different numbers of Al neighbors [4] 134

List of Tables

2.1 Glossary of terms. 31

2.2 The path variables for a point. Unless it is stated otherwise, $\zeta \in \{\alpha, \beta, \gamma, \delta\}$ and $i \in \{0, 1, 2\}$. 67

2.3 The path variables for a pair. Unless it is stated otherwise, $(\zeta, \eta) \in \{(\alpha, \gamma), (\alpha, \delta), (\beta, \gamma), (\beta, \delta)\}$, $i \in \{0, 1, 2\}$, and $j \in \{0, 1, 2\}$. 68

Chapter 1

Introduction

Einstein is reputed to have remarked that if any one branch of physics would stand the test of time, it would be equilibrium thermodynamics. The intervening years have largely justified that bold statement. The foundations of equilibrium thermodynamics have withstood the ever-increasing sophistication of experiments designed to test them. If anything, the field has grown in strength and stature with such milestones as Onsager's tour-de-force solution [1] of the two-dimensional rectangular lattice Ising [2] model and Wilson's application of the renormalization group to the study of critical phenomena [3,4]. There is just one thing wrong with this rosy picture. Many technologically important materials are *not* in thermodynamic equilibrium!

This is not to say that there have been no efforts in the study of nonequilibrium thermodynamics and statistical physics. However the traditional emphasis on equilibrium systems has resulted in kinetic studies being somewhat neglected. This is further exacerbated by the fact that including time-dependent effects greatly increases the complexity of the system being studied. As such, many early theoretical efforts at treating nonequilibrium systems did not stray far from the relative security of well-established results in equilibrium thermodynamics. For instance, one of the early forays into nonequilibrium thermodynamics was

Onsager's linear response theory [5–7], which considered external perturbations sufficiently weak as to justify a linear approximation to their effects. In contrast, many of the systems of interest in materials science today are in states that are far removed from equilibrium, where we would not expect linear response theory to hold. It is one of the theses of this dissertation that a first-principles (inherently nonlinear) approach is essential for the proper treatment of the kinetics of such far-from-equilibrium systems.

The main contribution of this dissertation is to the study of the kinetics of disorder→order transformations in highly nonequilibrium binary alloys. These efforts take the form of analytical approaches (Chapter 2) as well as the more brute-force Monte Carlo method (Chapter 3). In addition, I will introduce a third approach (Chapter 4) which is a synthesis of the two approaches mentioned previously. In the present introductory chapter, I will set the stage by briefly reviewing various concepts in equilibrium and nonequilibrium thermodynamics of relevance to the points raised in the chapters to come. These concepts will serve as a useful framework within which to discuss (Chapter 5) the core results of the three central chapters.

1.1 A Brief History of the Study of Nonequilibrium Thermodynamics and Kinetics

As mentioned previously, one of the earliest attempts at treating nonequilibrium thermodynamics was linear response theory [5–7], which arose out of the consideration of fluctuations in equilibrium thermodynamic systems [8–10]. The theory of fluctuations enables us to express the fluctuation in a particular thermodynamic quantity in terms of the relevant extensive and intensive variables of the system under study. Perhaps the most well-known of such studies of fluctuations in equilibrium thermodynamics is Einstein's seminal treatment of Brownian motion [11–18]. He was able to demonstrate the relationship between the mobility of a fluid system and the temperature through what would later be known as Einstein's relations. These results are important in answering the question of how a physical system that is not initially in equilibrium approaches a state of equilibrium, and led naturally to the later work of Onsager [5,6] and Kubo [7].

The limitation of linear response theory is that it is only valid for small deviations from equilibrium. Nevertheless it served as a historical spring-board for more sophisticated analytical approaches to nonequilibrium kinetics, two of which are the subject of Chapter 2 of this thesis. For instance, soon after the work on Brownian motion by Einstein [11–18] and others [19,20], Fokker [21] and Planck [22] derived a partial differential equation for the probability distribution $f(x,t)$ of a particle in the Brownian ensemble. The Fokker–Planck equation is a specific instance of the more general Master Equation, an integral-differential equation which takes the form

$$\frac{\partial f(x,t)}{\partial t} = \int_{-\infty}^{\infty} \left[-f(x,t)\, W(x,x') + f(x,t)\, W(x',x) \right] \, dx', \tag{1.1}$$

where $W(x,x')\,dx'\,\delta t$ is the probability of a transition from the position x to a position in the interval $(x', x'+dx')$ in time δt, and $W(x',x)dx'\delta t$ is the probability of a transition from the interval $(x', x'+dx')$ to the position x in time δt [23]. It should be clear from its form that the Master Equation describes a process that is inherently Markovian—the probability transition function $W(x,x')$, which mediates the transition, depends on the position x of the particle at time t but not on the previous history of the particle. The particular choice of $W(x,x')$ to be used is model-dependent and determined by the problem under consideration. This accounts for the versatility and richness of the Master Equation method.

In the first half of Chapter 2 of this thesis, we will adopt and adapt the Master Equation to our own purpose, *viz.*, the study of the kinetics of disorder→order transformations in binary alloys.

The path probability method of Kikuchi [24–27] may also be considered as a special instance of the Master Equation Method. Historically, however, the path probability method was developed as a time-dependent elaboration of the the cluster variation method [28–35]. Just as the cluster variation method works by minimizing a free energy expression in terms of cluster probabilities, the path probability method seeks the path linking states that is most probable. In essence, the method replaces the myriad of possible path contributions spanning a time interval $(t, t + \delta t)$ with a single path. This concept of the most probable path is akin to Feynman's path integral formulation of quantum mechanics [36–39] and Fermat's principle of least action. In the second half of Chapter 2, we will apply the path probability method in the pair approximation to the study of disorder→order kinetics in binary alloys.

The original Metropolis [40] implementation of the Monte Carlo method studied the equilibrium configurations in the canonical ensemble of an Ising spin system with Hamiltonian

$$\mathcal{H} = -J \sum_{\langle i,j \rangle} S_i \, S_j - H \sum_i S_i, \tag{1.2}$$

where $\mathcal{H}$ is the Hamiltonian, J is the nearest-neighbor pair interaction, H is the external magnetic field, $S_i \in \{-1, +1\}$ is the spin at site i, and the first summation is over all nearest neighbor pairs $\langle i, j \rangle$. Later, Fosdick *et al.* [41–43] and Guttman [44] adapted the method to the study of binary alloys using a spin-flip mechanism. Although the initial implementations of the Monte Carlo method were concerned with equilibrium systems, it was soon realized that the method could be used to simulate kinetic processes as well [45–48]. With its use in the study of kinetic processes, it was apparent that the choice of mechanism used in the Monte Carlo simulation could have a significant effect on the kinetic evolution and resulting microstructure of the system being studied [45–48]. For instance, in Monte Carlo simulations of ordering, the pair exchange mechanism and vacancy exchange mechanism give strikingly different results [41–48]. In contrast, many equilibrium quantities such as the critical temperature are quite insensitive to the mechanism of order evolution. In Chapter 3, we will use the vacancy mechanism in Monte Carlo simulations of disorder→order kinetics in binary alloys.

1.2 Spinodal Decomposition

The notion of a spinodal instability (or Gibbs instability) is frequently illustrated by considering the dependence of the Helmholtz free energy F on the composition c for a mixture exhibiting phase separation. Figure 1.1 shows schematically such an F–c dependence at some temperature T. The points labeled B and F in Fig. 1.1 correspond to local minima in the free energy curve ($\frac{\partial F}{\partial c} = 0, \frac{\partial^2 F}{\partial c^2} > 0$), whereas the point D corresponds to a local maximum ($\frac{\partial F}{\partial c} = 0, \frac{\partial^2 F}{\partial c^2} < 0$). A homogeneous thermodynamic system in equilibrium at the composition of B is therefore stable against small local fluctuations in the composition—such fluctuations would result in an overall increase of the free energy of the system and would not be favored. In contrast, a homogeneous system at the composition of D will be unstable against small fluctuations in the composition about D. Such fluctuations along the free energy curve will result in an overall lowering of the free energy and will be favored, resulting in the system undergoing a phase separation. The term *spinodal decomposition* is commonly used for phase separation processes such as this, for which there is no free energy barrier to the phase separation [49–51].

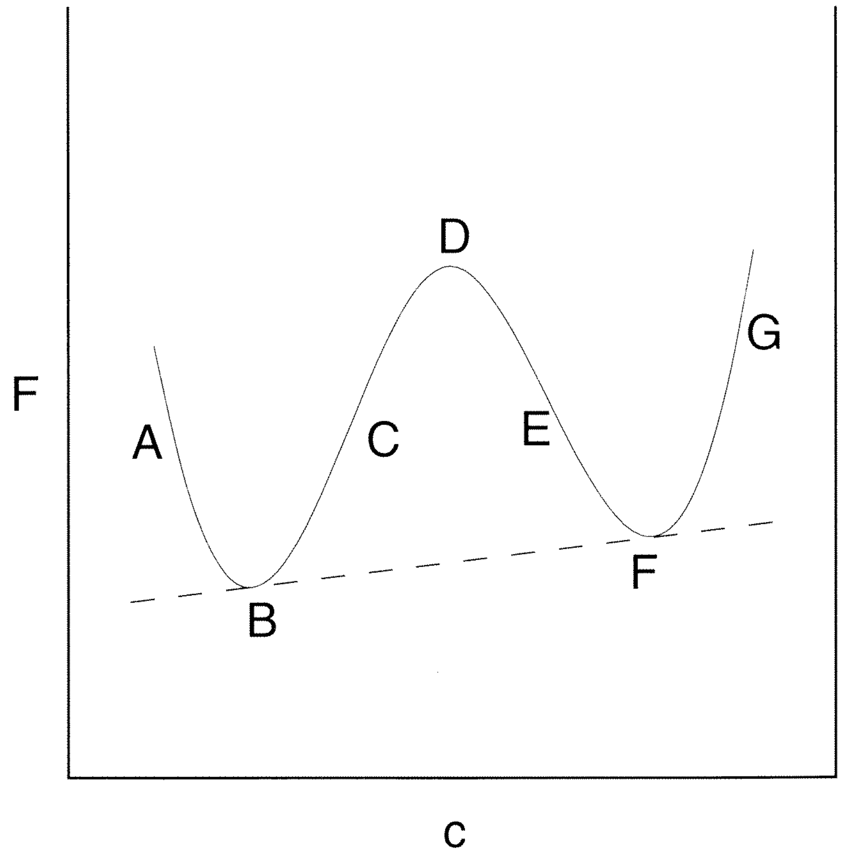

Figure 1.1: Helmholtz free energy F as a function of composition c at some temperature T for a mixture exhibiting phase separation.

The boundaries between the two types of behavior described above occur where $\frac{\partial^2 F}{\partial c^2} = 0$ (at the points labeled C and E) and are referred to as spinodal points. The curvature of the free energy is positive in the regions ABC and EFG and negative in the region CDE. The spinodal decomposition process, if allowed to proceed to completion, eventually results in a two-phase mixture with compositions near B and F in Fig. 1.1. This, in essence, is the reasoning behind the familiar *common-tangent construction.* Note that the two contact points of the common tangent with the free energy curve do not necessarily coincide with the two local minima of the free energy curve (at points labeled B and F in Fig. 1.1).

Recently, Cénédèse and Kikuchi [52] have treated the ferromagnetic Ising model with first-nearest-neighbor interactions on the two-dimensional triangular lattice. Their approach used the cluster variation method of Kikuchi [28–35]. in a series of increasingly accurate approximations, specifically the 1-, 2-, 3-, 4-, and 5-triangle approximations. Earlier work by Kikuchi [53] had shown that this *ladder sequence* of cluster approximations converged to the exact two-dimensional solution. In addition, Cénédèse and Kikuchi [52] also considered the exact solution of the triangular lattice Ising model. The resulting excess free energy *vs.* composition[1] curves obtained using this sequence of approximations for a fixed choice of $\frac{J}{k_B T}$ is shown in Fig. 1.2. The value of $\frac{J}{k_B T}$ was chosen so as to demonstrate strong phase separation. As can be seen from Fig. 1.2, as the size (and hence the accuracy) of the cluster approximation is increased, the excess free energy curves asymptote to the exact solution. This is reassuring. More problematic is the behavior of the excess free energy *vs.* composition for the exact solution, which exhibits an extended region in the middle of the composition range which is horizontal and flat with no trace of the central hump exhibited by the lower

---

[1] The composition ρ is simply the fraction of up (or equivalently down) spins.

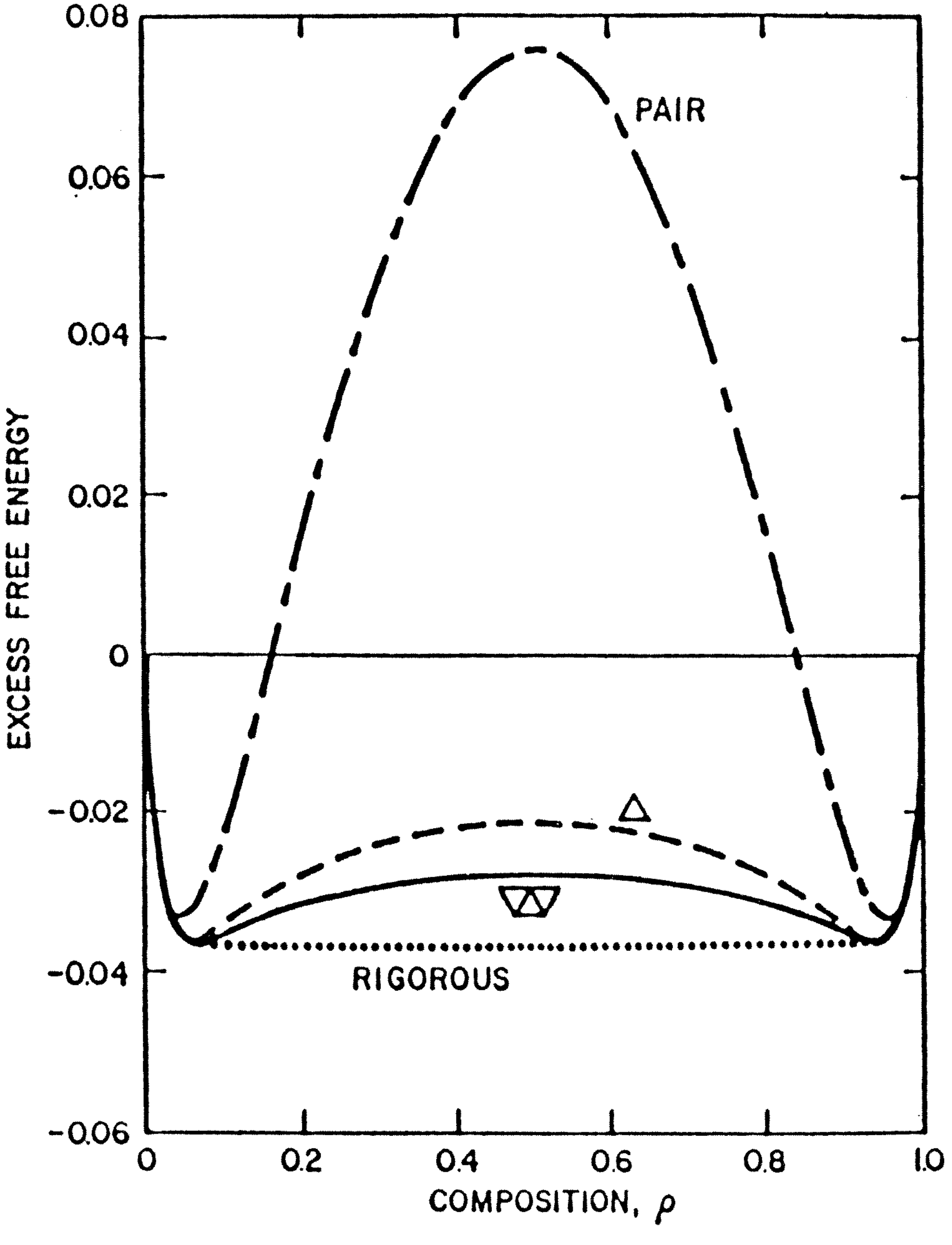

Figure 1.2: Excess Helmholtz free energy F as a function of composition ρ for a fixed value of $\frac{J}{k_BT}$ for the two-dimensional triangular lattice Ising model. The results shown are for the pair, 1-triangle, and 3-triangle approximations as well as the exact solution.

order cluster approximations! Furthermore, the curvature of the excess free energy as a function of composition $\frac{\partial^2 F}{\partial \rho^2}$ for the exact solution in Fig. 1.2 is zero in the flat central region and nonnegative throughout the entire composition range. The spinodal points have vanished! The central hump in the excess free energy *vs.* composition curves exhibited by the lower order cluster approximations—in particular, the regular solution or point approximation—has in the past frequently been interpreted as the driving force for spinodal decomposition, as depicted earlier in Fig. 1.1. However, according to the results of Fig. 1.2, it would seem that this central hump in the free energy is but an artifact of the level of approximation used and is not present in reality!

As mentioned in the previous paragraph, the spinodal points, defined as the points on the free energy *vs.* composition curves where the curvature changes sign, vanish in the exact solution of Fig. 1.2; at no point does the curvature of the free energy become negative. However, since the positions of the spinodal points are well-defined for the finite cluster approximations, it may be possible to define the spinodal points of the exact solution in a limiting sense. Cénédèse and Kikuchi [52] have attempted to do precisely that and the fruits of their labor are shown in Fig. 1.3. Their procedure was as follows. For a given magnetization M and pair interaction J, they found the temperature T_{s} at which M coincided with the position of the spinodal point ($\frac{\partial^2 F}{\partial \rho^2} = 0$). Likewise, they found the temperature T_{pb} at which M coincided with the position of the phase boundary ($\frac{\partial F}{\partial \rho} = 0$). The above procedure was repeated for a series of triangle cluster approximations (1-, 2-, 3-, 4-, and 5-triangle clusters) and two different values of the magnetization ($M = 0.80$ and $M = 0.85$). Figure 1.3 shows $T_{\mathrm{pb}} - T_{\mathrm{s}}$ graphed as a function of $\frac{1}{n+1}$ for $M = 0.80$ and $M = 0.85$, where n is the number of triangles in the cluster approximation. As can be seen an approximately linear relationship between

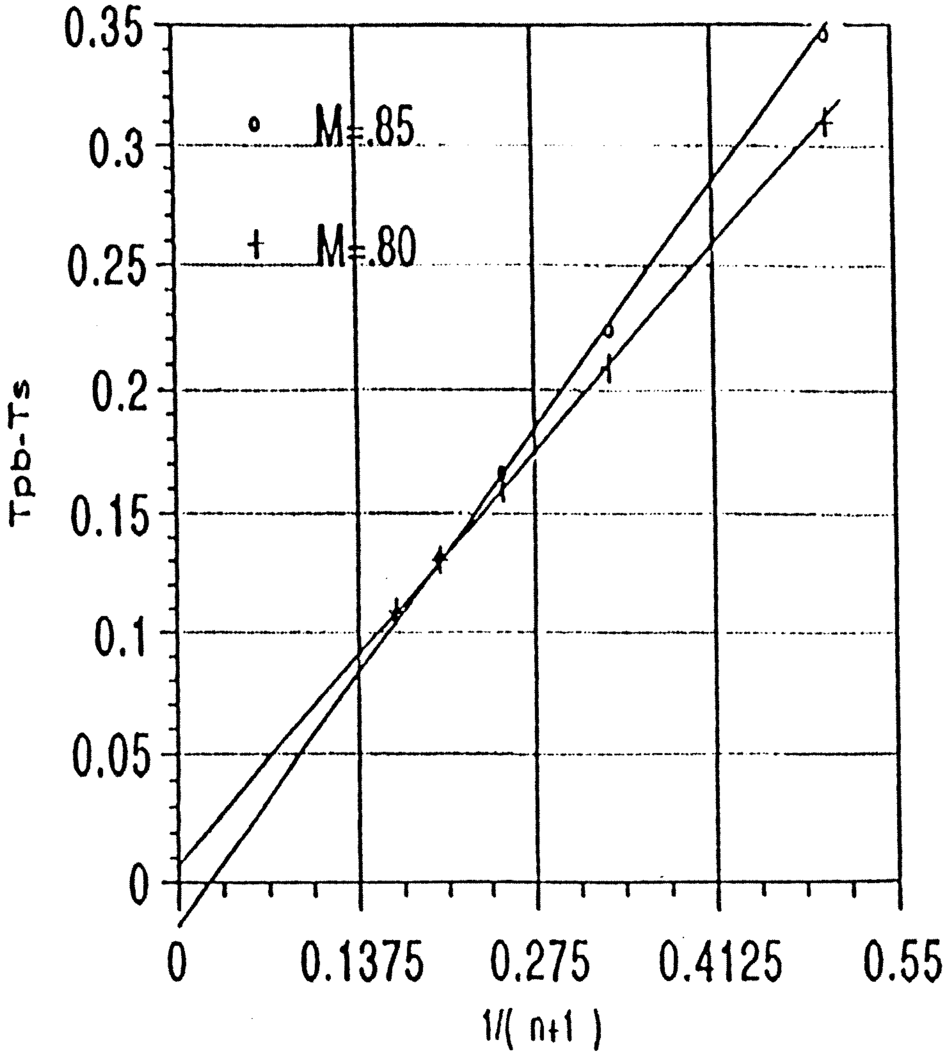

Figure 1.3: $T_{\mathrm{pb}} - T_{\mathrm{s}}$ as a function of $\frac{1}{n+1}$ for $M = 0.80$ and $M = 0.85$, where T_{pb} is the temperature corresponding to the phase boundary, T_{s} is the temperature corresponding to the spinodal point, n is the number of triangles in the cluster approximation, and M is the magnetization.

$T_{\mathrm{pb}} - T_{\mathrm{s}}$ and $\frac{1}{n+1}$ is obtained. Furthermore, the intercepts of the two linear fits to the data are close to zero, suggesting that $\lim_{n\to\infty} T_{\mathrm{pb}} - T_{\mathrm{s}} = 0$. In other words, the spinodal point and the phase boundary coincide in the exact solution!

The results of Figs. 1.2 and 1.3 are susceptible of a ready explanation. As the size of the base cluster (and the accuracy of the corresponding approximation) in the cluster variation method is increased, the base cluster is better able to reproduce the cluster probabilities that would be found in a real crystal lattice *at equilibrium*. For instance, in an alloy undergoing phase separation, the spanning length of the base cluster must be at least as large the wavelength of the spinodal decomposition in order to accurately reproduce the different phases and phase boundaries in the alloy.[2] In the limiting case, the exact solution in Fig. 1.2 is able to reproduce the entire phase separation process. If the exact solution of Fig. 1.2 can be thought of as corresponding to the cluster variation method using a triangle ladder cluster of infinite length as the base cluster, then that cluster would be large enough to reflect the phase separation undergone by the entire (infinite) crystal lattice. Configurations of such a base cluster which reflect this phase segregation would consequently have a high probability relative to those that do not do so. Considered in this light, we see that the excess free energy *vs.* composition curve for the exact solution essentially recovers the common-tangent construction of Fig. 1.1.[3]

Does the above elucidation imply that the phenomenon of spinodal decomposition is a figment of our imagination? Not at all. After all, there is much experimental evidence to support its existence. In addition, Monte Carlo simula-

---

[2] The need for large base clusters is less pressing for the case of alloys undergoing ordering since the base cluster only needs to encompass the period of the ordered structure, and this is usually quite small. However, even here, larger base clusters are needed in order to accurately model larger scale features such as antiphase domains and domain boundaries.

[3] The excess free energy is nonanalytic at the phase boundary.

tions of spinodal decomposition exhibit microstructural and growth features that are strongly reminiscent of the experimental evidence. What it does point out is the need for caution in using equilibrium results to interpret what is really a kinetic phenomenon. In particular, the common interpretation of the miscibility gap in the regular solution or mean-field approximation as the thermodynamic impetus for spinodal decomposition is naïve at best.

Cénédèse and Kikuchi [52] have proposed a way out of this dilemma by considering the excess free energy *vs.* composition curves from a kinetic viewpoint. Their argument is illustrated by Fig. 1.4. The lower set of free energy curves in Fig. 1.4 correspond to an equilibrium temperature T_{h}, which is above the temperature at which phase separation is precipitated in the exact solution.[4] An alloy with composition $\rho = 0.5$ at this temperature T_{h} should be homogeneous and single phase at equilibrium. Consider what would happen if such an equilibrium system were instantaneously quenched from the temperature T_{h} to a much lower temperature T_{l}. Cénédèse and Kikuchi [52] argue that the temperature of the alloy should homogenize quite rapidly to the heat bath temperature T_{l}. However, it takes much longer for the configuration of the alloy to equilibrate to the lower temperature T_{l}. In other words, immediately after the $T_{\mathrm{h}} \to T_{\mathrm{l}}$ quench, the internal energy E and configurational entropy S are essentially identical to the corresponding values before the quench. We can therefore write a *kinetic* free energy expression as follows:

$$F_{\mathrm{l}} = E(T_{\mathrm{h}}) - T_{\mathrm{l}} S(T_{\mathrm{h}}), \tag{1.3}$$

where F_{l} is the *kinetic* free energy immediately after the quench and $E(T_{\mathrm{h}})$ and $S(T_{\mathrm{h}})$ emphasize the fact that the internal energy and configurational entropy

---

[4] The free energy curve for the pair approximation (and, one would expect, that of the point approximation as well) at this temperature exhibits some phase separation but this is merely an artifact of the lack of rigor of the approximation.

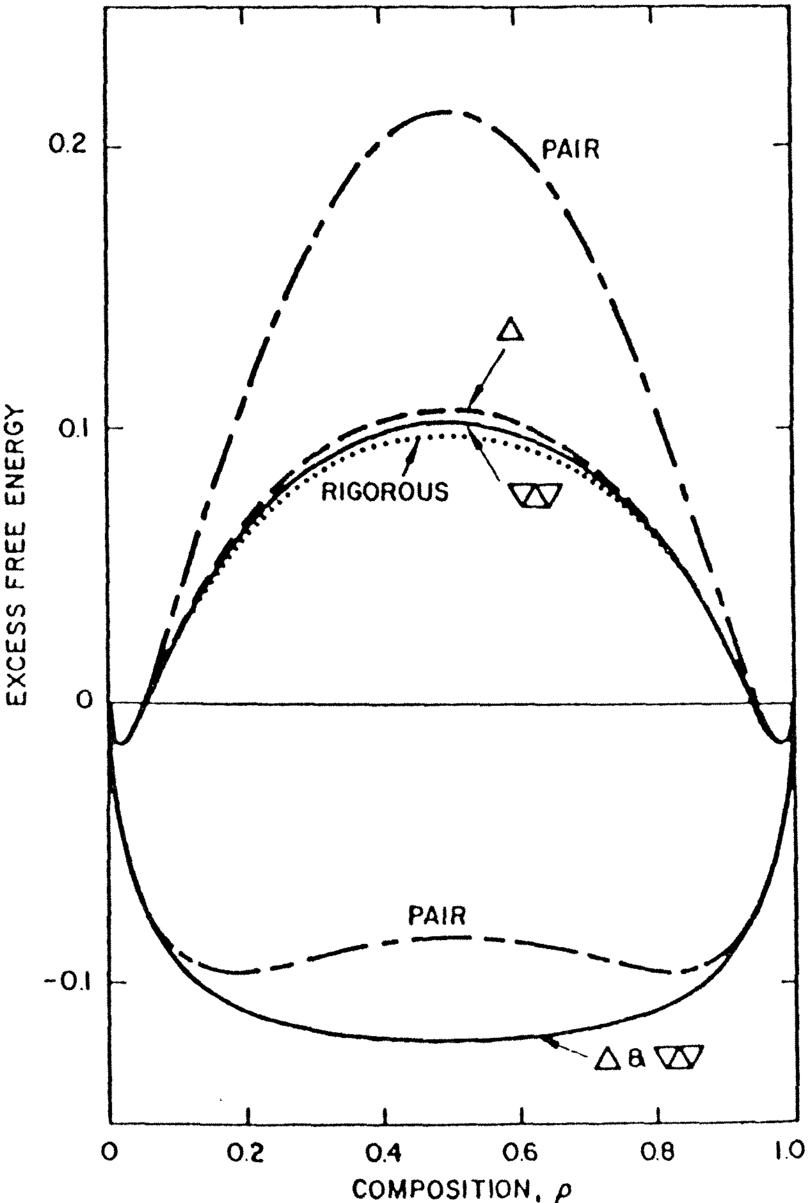

Figure 1.4: Excess Helmholtz free energy F as a function of composition ρ for the two-dimensional triangular lattice Ising model. The results shown are for the pair, 1-triangle, and 3-triangle approximations as well as the exact solution. The lower and upper sets of curves represent the excess free energy before and after a high temperature (T_h) to low temperature (T_l) quench, respectively.

correspond to the temperature before the quench. Such an expression for F_1 was calculated as a function of composition for various levels of approximation and is shown in the upper set of curves of Fig. 1.4. As in the case of Fig. 1.2 and the lower set of curves in Fig. 1.4, these free energy curves converge to the exact solution as the level of approximation is increased. More interestingly, however, the central hump in the free energy persists in the exact solution, as do the spinodal points. Considered in this light, we see that we can salvage the concept of the spinodal if we are willing to admit a kinetic interpretation of the free energy.

1.3 Stability, Metastability, and Instability

> *This downhill path is easy, but there's no turning back.*
>
> *Christina Rossetti*

The concepts of stability and metastability have much currency in materials science today, and may be illustrated using Fig. 1.1. The point B in Fig. 1.1 corresponds to a global minimum of the free energy. A homogeneous system corresponding to this point is in *stable* equilibrium in the sense that any small fluctuation in the composition along the free energy curve results in an increase of the free energy. The point F in Fig. 1.1, though at a minimum locally, is not a global minimum of the free energy. A homogeneous system corresponding to this point is *not* in stable equilibrium. If its composition is allowed to vary, as in a grand canonical ensemble, it will eventually find its way to the point B, which has a lower free energy overall. In order to do so, however, it appears that the system will have to overcome the free energy barrier corresponding to the central hump in Fig. 1.1. Such nonglobal minima in the free energy are commonly referred to as *metastable*. For the sake of completeness, we should also mention that a system at the point D, which is at a local maximum of the free energy, is in unstable equilibrium.

As mentioned in the previous paragraph, for an alloy to go from F to B along the free energy curve, the process would appear to involve a temporary increase in the free energy. This suggests that such a transition would not be favored. This would result in the system at the point F being long-lived, which would help account for the technological importance and usefulness of metastable materials. In reality, the above argument is specious and somewhat misleading. For instance, it implicitly assumes that the system changes its composition uniformly and homogeneously in going from F to B and that it does so along the free energy curve. In actuality, however, the transition would probably occur nonuniformly and heterogeneously via nucleation and growth of the composition corresponding to B. If this were true, then the system would essentially move *along the common tangent* from F to B. In other words, there would be no increase of the free energy in going from F to B, and no free energy barrier to be overcome! This is concordant with the results of Cénédèse and Kikuchi [52] depicted in Fig. 1.2 of the previous section, where the free energy in the exact solution follows the common tangent in the region of phase separation. In a real alloy system, the nucleation and growth of the state corresponding to B would be hindered by the need for long-range diffusion and transport of atoms to form the B phase.

However, the above-mentioned absence of the free energy barrier is only true from a macroscopic viewpoint. At the microscopic or atomic level, there is still an activation barrier to the nucleation of the phase with the lower free energy. This nucleation barrier is similar to the ones commonly described in introductory materials science textbooks [54] and can be illustrated with reference to Fig. 1.5. Consider the formation of an incipient spherical nucleus of the phase with lower

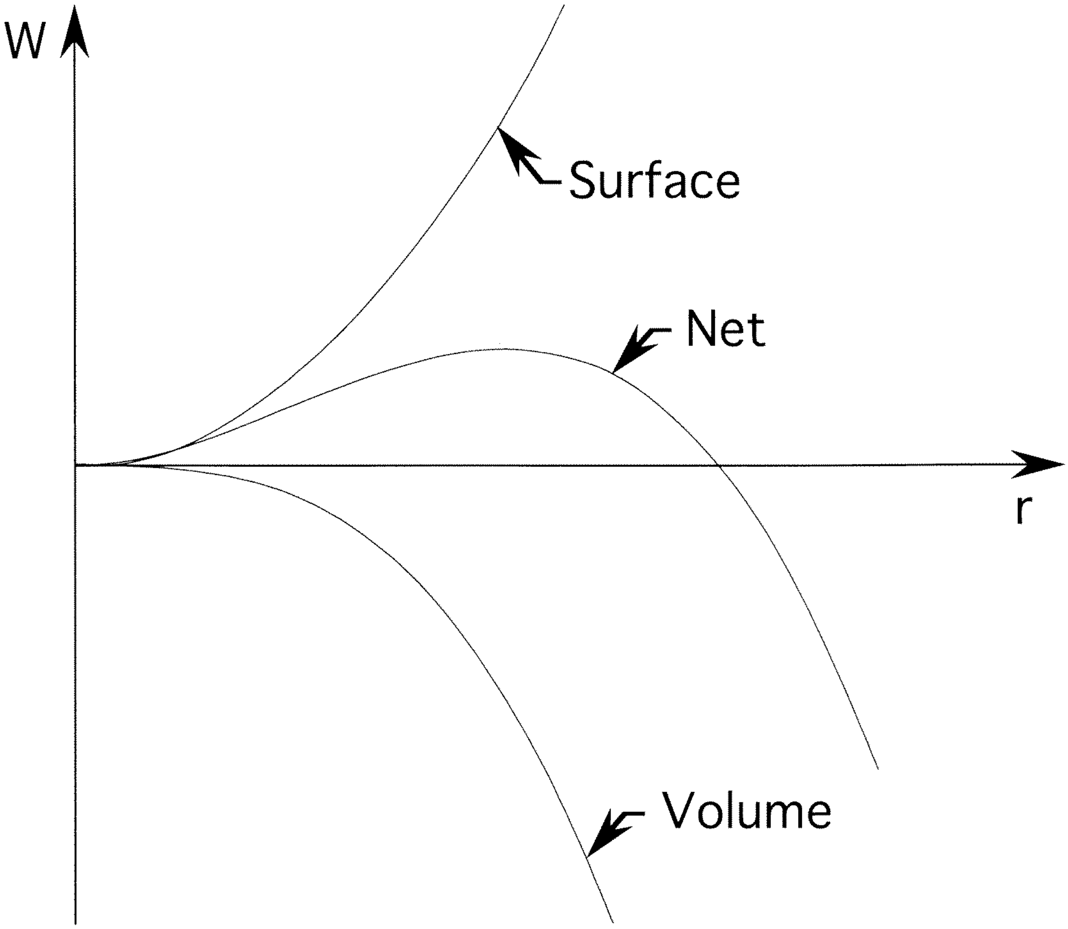

Figure 1.5: The work W required for the formation of a spherical nucleus of radius r.

volume free energy (corresponding to B in Fig. 1.1) in the primary homogeneous phase (corresponding to F in Fig. 1.1). The work required W for the formation of such a nucleus having radius r can be written as

$$W(r) = 4\pi r^2\gamma - \frac{4}{3}\pi r^3 G, \tag{1.4}$$

where γ is the surface energy of the interface between the two phases and G is the magnitude of the difference in volume free energies of the two phases. Straightforward differentiation of Eq. 1.4 with respect to r gives the critical radius r_{crit} of the nucleation process as

$$r_{\text{crit}} = \frac{2\gamma}{G}. \tag{1.5}$$

Nuclei with radii less than the critical radius will tend to decrease in size whereas nuclei with $r > r_{\text{crit}}$ will tend to snowball and precipitate the second phase. The work required for the formation of this critical radius is

$$W(r_{\text{crit}}) = \frac{16}{3}\pi\frac{\gamma^3}{G^2}. \tag{1.6}$$

This energy barrier for the formation of the nucleus must be overcome for the nucleus to increase in size.

One major difference between the energy barrier to nucleation in the microscopic scenario and the ostensible free energy barrier in the macroscopic picture lies in the magnitudes of the energies involved. In the former case, the critical radius is typically on the order of a few atom diameters and the energy barrier to the formation of a nascent nucleus is small enough to be provided by local thermal fluctuations. In contrast, the system at F in Fig. 1.1 is to be considered as being in the thermodynamic (large N) limit, and any free energy barrier would be quite large and not easily surmountable. In light of this, it is clear why the system at F in Fig. 1.1 will tend to transform to the point B by heterogeneous nucleation and growth of the second phase rather than an homogeneous transformation along the equilibrium free energy curve.

1.4 Pseudostability

Things are in the saddle ...

Ralph Waldo Emerson

Local minima and maxima are not the only types of stationary points which may occur in the free energy curve. For instance, in one dimension, there may exist stationary points of inflection, such as the hypothetical one depicted in Fig. 1.6. At the point A in Fig. 1.6, the first and second derivatives of the free energy with respect to composition are zero ($\frac{\partial F}{\partial c} = 0, \frac{\partial^2 F}{\partial c^2} = 0$). Immediately to the left of point A, the second derivative of the free energy is positive ($\frac{\partial^2 F}{\partial c^2} > 0$), whereas just to the right, it is negative ($\frac{\partial^2 F}{\partial c^2} < 0$). A system at the point A, if allowed to vary its composition homogeneously along the equilibrium free energy curve, would eventually find its way to point B, which is a global minimum in the free energy.

In two dimensions, such stationary points may take the form of saddle points in the free energy surface. A saddle point in the free energy $F(\{\xi_i\})$, where $\{\xi_i\}$ represents the relevant state variables, is characterized by having

$$\frac{\partial F}{\partial \xi_i} = 0 \qquad \forall\, \xi_i \tag{1.7}$$

with the additional constraint that the eigenvalues of the Hessian M_{ij}, where

$$M_{ij} = \frac{\partial^2 F}{\partial \xi_i \partial \xi_j}, \tag{1.8}$$

have mixed signs [55]. An example of such a saddle point in the free energy surface is shown in Fig. 1.7, which was abstracted from Ref. [55]. The results

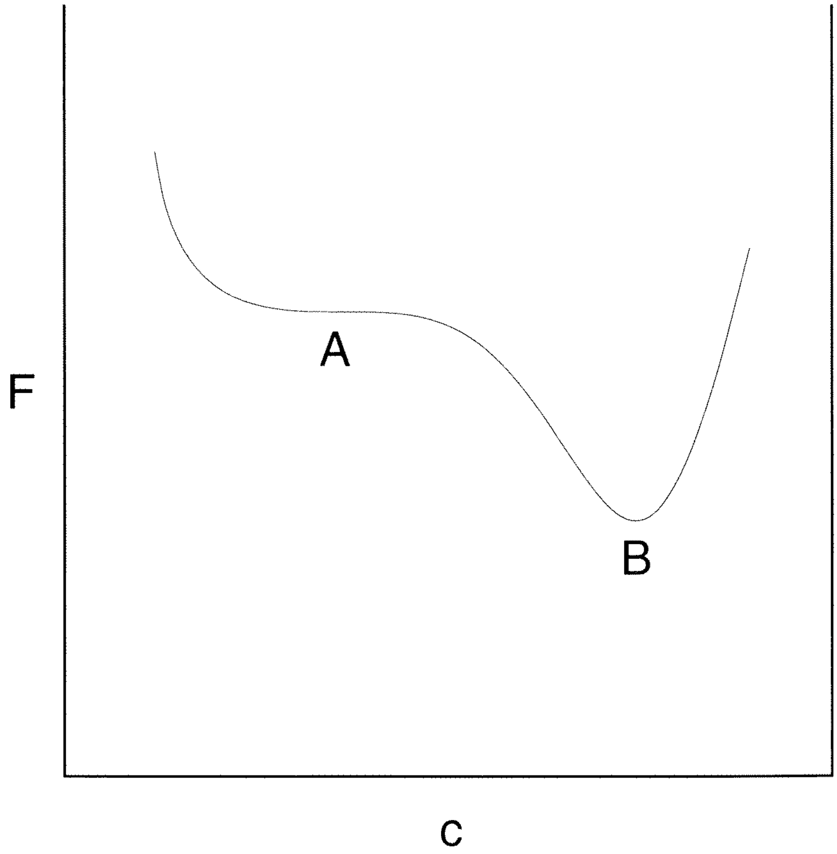

Figure 1.6: Helmholtz free energy F as a function of composition c at some temperature T for a system exhibiting a stationary point of inflection.

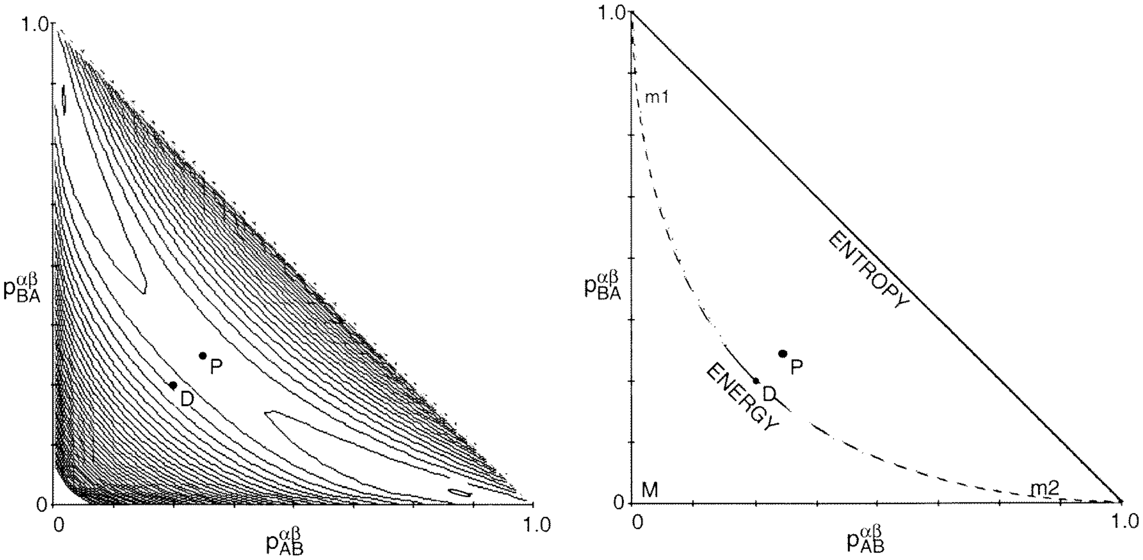

Figure 1.7: Contour plot of the free energy function in the pair approximation for a binary equiatomic bcc alloy exhibiting B2 order (left) with the main features of the the free energy surface indicated (right). The random disordered state is labeled 'D', the absolute (global) minima by 'm1' and 'm2', the absolute maximum by 'M', and the saddle point by 'P'.

shown in Fig. 1.7 were calculated for a binary equiatomic bcc alloy in the pair approximation using the Fowler–Guggenheim entropy correction [56]. The saddle point in Fig. 1.7 is marked P. In the kinetic path that accompanied this figure in Ref. [55], an initially disordered alloy (at the point D) underwent a relatively rapid initial short-range order relaxation to the saddle point P. There was no significant development of long-range order during this initial stage. Once at the saddle point, the alloy remained in this quiescent state for an extended period of time before continuing to develop long-range order as well as additional short-range order. This process took the alloy from P to one of the two global minima (either m1 or m2) in Fig. 1.7. This second leg of the kinetic path followed a more gradual slope with a longer relaxation time than the rapid initial short-range order relaxation. The difference in the gradient of the free energy surface can be discerned from the spacing of the contour lines in Fig. 1.7.

Why should such saddle points in the free energy surface be of importance? The point may be argued as follows [55]. Quite simply, we expect the thermodynamic driving force for the transformation to vanish at such saddle points. In general, we may take the time rate of change of a given state variable ξ_i to depend on the gradient of the free energy in the following manner

$$\frac{d\xi_i}{dt} = \sum_j \gamma_{ij} \frac{\partial F}{\partial \xi_j}, \tag{1.9}$$

where the γ_{ij} are the kinetic coefficients of the system [57]. The above equation may be familiar from Onsager's development [5], where the $\frac{d\xi_i}{dt}$ are our generalized currents and the $\frac{\partial F}{\partial \xi_j}$ our generalized (driving) forces. Substituting Eq. 1.7 into Eq. 1.9, we find that

$$\frac{d\xi_i}{dt} = 0 \qquad \forall\, \xi_i \tag{1.10}$$

at the saddle point. This explains why the saddle point is associated with the long-lived quiescent state in Fig. 1.7 [55]. The term *pseudostable* [55] has been coined to characterize such states which, though neither stable nor metastable, falsely give the appearance of being stable owing to the vanishing or near-vanishing of the thermodynamic driving force for change.

The eigenvalues of the Hessian M_{ij} having mixed signs at the saddle point serves to distinguish it from other stationary points such as local minima and maxima. More than that, however, it provides the alloy a convenient means of reaching the saddle point. In fact, that is precisely what happens in the case illustrated by Fig. 1.7 [55]. The kinetic path of the alloy arrives at the saddle point by coming down a concave 'wing' of the saddle (from D to P in Fig. 1.7) and leaves via a convex 'wing' of the the saddle (from P to either m1 or m2). All the while, the free energy of the alloy is monotonic nonincreasing as a function of time. In contrast, even though the thermodynamic driving force also vanishes at points of local maxima in the free energy surface, it is not at all clear how the alloy will ever arrive at such a point, at least under isothermal conditions, since it faces an uphill struggle against the free energy gradient in order to do so. By this argument, local maxima are generally not expected to play a major role in the generation of long-lived quiescent states during the relaxation of an alloy to equilibrium under isothermal conditions. An exception to the above argument may obtain during nonisothermal processes, when the free energy surface is time-dependent and an alloy may find itself poised precariously at a local maximum as a result of, say, a high- to low-temperature quench.

In using Eq. 1.9, we implicitly assumed a linear response of the system to the free energy gradient. In retrospect, we were justified in making this assumption since the gradient of the free energy surface is near-vanishing in the vicinity of the saddle point. If we make the reasonable assumption that the free energy surface is time-invariant ($\frac{\partial F}{\partial t} = 0$), as it would be for a fixed temperature in the canonical ensemble, we find, using

$$\frac{dF}{dt} = \sum_i \frac{\partial F}{\partial \xi_i} \frac{\partial \xi_i}{\partial t} + \frac{\partial F}{\partial t} \tag{1.11}$$

and Eq. 1.10, that

$$\frac{dF}{dt} = 0 \tag{1.12}$$

at the saddle point. In other words, the free energy is stationary at the saddle point. The fact that the free energy is varying quite slowly as a function of time in the vicinity of the saddle point suggests that it is reasonable to use an equilibrium free energy surface to explain the kinetic behavior of the alloy—the slow evolution of the state of the alloy gives the system ample opportunity to explore most or all of the accessible points in phase space.

Using the fact that Eq. 1.12 holds at saddle points in the free energy surface (although keeping in mind that the converse is not necessarily true), we should be heedful of situations where the free energy is stationary in time as reflecting possible pseudostable states or saddle points in the free energy surface. Using this cue, we will propose possible candidates for pseudostability in the following chapters.

References

[1] L. Onsager, *Phys. Rev.* **65**, 117 (1944).

[2] E. Ising, *Z. Physik* **31**, 253 (1925).

[3] K. G. Wilson and J. Kogut, *Phys. Rep.* **12**, 74 (1974).

[4] K. G. Wilson, *Rev. Mod. Phys.* **55**, 583 (1983).

[5] L. Onsager, *Phys. Rev.* **37**, 405 (1931).

[6] L. Onsager, *Phys. Rev.* **38**, 2265 (1931).

[7] R. Kubo, *J. Phys. Soc. Japan* **12**, 570 (1957).

[8] R. K. Pathria, *Statistical Mechanics*, (Pergamon, Oxford, 1972), Chapter 13.

[9] L. D. Landau and E. M. Lifshitz, *Statistical Physics*, Third Edition Part 1 (Pergamon, Oxford, 1980), Chapter 12.

[10] M. Plischke and B. Bergersen, *Equilibrium Statistical Physics*, (Prentice Hall, Englewood Cliffs, New Jersey, 1989), Chapter 8.

[11] A. Einstein, *Ann. Phys.* **17**, 132 (1905).

[12] A. Einstein, *Ann. Phys.* **17**, 549 (1905).

[13] A. Einstein, *Ann. Phys.* **17**, 891 (1905).

[14] A. Einstein, *Ann. Phys.* **18**, 639 (1905).

[15] A. Einstein, *Ann. Phys.* **19**, 289 (1906).

[16] A. Einstein, *Ann. Phys.* **19**, 371 (1906).

[17] A. Einstein, *Ann. Phys.* **20**, 199 (1906).

[18] A. Einstein, *Ann. Phys.* **20**, 627 (1906).

[19] M. v. Smoluchowski, *Ann. Phys.* **21**, 756 (1906).

[20] M. v. Smoluchowski, *Ann. Phys.* **25**, 205 (1908).

[21] A. D. Fokker, *Ann. Phys.* **43**, 812 (1914).

[22] M. Planck, *Ann. Phys.* **26**, 1 (1908).

[23] R. K. Pathria, *Statistical Mechanics*, (Pergamon, Oxford, 1972), Section 13.5.

[24] R. Kikuchi, *Ann. Phys.* **10**, 127 (1960).

[25] R. Kikuchi, *Phys. Rev.* **124**, 1682 (1961).

[26] R. Kikuchi and P. Gottlieb, *Phys. Rev.* **124**, 1691 (1961).

[27] R. Kikuchi, *Prog. Theor. Phys. Suppl.* **35**, 1 (1966).

[28] R. Kikuchi, *Phys. Rev.* **81**, 988 (1951).

[29] M. Kurata, R. Kikuchi, and T. Watari, *J. Chem. Phys.* **21**, 434 (1953).

[30] J. A. Barker, *Proc. Roy. Soc. A* **216**, 45 (1953).

[31] T. Morita, *J. Math. Phys.* **13**, 115 (1972).

[32] J. M. Sanchez and D. de Fontaine, *Phys. Rev. B* **17**, 2926 (1978).

[33] D. Gratias, J. M. Sanchez, and D. de Fontaine, *Physica A* **113**, 315 (1982).

[34] J. M. Sanchez, F. Ducastelle, and D. Gratias, *Physica A* **128**, 334 (1984).

[35] F. Ducastelle, *Order and Phase Stability in Alloys*, (North-Holland, Amsterdam, The Netherlands, 1991), Section 4.3.

[36] R. P. Feynman, *Rev. Mod. Phys.* **20**, 367 (1948).

[37] R. P. Feynman, R. B. Leighton, and M. Sands, *The Feynman Lectures on Physics*, (Addison–Wesley, Reading, Massachusetts, 1965), Volume II, Chapter 19.

[38] R. P. Feynman and A. R. Hibbs, *Quantum Mechanics and Path Integrals*, (McGraw–Hill, New York, 1965).

[39] R. P. Feynman, *QED — The Strange Theory of Light and Matter*, (Prince-

ton, Princeton, New Jersey, 1985).

[40] N. Metropolis, A. W. Rosenbluth, M. N. Rosenbluth, A. H. Teller, and E. Teller, *J. Chem. Phys.* **21**, 1087 (1953).

[41] L. D. Fosdick, *Phys. Rev.* **116**, 656 (1959).

[42] J. R. Ehrman, L. D. Fosdick, and D. C. Handscomb, *J. Math. Phys.* **1**, 547 (1960).

[43] L. D. Fosdick, *Methods Comp. Phys.* **1**, 245 (1963).

[44] L. Guttman, *J. Chem. Phys.* **34**, 1024 (1961).

[45] P. A. Flinn and G. M. McManus, *Phys. Rev.* **124**, 54 (1961).

[46] J. R. Beeler, Jr. and J. A. Delaney, *Phys. Rev.* **130**, 962 (1963).

[47] J. R. Beeler, Jr., *Phys. Rev.* **134**, A 1396 (1964).

[48] J. R. Beeler, Jr., *Phys. Rev.* **138**, A 1259 (1965).

[49] J. W. Cahn and J. E. Hilliard, *J. Chem. Phys.* **28**, 258 (1958).

[50] M. Hillert, *Acta. Metall.* **9**, 525 (1961).

[51] H. E. Cook, D. de Fontaine, and J. E. Hilliard, *Acta Metall.* **17**, 765 (1969).

[52] P. Cénédèse and R. Kikuchi, unpublished results.

[53] R. Kikuchi, *J. Chem. Phys.* **47**, 1664 (1967).

[54] M. F. Ashby and D. R. H. Jones, *Engineering Materials 2*, (Pergamon, Oxford, 1986).

[55] B. Fultz, *Philos. Mag. B* **67**, 253 (1993).

[56] R. H. Fowler and E. A. Guggenheim, *Proc. Roy. Soc. A* **174**, 189 (1940).

[57] R. K. Pathria, *Statistical Mechanics*, (Pergamon, Oxford, 1972), Section 13.8.

Chapter 2

Analytical Theories of Disorder→Order Transformations

In this chapter I present two distinct but related analytical approaches to the study of disorder→order transformations in binary bcc alloys. Section 2.1 employs a master equation method that is formulated in the Bragg-Williams or point approximation. The method considers the bcc crystal lattice as comprising four fcc sublattices with twice the lattice constant of the parent bcc lattice. Both first- and second-nearest neighbor pair interactions are used in order to allow for the formation of B2, $D0_3$, and B32 order. Section 2.2 makes use of the path probability method in the Bethe or pair approximation. As in the previous instance, a four-sublattice model is used together with first- and second-nearest neighbor pair interactions.

2.1 The Master Equation Method in the Point Approximation

It is shown that a binary alloy with an AB_3 stoichiometry on a bcc lattice may develop various combinations of B2 and $D0_3$ order along its kinetic path towards equilibrium. The temporal evolution of these two order parameters is analyzed with an activated-state rate theory. Individual vacancy jumps are treated in a Master Equation formalism that involves first-nearest-neighbor (1nn) and second-nearest-neighbor (2nn) interactions. In our formulation, a set of coupled differential equations is obtained describing the time-dependence of six order parameters. These equations were integrated numerically for a variety of interatomic interactions and initial conditions. It was found that the *relative* rates of B2 and $D0_3$ ordering, and hence the path of the alloy through the space spanned by the B2 and $D0_3$ order parameters, depend on the relative strengths of the interatomic interaction potentials and on the temperature. For very strong 2nn interactions, a transient B32 structure was observed to develop at early times, although this phase disappeared as equilibrium was approached.

2.1.1 Introduction

Much interest has centered lately on the kinetics of order-disorder transformations in crystalline alloys. In moving away from the traditional studies of equilibrium states to investigations of kinetic phenomena, the first problems to be considered were temporal dependences of a single observable parameter characterizing the state of order of the alloy [1–4]. In two of these theories [1–3] (as well as in studies of diffusion in ternary alloys [5,6]), a variety of independent relaxation processes were observed, such as relaxations of parameters describing long-range order (LRO), short-range order (SRO), and ordering of vacancies. Such observations suggest that it may be possible to observe independent relaxations of two LRO parameters that could be measured by diffraction experiments.

A crystalline alloy characterized by a single observable order parameter will necessarily move through the same nonequilibrium states of order for all possible temperatures and initial conditions. The only anomalies that one might observe are reversals and/or overshoots of the trajectory past the equilibrium end state [1]. With the introduction of additional observable order parameters, however, a rich variety of "kinetic paths" [7] through the state space spanned by the order parameters is possible. In a recent paper that treated the case of B2 ordering in ternary alloys [7], kinetic paths in two order parameters were found to be temperature dependent when the three atomic species differed either in their interatomic interaction potentials or in their saddle-point energies for diffusive jumps. An experimental study [8] of B2 ordering in Fe–Co–Mo ternary alloys attributed an observed temperature dependence of kinetic paths to a high saddle-point energy for Mo diffusion.

In this paper, we extend the master equation approach used previously [7] to treat the case of order-disorder processes in alloys exhibiting simultaneous B2 and $D0_3$ order. We follow the relative rates at which B2 and $D0_3$ order evolve, and we investigate how temperature can be used to control the kinetic path through the two-dimensional parameter space spanned by the LRO parameters (S_{D0_3} and S_{B2}). These efforts were at least partly motivated by our companion experimental study of B2 and $D0_3$ ordering in Fe_3Al [9].

2.1.2 Theory

A body-centered cubic (bcc) alloy of composition AB_3 exhibiting B2 and $D0_3$ order can be described as comprising four interpenetrating face-centered cubic (fcc) sublattices, here denoted α, β, γ, and δ. Two of these fcc sublattices, α and β, together constitute a simple cubic (sc) sublattice (denoted $\alpha \cup \beta$), and the other two sublattices, γ and δ, form a second sc sublattice (denoted $\gamma \cup \delta$). (These two sc sublattices correspond to the "corner sites" and "center sites" of the parent bcc structure.) These two sc sublattices are the sublattices of B2 order. (Table 2.1

summarizes these and other definitions.) Figure 2.1 depicts the four fcc sublattices of the bcc lattice structure and the interconnections between them. It is clear that for a vacancy model of diffusion in which only first-nearest-neighbor (1nn) jumps are allowed, not all sublattices are equally accessible to the moving atom. The arrows in Fig. 2.1 indicate the possible interchanges of an atom and vacancy among these sublattices. For an atom or vacancy on a particular sublattice, only two of the three remaining sublattices are directly accessible to it; diagonal steps are forbidden in Fig. 2.1. In order for an atom or vacancy to move from a particular sublattice to the one diagonally across from it, it must first move onto one of the two adjacent sublattices.

Figure 2.2 shows the B2, $D0_3$, and B32 structures for a binary bcc alloy of composition AB_3. If the composition of the alloy is changed to AB, the $D0_3$ structure is not favored by the stoichiometry, and the sublattices in the B2 and B32 structures which were previously occupied with equal probability by A and B atoms are now populated wholly by A atoms. Figure 2.3 shows the corresponding ground state structures as a function of 1nn and 2nn interaction potentials.

For a bcc lattice having N sites of which $c_{\mathrm{A}}N$ are occupied by A atoms and $c_{\mathrm{B}}N$ are occupied by B atoms, let i, j, k, and l denote the number of A atoms on the α, β, γ, and δ sublattices, respectively. We concern ourselves with stoichiometric AB_3, where $c_{\mathrm{A}} = \frac{1}{4}$, $c_{\mathrm{B}} = \frac{3}{4}$, and $0 \leq i, j, k, l \leq \frac{N}{4}$. We also let p, q, r, and s represent the number of vacancies on the α, β, γ, and δ sublattices ($0 \leq p, q, r, s \leq c_V N$). These eight variables, i, j, k, l, p, q, r, and s, serve as our eight order parameters. Note, however, that only six of these eight order parameters are independent because of the two constraints:

$$i + j + k + l = c_{\mathrm{A}}N, \tag{2.1}$$

Parameter	Definition
N	The number of crystal lattice sites.
A, B	The two species of atoms.
c_{A}, c_{B}	The concentrations of A and B atoms. (Here, as for stoichiometric AB_3, $c_{\mathrm{A}} = \frac{1}{4}$ and $c_{\mathrm{B}} = \frac{3}{4}$.)
c_V	The concentration of vacancies.
α, β, γ, δ	The four interpenetrating fcc sublattices of $\mathrm{D0}_3$ order.
$\alpha \cup \beta$, $\gamma \cup \delta$	The two interpenetrating sc sublattices of B2 order.
i, j, k, l	The numbers of A atoms on the α, β, γ, δ sublattices.
p, q, r, s	The numbers of vacancies on the α, β, γ, δ sublattices.
z	The first-nearest-neighbor (1nn) co-ordination number. ($z = 8$ for a bcc lattice.)
z'	The second-nearest-neighbor (2nn) co-ordination number. ($z' = 6$ for a bcc lattice.)
N^1_{AA}, N^1_{BB}, N^1_{AB}	The numbers of 1nn A–A, B–B, A–B pairs.
N^2_{AA}, N^2_{BB}, N^2_{AB}	The numbers of 2nn A–A, B–B, A–B pairs.
$\{N\}$	$\{N^1_{\mathrm{AA}}, N^1_{\mathrm{BB}}, N^1_{\mathrm{AB}}, N^2_{\mathrm{AA}}, N^2_{\mathrm{BB}}, N^2_{\mathrm{AB}}\}$
V^1_{AA}, V^1_{BB}, V^1_{AB}	The interaction potentials of 1nn A–A, B–B, A–B pairs (in units of k_BT).
V^2_{AA}, V^2_{BB}, V^2_{AB}	The interaction potentials of 2nn A–A, B–B, A–B pairs (in units of k_BT).
$\{V\}$	$\{V^1_{\mathrm{AA}}, V^1_{\mathrm{BB}}, V^1_{\mathrm{AB}}, V^2_{\mathrm{AA}}, V^2_{\mathrm{BB}}, V^2_{\mathrm{AB}}\}$
E_{A}, E_{B}	The activation barrier heights of A and B atoms in the absence of chemical interactions (in units of k_BT).
$\{E\}$	$\{E_{\mathrm{A}}, E_{\mathrm{B}}\}$
$Q^{\mathrm{A}}_{\alpha\gamma}$, etc.	The activation energies for jumps of A atoms from the γ sublattice to the α sublattice (in units of k_BT), etc.
$\{Q\}$	$\{Q^{\mathrm{A}}_{\alpha\gamma}, \ldots\}$
$W^{\mathrm{A}}_{\alpha\gamma}$, etc.	The rates of movement of A atoms from the γ sublattice to the α sublattice, etc.
$\{W\}$	$\{W^{\mathrm{A}}_{\alpha\gamma}, \ldots\}$

Table 2.1: Glossary of terms.

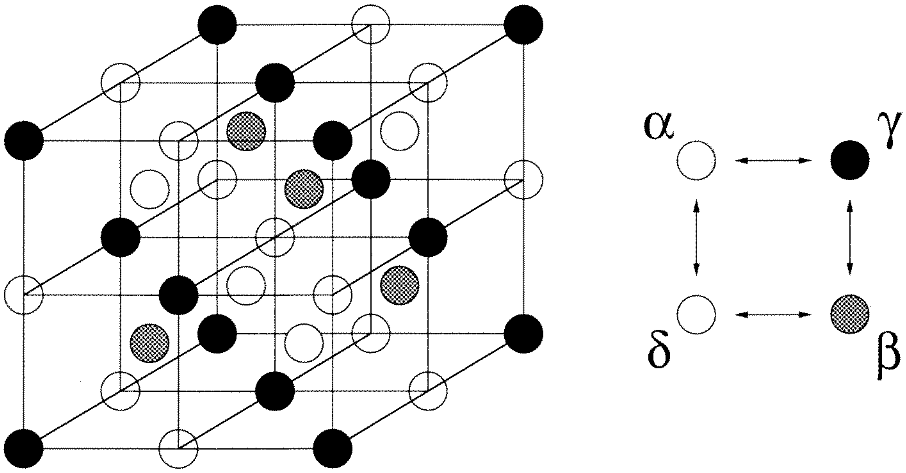

Figure 2.1: The four fcc sublattices of the bcc lattice (left) and the interconnections between them (right). The arrows indicate the possible interchanges of an atom and a vacancy among these sublattices.

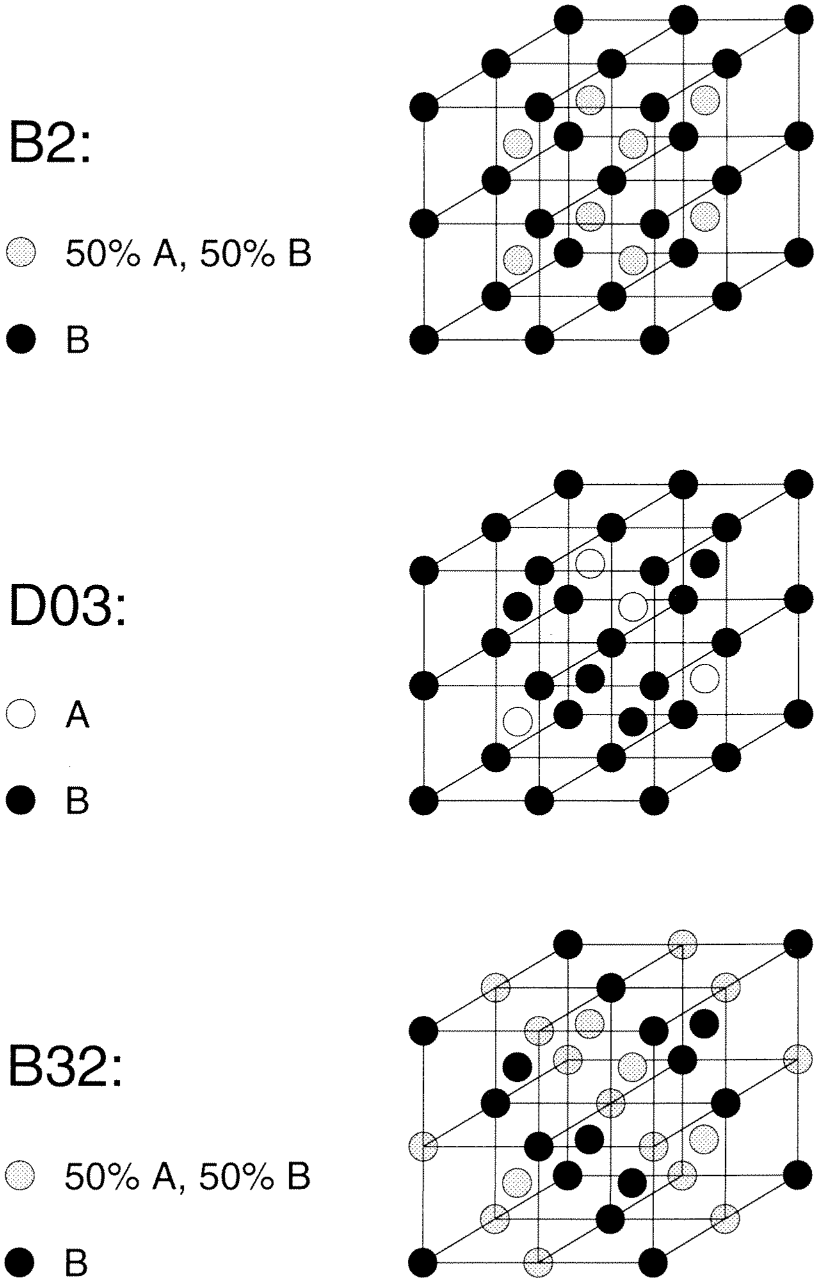

Figure 2.2: The B2 (top), $D0_3$ (middle), and B32 (bottom) structures for a binary bcc alloy of composition AB_3.

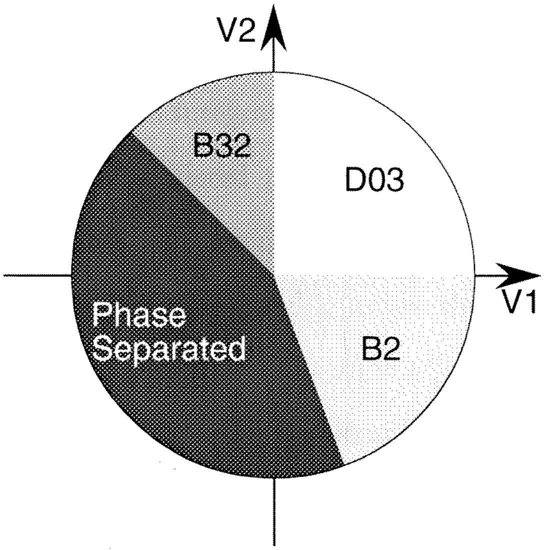

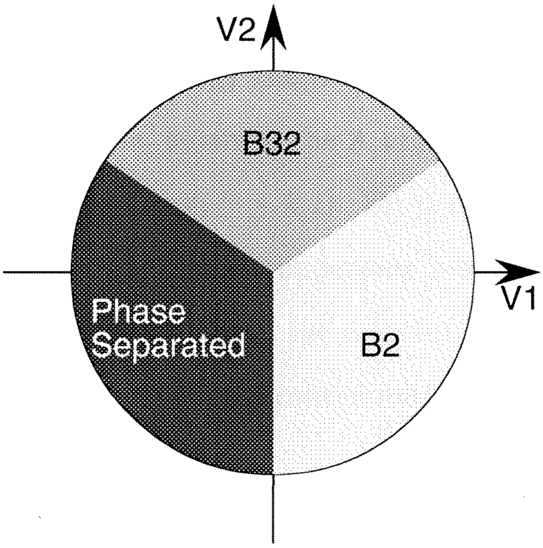

Figure 2.3: The ground state structures for binary bcc alloys of composition AB_3 (top) and AB (bottom).

$$p + q + r + s = c_V N. \tag{2.2}$$

In spite of this redundancy, we chose to work with the eight order parameters as though they were independent, and we used Eqs. 2.1 and 2.2 as consistency checks on the accuracy of our numerical integrations.

In the high-temperature disordered phase, all lattice sites are equally likely to be occupied by an A atom, and the numbers of A atoms on the α, β, γ, and δ sublattices are equal ($i = j = k = l = \frac{N}{16}$), as are the numbers of B atoms on these sublattices $[(\frac{N}{4} - i) = (\frac{N}{4} - j) = (\frac{N}{4} - k) = (\frac{N}{4} - l) = \frac{3N}{16}]$. The two pairs of sublattices, $\alpha \cup \beta$ and $\gamma \cup \delta$, are the two simple cubic (sc) sublattices of the B2 ordered structure, and in the intermediate-temperature B2 phase the A atoms prefer one of the two sc sublattices, say $\alpha \cup \beta$, over the other ($i + j > k + l$). The maximum amount of B2 order in our AB_3 alloy occurs when $i + j = \frac{N}{4}$ and $k + l = 0$. With B2 order in the absence of $D0_3$ order, the A atoms have no preference as to whether they occupy the α sublattice or the β sublattice. In the low-temperature $D0_3$ phase, however, the A atoms prefer one of the four fcc sublattices, say α, over the others ($i > j, k, l$). For perfect $D0_3$ order, $i = \frac{N}{4}$ and $j = k = l = 0$. Now the A atoms have undergone a secondary ordering on the $\alpha \cup \beta$ sublattice, preferentially occupying the α sublattice.

In terms of our order parameters, the conventional parameters for B2 and $D0_3$ order are:

$$S_{\mathrm{B2}} \equiv \frac{(i + j) - (k + l)}{N/2}, \tag{2.3}$$

$$S_{\mathrm{D0_3}}^{\alpha \cup \beta} \equiv \frac{i - j}{N/4}, \tag{2.4}$$

$$S_{\mathrm{D0_3}}^{\gamma \cup \delta} \equiv \frac{k - l}{N/4}, \tag{2.5}$$

where $-1 \leq S_{\mathrm{B2}}, S_{\mathrm{D0_3}}^{\alpha \cup \beta}, S_{\mathrm{D0_3}}^{\gamma \cup \delta} \leq 1$. Note that there are two distinct $D0_3$ order parameters that describe the secondary ordering of the A atoms on each sc sublattice. The existence of three conventional order parameters is consistent with our formalism, where we have three independent order parameters among the i, j, k, and l. The conventional $S_{\mathrm{D0_3}}$ is simply whichever of $S_{\mathrm{D0_3}}^{\alpha\cup\beta}$ and $S_{\mathrm{D0_3}}^{\gamma\cup\delta}$ has the greater magnitude. We also find it convenient to define order parameters for B32 order in terms of those for D0$_3$ order:

$$S_{\mathrm{B32}}^{\alpha\cup\gamma} \equiv S_{\mathrm{D0_3}}^{\alpha\cup\beta} + S_{\mathrm{D0_3}}^{\gamma\cup\delta} - \mathrm{Max}(\mathrm{S}_{\mathrm{D0_3}}^{\alpha\cup\beta}, \mathrm{S}_{\mathrm{D0_3}}^{\gamma\cup\delta}) \equiv -\mathrm{S}_{\mathrm{B32}}^{\beta\cup\delta}, \tag{2.6}$$

$$S_{\mathrm{B32}}^{\alpha\cup\delta} \equiv S_{\mathrm{D0_3}}^{\alpha\cup\beta} - S_{\mathrm{D0_3}}^{\gamma\cup\delta} - \mathrm{Max}(\mathrm{S}_{\mathrm{D0_3}}^{\alpha\cup\beta}, -\mathrm{S}_{\mathrm{D0_3}}^{\gamma\cup\delta}) \equiv -\mathrm{S}_{\mathrm{B32}}^{\beta\cup\gamma}, \tag{2.7}$$

where the third term is subtracted, somewhat artificially, to distinguish B32 order from D0$_3$ order.

Each of the eight 1nn atoms around a vacancy is a candidate for a diffusive jump. In order to move, however, the atom first has to overcome the activation barrier associated with that jump. These activation energies for A and B atoms, Q_{A} and Q_{B}, are (in units of $k_B T$):

$$Q_{\mathrm{A}} = E_{\mathrm{A}} - N_{\mathrm{AA}}^1 V_{\mathrm{AA}}^1 - N_{\mathrm{AB}}^1 V_{\mathrm{AB}}^1 - N_{\mathrm{AA}}^2 V_{\mathrm{AA}}^2 - N_{\mathrm{AB}}^2 V_{\mathrm{AB}}^2, \tag{2.8}$$

$$Q_{\mathrm{B}} = E_{\mathrm{B}} - N_{\mathrm{BB}}^1 V_{\mathrm{BB}}^1 - N_{\mathrm{AB}}^1 V_{\mathrm{AB}}^1 - N_{\mathrm{BB}}^2 V_{\mathrm{BB}}^2 - N_{\mathrm{AB}}^2 V_{\mathrm{AB}}^2. \tag{2.9}$$

In our notation, the V's and N's represent the strengths and numbers of the various interatomic interactions. We consider second-nearest-neighbor (2nn) interactions as well as 1nn interactions since D0$_3$ ordering cannot take place with only 1nn interactions. We have also included a term E_{A} (E_{B}) in the expression above to account for the activation energy for the jump of an A (B) atom in the absence of interatomic interactions. We assume that this "saddle-point" energy depends only on the species of the atom making the jump. Vacancy-atom and vacancy-vacancy interactions are ignored. The average jump rate of an atom into a neighboring vacancy is

$$W = \nu \exp\left(-Q/k_B T\right), \tag{2.10}$$

which is in the usual form of an attempt frequency, ν, times a Boltzmann factor. In what follows, we take ν to be unity without loss of generality.

With a vacancy jump as the elementary kinetic step, we used a Master Equation approach to calculate the evolution of order in the alloy. For a hypothetical alloy whose state of order is specified by only one order parameter, the Master Equation assumes its canonical form

$$\frac{d}{dt}A_i = \sum_{i'} \left\{ W_i^{i'} A_{i'} - W_{i'}^{i} A_i \right\}, \tag{2.11}$$

where the state of order is represented by the vector $\mathbf{A}$, whose components represent the probabilities of the various possible states of order. Since the alloy can be in only one state at a time, $\mathbf{A}$ is of the form

$$\mathbf{A} = \hat{\mathbf{e}}_i, \tag{2.12}$$

where $\hat{\mathbf{e}}_i$ is a basis vector of modulus unity. Transitions between states of order are mediated by the matrix $W_{i'}^{i}$, which takes the alloy from $\hat{\mathbf{e}}_i$ to $\hat{\mathbf{e}}_{i'}$. Except for the states of perfect order, a particular state $\hat{\mathbf{e}}_i$ is many-fold degenerate; a specific state of order may be realized through a variety of atomic arrangements.

In our analysis of B2 and D0$_3$ ordering, the Master Equation takes the form

$$\begin{aligned} \frac{d}{dt}A_{ijklpqrs} = \sum_{i'j'k'l'p'q'r's'} & \left\{ W_{ijklpqrs}^{i'j'k'l'p'q'r's'} A_{i'j'k'l'p'q'r's'} \right. \\ & \left. - W_{i'j'k'l'p'q'r's'}^{ijklpqrs} A_{ijklpqrs} \right\}. \end{aligned} \tag{2.13}$$

The state of order in our alloy is now represented by a matrix of rank eight $A_{ijklpqrs}$, and transitions between these states are mediated by an operator of rank sixteen

$W_{ijklpqrs}^{i'j'k'l'p'q'r's'}$. Conveniently, the vast majority of the elements of the W-operator are zero because the elementary kinetic step is a single jump of a single atom into a vacant neighboring lattice site. Thus, the eight order parameters can change at most by ±1, making the W-operator "tri-diagonal." Its only nonzero elements are of the forms

$$W_{i\pm1,j,k\mp1,l,p\mp1,q,r\pm1,s}^{i,j,k,l,p,q,r,s}, \quad W_{i\pm1,j,k,l\mp1,p\mp1,q,r,s\pm1}^{i,j,k,l,p,q,r,s},$$

$$W_{i,j\pm1,k\mp1,l,p,q\mp1,r\pm1,s}^{i,j,k,l,p,q,r,s}, \quad W_{i,j\pm1,k,l\mp1,p,q\mp1,r,s\pm1}^{i,j,k,l,p,q,r,s},$$

for jumps of A atoms, and

$$W_{i,j,k,l,p\mp1,q,r\pm1,s}^{i,j,k,l,p,q,r,s}, \quad W_{i,j,k,l,p\mp1,q,r,s\pm1}^{i,j,k,l,p,q,r,s},$$

$$W_{i,j,k,l,p,q\mp1,r\pm1,s}^{i,j,k,l,p,q,r,s}, \quad W_{i,j,k,l,p,q\mp1,r,s\pm1}^{i,j,k,l,p,q,r,s},$$

for jumps of B atoms. These correspond to the allowed atom-vacancy interchanges along the double-headed arrows of Fig. 2.1. For instance, in the elementary kinetic step of an A atom jumping from the γ sublattice to the α sublattice, the only changes in the order parameters are $\Delta i = +1$, $\Delta k = -1$, $\Delta p = -1$, and $\Delta r = +1$. The element of the W-operator inducing this transition is $W_{i+1,j,k-1,l,p-1,q,r+1,s}^{i,j,k,l,p,q,r,s}$, which we abbreviate as $W_{\alpha\gamma}^{\mathrm{A}}$. This rate is composed of three factors:

- the probability that an atom on the γ sublattice is an A atom, $(k/\frac{N}{4})$,
- the probability that one of the $\frac{z}{2}$ neighboring sites on the α sublattice is occupied by a vacancy, $(p/\frac{N}{4})\frac{z}{2}$,
- the corresponding Boltzmann factor for the jump, $\exp(-Q_{\alpha\gamma}^{\mathrm{A}})$.

The activation energy for this jump, $Q_{\alpha\gamma}^{\mathrm{A}}$ (in units of k_BT), depends on the identities of the 1nn and 2nn atoms of the jumping atom as given in Eqs. 2.8 and 2.9. Of these neighboring atoms, $\frac{z}{2}-1$ are on the α sublattice,[1] $\frac{z}{2}$ are on the β sublattice, and z' are on the δ sublattice. In summary, we write

$$W^{i,j,k,l,p,q,r,s}_{i+1,j,k-1,l,p-1,q,r+1,s} \equiv W^{\mathrm{A}}_{\alpha\gamma} = \left(k\middle/\tfrac{N}{4}\right)\left(p\middle/\tfrac{N}{4}\right)\tfrac{z}{2}\exp\left(-Q^{\mathrm{A}}_{\alpha\gamma}\right), \tag{2.14}$$

where

$$\begin{aligned} Q^{\mathrm{A}}_{\alpha\gamma} = E_{\mathrm{A}} &- \left[V^{1}_{\mathrm{AA}}i + V^{1}_{\mathrm{AB}}\left(\tfrac{N}{4}-i\right)\right]\left(\tfrac{z}{2}-1\right)\middle/\tfrac{N}{4} \\ &- \left[V^{1}_{\mathrm{AA}}j + V^{1}_{\mathrm{AB}}\left(\tfrac{N}{4}-j\right)\right]\tfrac{z}{2}\middle/\tfrac{N}{4} \\ &- \left[V^{2}_{\mathrm{AA}}l + V^{2}_{\mathrm{AB}}\left(\tfrac{N}{4}-l\right)\right]z'\middle/\tfrac{N}{4}. \end{aligned} \tag{2.15}$$

Similar expressions exist for the other fifteen nonzero elements of the W-operator. In writing Eq. 2.15, we have ignored the distinction between LRO and SRO correlations between atoms and have obtained the local neighborhood of the A atom from the total sublattice occupancies. This is analogous to the mean field approximation of equilibrium thermodynamics.

For a given set of 1nn and 2nn interactions, these expressions for $\{W\}$ depend only on the order parameters $\{i,j,k,l,p,q,r,s\}$. From these $\{W\}$, we obtain expressions for the instantaneous rates of change of the order parameters:

$$J_i \equiv \frac{di}{dt} = W^{\mathrm{A}}_{\alpha\gamma} + W^{\mathrm{A}}_{\alpha\delta} - W^{\mathrm{A}}_{\gamma\alpha} - W^{\mathrm{A}}_{\delta\alpha}, \tag{2.16}$$

$$J_j \equiv \frac{dj}{dt} = W^{\mathrm{A}}_{\beta\gamma} + W^{\mathrm{A}}_{\beta\delta} - W^{\mathrm{A}}_{\gamma\beta} - W^{\mathrm{A}}_{\delta\beta}, \tag{2.17}$$

$$J_k \equiv \frac{dk}{dt} = W^{\mathrm{A}}_{\gamma\alpha} + W^{\mathrm{A}}_{\gamma\beta} - W^{\mathrm{A}}_{\alpha\gamma} - W^{\mathrm{A}}_{\beta\gamma}, \tag{2.18}$$

$$J_l \equiv \frac{dl}{dt} = W^{\mathrm{A}}_{\delta\alpha} + W^{\mathrm{A}}_{\delta\beta} - W^{\mathrm{A}}_{\alpha\delta} - W^{\mathrm{A}}_{\beta\delta}, \tag{2.19}$$

$$\begin{aligned} J_p \equiv \frac{dp}{dt} &= W^{\mathrm{A}}_{\gamma\alpha} + W^{\mathrm{A}}_{\delta\alpha} - W^{\mathrm{A}}_{\alpha\gamma} - W^{\mathrm{A}}_{\alpha\delta} \\ &\quad + W^{\mathrm{B}}_{\gamma\alpha} + W^{\mathrm{B}}_{\delta\alpha} - W^{\mathrm{B}}_{\alpha\gamma} - W^{\mathrm{B}}_{\alpha\delta}, \end{aligned} \tag{2.20}$$

$$J_q \equiv \frac{dq}{dt} = W^{\mathrm{A}}_{\gamma\beta} + W^{\mathrm{A}}_{\delta\beta} - W^{\mathrm{A}}_{\beta\gamma} - W^{\mathrm{A}}_{\beta\delta}$$

---

[1] One of the sites on the α sublattice is the soon-to-be-occupied vacancy.

$$+ W^{\mathrm{B}}_{\gamma\beta} + W^{\mathrm{B}}_{\delta\beta} - W^{\mathrm{B}}_{\beta\gamma} - W^{\mathrm{B}}_{\beta\delta}, \tag{2.21}$$

$$\begin{aligned} J_r \equiv \frac{dr}{dt} &= W^{\mathrm{A}}_{\alpha\gamma} + W^{\mathrm{A}}_{\beta\gamma} - W^{\mathrm{A}}_{\gamma\alpha} - W^{\mathrm{A}}_{\gamma\beta} \\ &+ W^{\mathrm{B}}_{\alpha\gamma} + W^{\mathrm{B}}_{\beta\gamma} - W^{\mathrm{B}}_{\gamma\alpha} - W^{\mathrm{B}}_{\gamma\beta}, \end{aligned} \tag{2.22}$$

$$\begin{aligned} J_s \equiv \frac{ds}{dt} &= W^{\mathrm{A}}_{\alpha\delta} + W^{\mathrm{A}}_{\beta\delta} - W^{\mathrm{A}}_{\delta\alpha} - W^{\mathrm{A}}_{\delta\beta} \\ &+ W^{\mathrm{B}}_{\alpha\delta} + W^{\mathrm{B}}_{\beta\delta} - W^{\mathrm{B}}_{\delta\alpha} - W^{\mathrm{B}}_{\delta\beta}. \end{aligned} \tag{2.23}$$

This set of eight coupled nonlinear first-order differential equations completely determines the trajectory of the alloy through (i, j, k, l, p, q, r, s)-space for a given set of initial conditions $\{i_0, j_0, k_0, l_0, p_0, q_0, r_0, s_0\}$. The velocity of this trajectory at any instant is given by

$$\mathbf{J} = J_i\hat{\mathbf{i}} + J_j\hat{\mathbf{j}} + J_k\hat{\mathbf{k}} + J_l\hat{\mathbf{l}} + J_p\hat{\mathbf{p}} + J_q\hat{\mathbf{q}} + J_r\hat{\mathbf{r}} + J_s\hat{\mathbf{s}}. \tag{2.24}$$

For a given set of initial conditions, we use the expression for $\mathbf{J}$ to obtain the kinetic path through (i, j, k, l, p, q, r, s)-space by numerical integration.

2.1.3 Numerical Computations

Using Eqs. 2.14 and 2.15 and their fifteen analogs, Eqs. 2.16–2.23 were integrated numerically for a variety of initial configurations and interaction energies $\{V\}$ and $\{E\}$. The computer code was written in VAX FORTRAN and executed on a MicroVAX VAXstation II. It proved desirable to use quadruple-precision arithmetic for increased accuracy. Because the vacancy concentration on a particular sublattice is usually very much lower than the concentrations of A or B atoms on that sublattice, the absolute changes in these concentrations in some fixed time interval have a similar disparity in magnitude. This leads to Eqs. 2.16–2.23 being "stiff," and troublesome to integrate. Various methods of integration were tried [10,11], from the forward Euler method to the Bulirsch-Stoer method, but the one that proved most successful was the fourth-order Runge-Kutta method with adaptive step-size control. Nevertheless, all methods gave identical results within the limits of our computational precision when they were stable. Graphs showing the time evolution of the eight order parameters $\{i, j, k, l, p, q, r, s\}$ were generated. Since we are primarily interested in the relative rates of change of the four order parameters $\{i, j, k, l\}$, it proved convenient to plot them against each other, e.g., j *vs.* i. The axes of such graphs as presented here are labeled in terms of N. This emphasizes the fact that the calculated kinetic paths scale with the choice of N. For our purposes, we chose a value of 4×10^6 for N. Using Eqs. 2.3–2.5, graphs of S_{B2} *vs.* $S_{\mathrm{D0_3}}$ were also obtained.

One interesting and useful feature of the kinetic paths obtained is that they are independent of c_V for $c_V \ll c_{\mathrm{A}}, c_{\mathrm{B}}$ [7]. This independence of the kinetic paths on c_V was confirmed empirically by varying c_V while keeping the other input parameters unchanged. This meant that instead of using values of c_V typical of a quenched alloy ($\sim 10^{-5}$) for our numerical integrations, somewhat larger values of c_V (albeit values of $c_V \ll c_{\mathrm{A}}, c_{\mathrm{B}}$) could be used to speed up the computations. For instance, the kinetic paths obtained with $c_V = 10^{-2}$ were virtually identical to those obtained with $c_V = 10^{-3}$ but were noticeably different from those obtained with $c_V = 10^{-1}$. For our purposes, we took $c_V = 10^{-2}$.

2.1.4 Results and Discussion

Figures 2.4 and 2.5 show kinetic paths at two different temperatures for an alloy in which $V^1_{\mathrm{AA}} = V^1_{\mathrm{BB}} = V^2_{\mathrm{AA}} \equiv V$. (Hereafter, all V's and E's will be assumed to be zero unless explicitly stated otherwise. In these and other figures, the temperature is expressed in terms of the critical temperatures for both B2 and D0$_3$ ordering. Since the relative magnitudes of these two critical temperatures depend

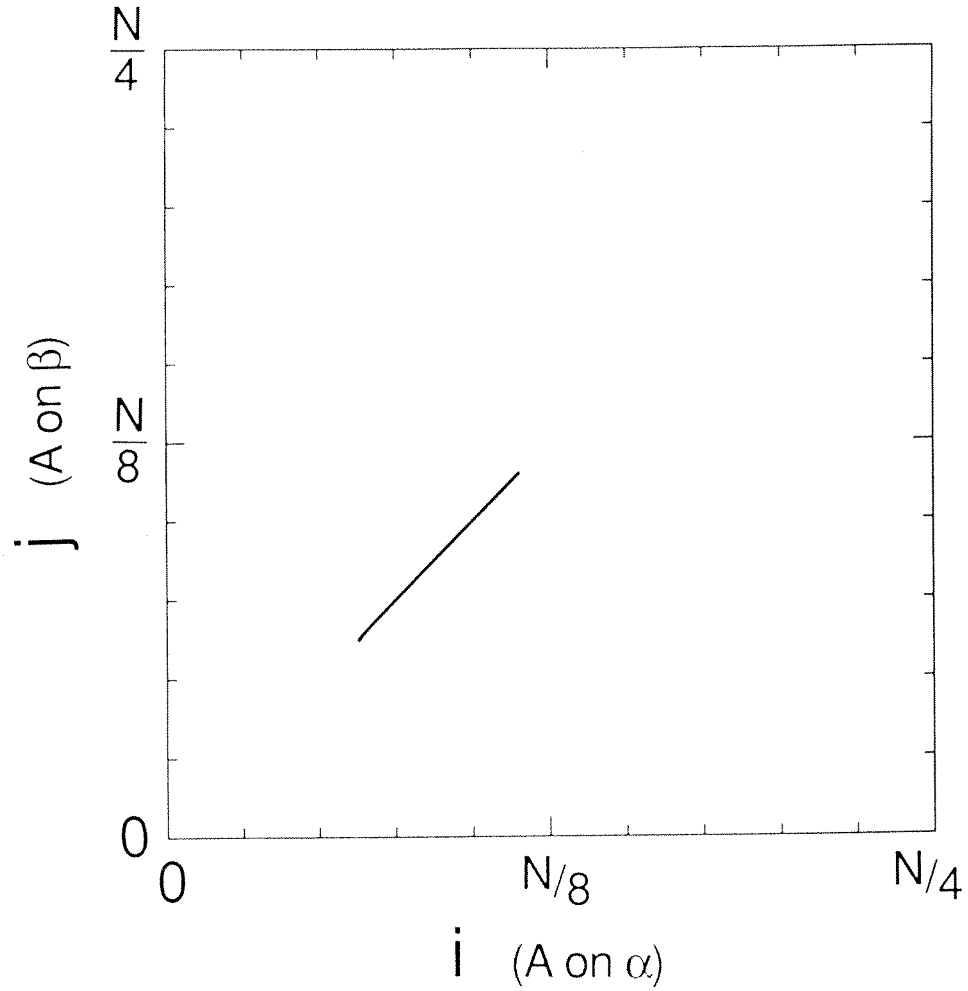

Figure 2.4: Kinetic path of an initially disordered alloy exhibiting B2 ordering ($V^1_{\mathrm{AA}} = V^1_{\mathrm{BB}} = V^2_{\mathrm{AA}} = 0.90$; $T = 0.74T_c^{\mathrm{B2}} = 1.11T_c^{\mathrm{D0_3}}$). The end-points of the i–j curves are our best estimates of the equilibrium end-points. The values of k and l decreased to near zero at equilibrium.

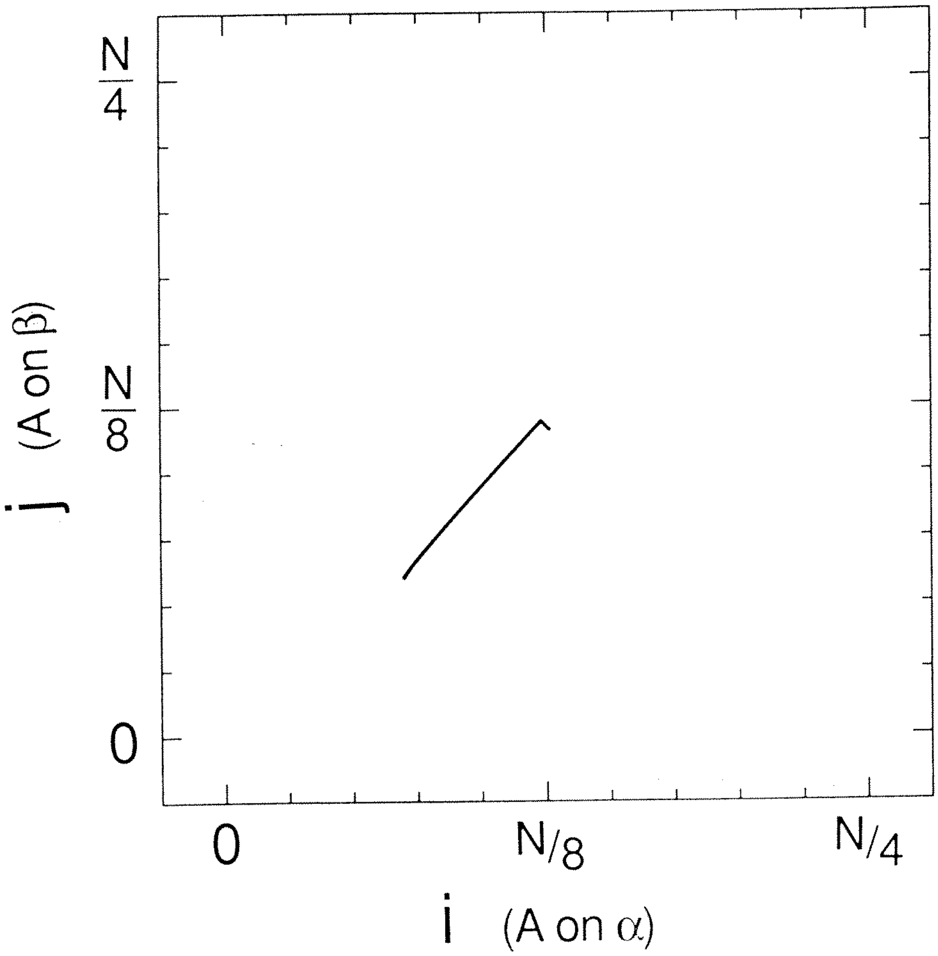

Figure 2.5: Kinetic path of an initially disordered alloy exhibiting B2 and D0$_3$ ordering ($V^1_{\rm AA} = V^1_{\rm BB} = V^2_{\rm AA} = 1.10$; $T = 0.61T_c^{\rm B2} = 0.91T_c^{\rm D0_3}$). The end-points of the i–j curves are our best estimates of the equilibrium end-points. The values of k and l decreased to near zero at equilibrium.

on the relative magnitudes the various 1nn and 2nn interaction strengths, a simple expression for T_c^{B2} and $T_c^{\mathrm{D0_3}}$ in terms of the V's does not exist.) This is one of the simpler combinations of potentials that is able to generate D0_3 order. The alloys were started near complete disorder ($i_0 = \frac{N}{16}+3\epsilon, \quad j_0 = k_0 = l_0 = \frac{N}{16}-\epsilon$, where ϵ is some small positive quantity introduced to force the alloy off the stationary point at zero order; $p_0 = q_0 = r_0 = s_0$) and allowed to relax to equilibrium. The end-points of the i–j curves are our best estimates of the equilibrium end-points unless otherwise noted. The values of k and l decreased to near zero at equilibrium. In Fig. 2.4, i and j increased to equilibrium values slightly less than $\frac{N}{8}$, whereas k and l decreased to equilibrium values close to zero.[2] This equilibrium configuration corresponds to B2 order without any D0_3 order. Figure 2.5 was obtained from an alloy that underwent ordering at a lower temperature. As before, the alloy initially developed B2 order. However, once near-maximal B2 order was obtained, i continued to increase but at the expense of j, which started to decrease. At this point, the A atoms began undergoing a secondary ordering on the $\alpha \cup \beta$ sublattice, segregating preferentially to the α sublattice. (Meanwhile, k and l continued to remain close to zero.) This secondary ordering proceeded until equilibrium D0_3 order was reached. The time scale on which the secondary D0_3 ordering took place was slower than the initial evolution of B2 order by as much as two orders of magnitude. This difference in time scales can be understood as follows. Before an A atom on the β sublattice can move onto the α sublattice, it must first move onto the γ or δ sublattice. This movement is impeded because by the time near-maximal B2 order is achieved and D0_3 ordering begins, the A-atom population on the γ and δ sublattices has diminished to near zero. Since the γ and δ sublattices

---

[2] Since k_0 and l_0 were chosen to be equal to each other, and the γ and δ sublattices are equivalent, k and l should always be equal to each other and, given i and j, can be deduced from Eq. 2.1.

are the immediate source of A atoms moving onto the α sublattice, the migration of A atoms from the β sublattice to the α sublattice is severely bottle-necked.

With other choices of interatomic interaction potentials, the evolution of B2 and $D0_3$ order does not occur in a two-step process in which B2 ordering is essentially complete before $D0_3$ ordering begins. With our choice of initial conditions, the evolution of $D0_3$ order involves the net flow of A atoms from the β sublattice first to the γ or δ sublattice, and then to the α sublattice. The 1nn environments for atoms on the α and β sublattices are identical and consist of atoms on the γ and δ sublattices. Similarly, there is no differentiation between the α and β sublattices in the 1nn environments of atoms on the γ and δ (although there must be a vacant site on the α or β sublattice for the jump onto this sublattice to occur). The α and β sublattices are hence identical with respect to 1nn interactions, and therefore any difference in Boltzmann factors that promotes a net difference in the flows of A atoms onto the α and β sublattices must originate with the 2nn interactions. By increasing V^2_{AA} and V^2_{BB} relative to V^1_{AA} and V^1_{BB}, it should be possible to force strong $D0_3$ ordering initially without having to wait for B2 ordering to go to completion. (We are justified in neglecting the vacancy concentrations in this argument because there is no significant redistribution of the vacancy concentrations among the four sublattices during the early, near-disorder, stages of ordering.)

An example of two different kinetic paths is presented in Fig. 2.6, in which $V^1_{\mathrm{AA}} = V^2_{\mathrm{AA}} = 1.60$ and V^1_{BB} equals 1.20 and 0.40. With the stronger V^1_{BB}, the alloy follows an initial kinetic path that is the growth of essentially pure B2 order. For the weaker V^1_{BB}, and hence a relatively stronger V^2_{AA}, the path falls below this diagonal line of $i = j$, indicating the initial evolution of some $D0_3$ order. (Note, however, that both kinetic paths in Fig. 2.6 terminate near the lower right corner,

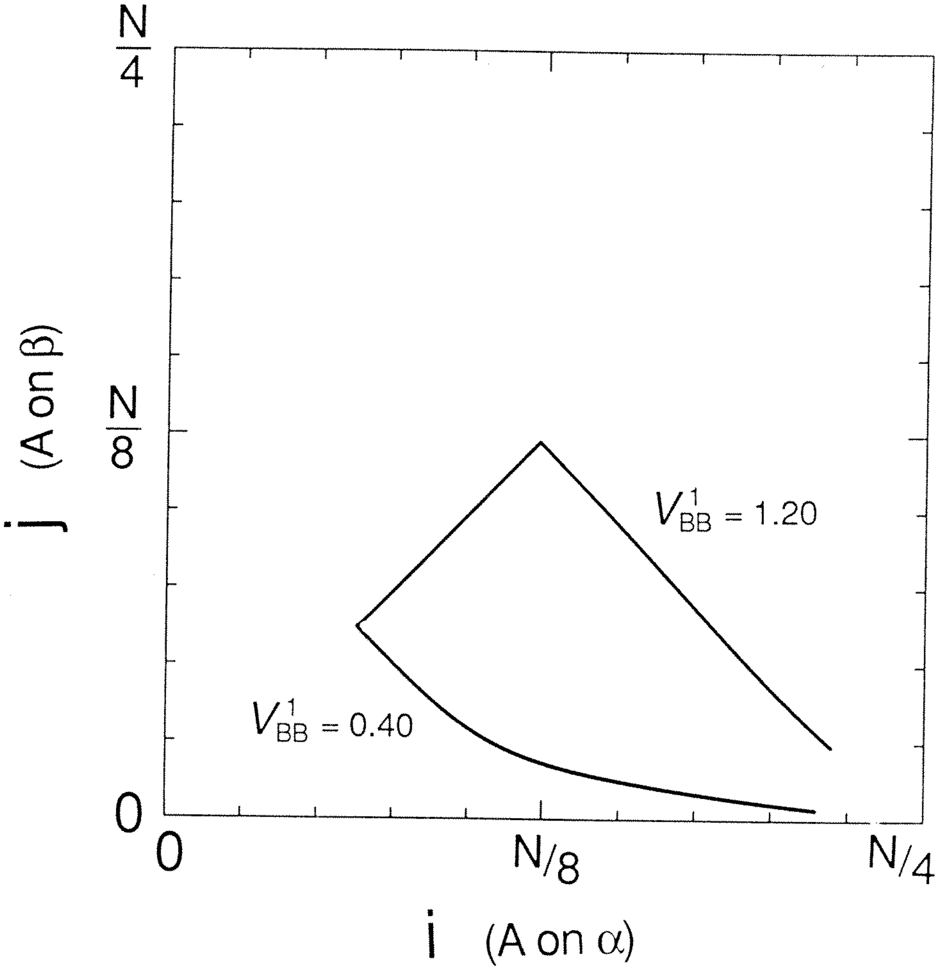

Figure 2.6: Kinetic paths exhibiting the transition from initial B2 ordering to initial D0$_3$ ordering. Labels indicate values of V_{BB}^1 ($V_{\mathrm{AA}}^1 = V_{\mathrm{AA}}^2 = 1.60$; $V_{\mathrm{BB}}^1 = 0.40 \Rightarrow T = 1.21T_c^{\mathrm{B2}} = 0.70T_c^{\mathrm{D0_3}}$; $V_{\mathrm{BB}}^1 = 1.20 \Rightarrow T = 0.53T_c^{\mathrm{B2}} = 0.61T_c^{\mathrm{D0_3}}$). See text for further explanation.

where all the A atoms are situated on the α sublattice. This corner corresponds to $S_{\rm B2} = \frac{1}{2}$ and $S_{\rm D0_3}^{\alpha\cup\beta} = 1$.) As expected, we found that the sharpness of this transition became more marked at lower temperatures due to the $\frac{1}{T}$ dependence of the terms in the Boltzmann factor of Eq. 2.14 and its analogs. Similar behavior was observed for cases in which $V_{\rm AA}^1 = V_{\rm BB}^1$ and the strength of $V_{\rm AA}^2$ was increased.

We also investigated the temperature dependence of the kinetic paths in an alloy having a fixed ratio of interatomic interaction potentials. Figure 2.7 shows kinetic paths for an alloy in which $V_{\rm AA}^1 = 2V_{\rm BB}^1 = V_{\rm AA}^2 \equiv V$. Varying V, which is equivalent to varying $\frac{1}{T}$, gave widely differing kinetic paths. Here, decreasing the temperature (increasing V) enhances B2 ordering relative to $\rm D0_3$ ordering, although it does not affect qualitatively the two-step nature of the ordering process, *viz.*, initial B2 ordering followed by $\rm D0_3$ ordering. This temperature dependence is similar to that found in our experimental study of B2 and $\rm D0_3$ ordering in rapidly quenched $\rm Fe_3Al$ [9]. In the present work we also observed the greatest temperature dependence of kinetic paths for ratios of V parameters near those at the transition between no initial $\rm D0_3$ ordering and initial $\rm D0_3$ ordering.

It was determined empirically that the critical potential for $\rm D0_3$ ordering for an alloy in which $V_{\rm AA}^1 = V_{\rm BB}^1 = V_{\rm AA}^2 \equiv V$ is $V = 1.00$. This was done by varying V and observing at which point incipient $\rm D0_3$ ordering occurred. This critical potential of $V_c(\rm D0_3) = 1.00$ was corroborated by investigations of the stationary (equilibrium) points of the alloy. The left-hand sides of Eqs. 2.16–2.23 were set equal to zero, and values of $\{i, j, k, l, p, q, r, s\}$ which satisfied them were sought. Just below the critical potential for $\rm D0_3$ ordering ($V < V_c(\rm D0_3)$), the only stable stationary point (local minimum) occurs at $(i, j, k, l) = \left(\frac{N}{8} - \epsilon, \frac{N}{8} - \epsilon, \epsilon, \epsilon\right)$. This stationary point represents equilibrium B2 order. Just above the critical potential for $\rm D0_3$ ordering ($V > V_c(\rm D0_3)$), this stationary point bifurcates into

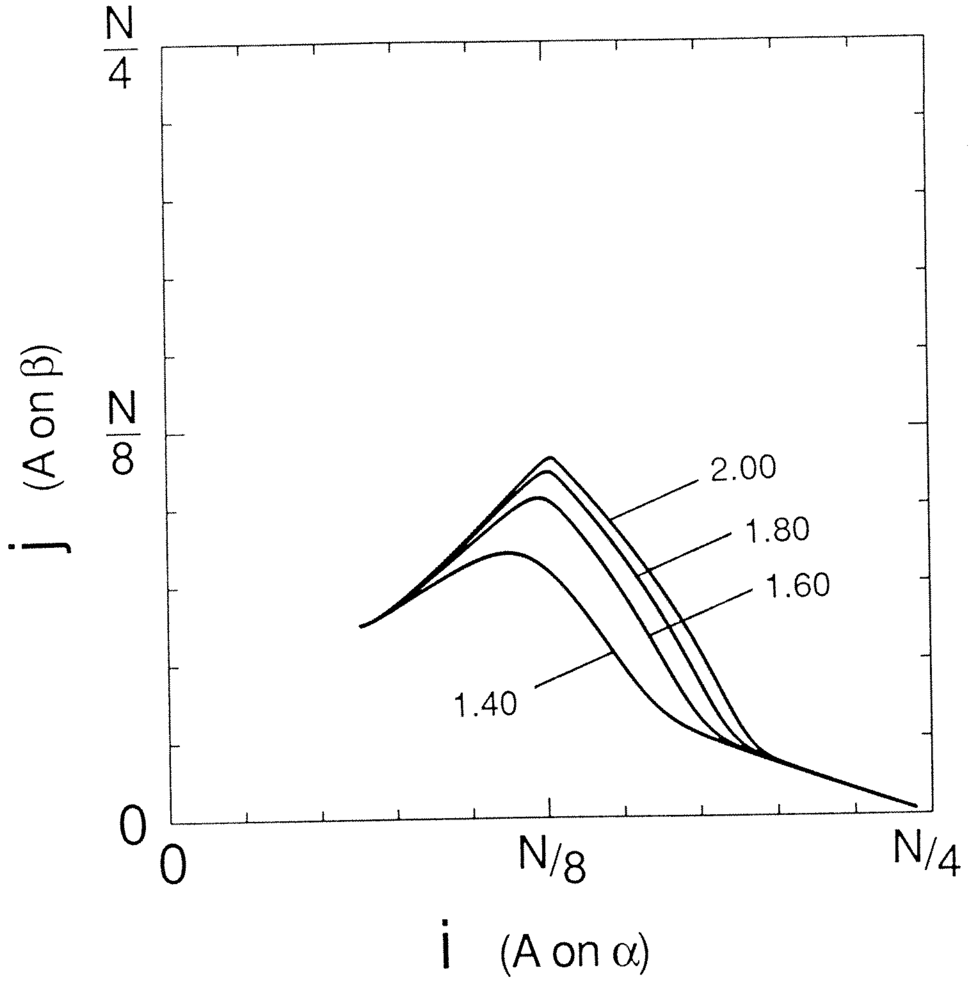

Figure 2.7: Kinetic paths depicting the dependence of the relative rates of B2 and $\mathrm{D0}_3$ ordering on temperature. Labels indicate values of V, where $V \equiv V^1_{\mathrm{AA}} = 2V^1_{\mathrm{BB}} = V^2_{\mathrm{AA}}$ ($V = 1.40 \Rightarrow T = 0.84T_c^{\mathrm{B2}} = 0.76T_c^{\mathrm{D0_3}}$; $V = 1.60 \Rightarrow T = 0.74T_c^{\mathrm{B2}} = 0.67T_c^{\mathrm{D0_3}}$; $V = 1.80 \Rightarrow T = 0.65T_c^{\mathrm{B2}} = 0.59T_c^{\mathrm{D0_3}}$; $V = 2.00 \Rightarrow T = 0.59T_c^{\mathrm{B2}} = 0.54T_c^{\mathrm{D0_3}}$).

two local minima, one corresponding to B2 order as before, and one at $(i, j, k, l) = \Big((\frac{N}{8} - \epsilon)(1 + \Delta), (\frac{N}{8} - \epsilon)(1 - \Delta), \epsilon, \epsilon\Big)$ corresponding to $D0_3$ order. From Eq. 2.4, Δ is just $S^{\alpha \cup \beta}_{D0_3}$ in the limit $\epsilon \to 0$. Further increases in V serve to increase Δ and consequently the amount of equilibrium $D0_3$ order in the alloy. These observations are consistent with a second-order phase transition at $V_c(D0_3) = 1.00$.

In a similar manner, the case in which $V^1_{AA} = V^1_{BB} \equiv V$ and V^2_{AA} is nonzero was studied for a range of values of V^2_{AA}/V. Critical potentials V_c(B2) and $V_c(D0_3)$ were obtained for various V^2_{AA}/V and are plotted in Fig. 2.8. Here, the V_c(B2) and $V_c(D0_3)$ correspond to the critical values of V. Similarly, Fig. 2.9 shows critical potentials for the case in which $V^1_{AA} = V^2_{AA} \equiv V$ and V^1_{BB} is nonzero. The dashed parts of the curves for V_c(B2) indicate the critical potentials at which incipient B2 ordering occurs *without simultaneous* $D0_3$ ordering. (The right-hand region of Fig. 2.8 and the left-hand region of Fig. 2.9, therefore, are not meant to indicate potentials for which $D0_3$ order can evolve without simultaneous B2 order.) The data of Fig. 2.6 were obtained above and below the cross-over point $V^1_{BB}/V \approx 0.55$ of Fig. 2.9. Figures 2.8 and 2.9 lend further support to our earlier argument that increasing V^2_{AA} and V^2_{BB} relative to V^1_{AA} and V^1_{BB} should enhance $D0_3$ ordering relative to B2 ordering. However, we hasten to remark that since $c_B > c_A$, increasing V^2_{BB} will affect $D0_3$ ordering differently from increasing V^2_{AA}.

We have also found it possible to form a third ordered structure corresponding to equal A atom occupancies on adjacent pairs of sublattices in Fig. 2.1, such as $\alpha \cup \gamma$ or $\alpha \cup \delta$. This is a partially ordered B32 structure. At low temperatures the B32 structure is not chosen in equilibrium over the $D0_3$ structure when 1nn interactions favor bonds between unlike atoms [12,13]. Nevertheless, we have observed the B32 structure as a transient kinetic phase when the 2nn interactions are very strong. In cases where the 1nn interactions favor bonds between unlike

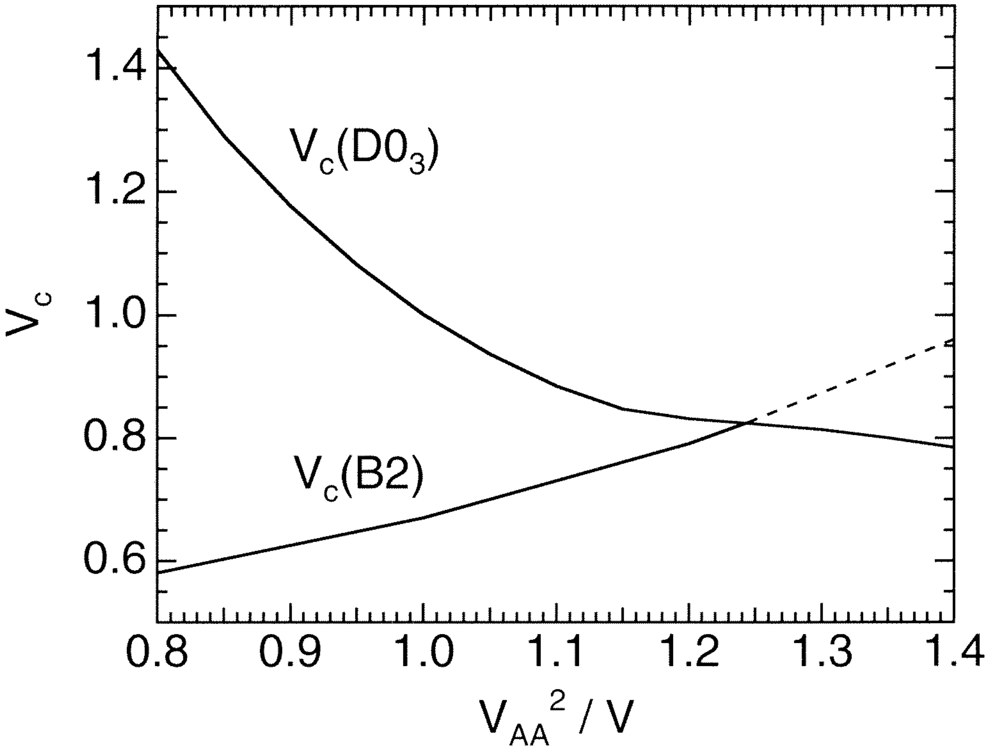

Figure 2.8: Critical potentials for B2 and D0$_3$ order as a function of V^2_{AA}/V, where $V^1_{\mathrm{AA}} = V^1_{\mathrm{BB}} \equiv V$. The dashed parts of the curves for V_c(B2) indicate the critical potentials at which incipient B2 ordering occurs *without simultaneous* D0$_3$ ordering.

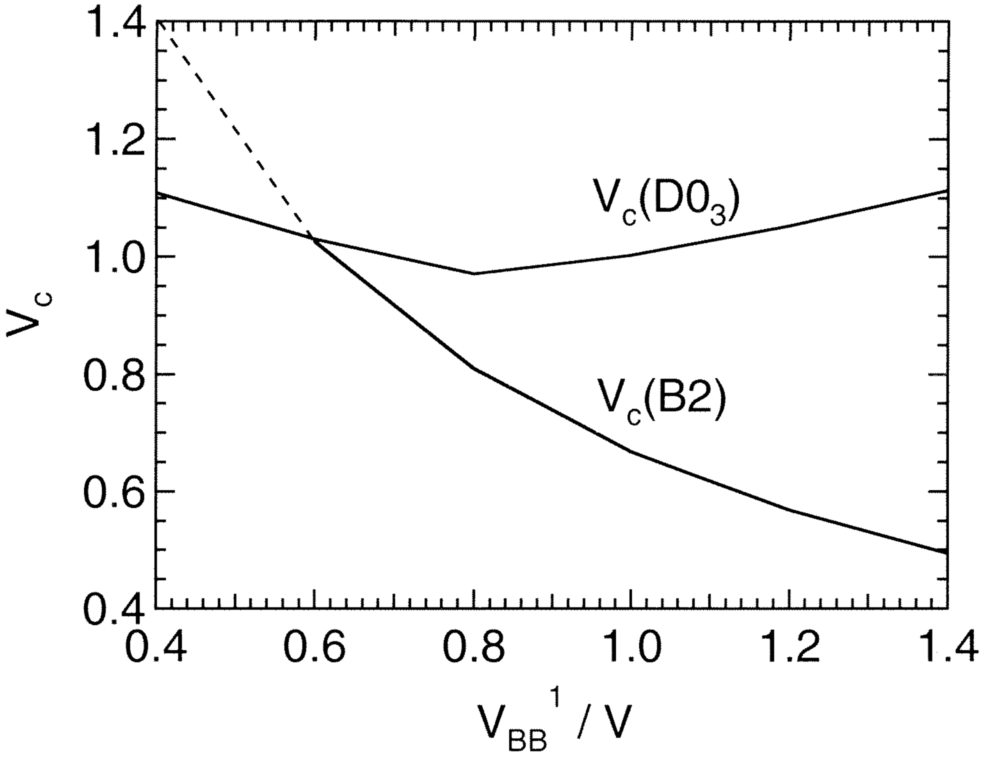

Figure 2.9: Critical potentials for B2 and $D0_3$ order as a function of V^1_{BB}/V, where $V^1_{\mathrm{AA}} = V^2_{\mathrm{AA}} \equiv V$. The dashed parts of the curves for V_c(B2) indicate the critical potentials at which incipient B2 ordering occurs *without simultaneous* $D0_3$ ordering.

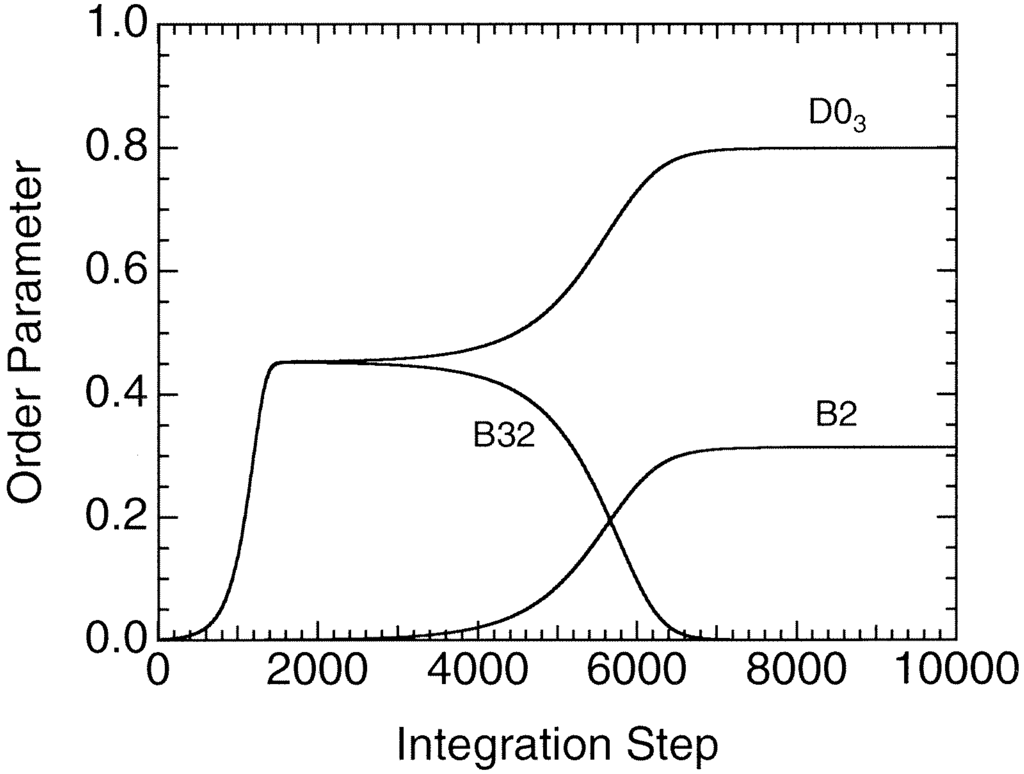

Figure 2.10: Evolution of B2, D0$_3$, and B32 order parameters ($V_{\mathrm{AA}}^1 = V_{\mathrm{AA}}^2 = 1.60$; $T = 3.38T_c^{\mathrm{B2}} = 0.67T_c^{\mathrm{D0_3}}$).

atoms, the kinetic path eventually leads away from this transient kinetic structure towards an equilibrium state with B2 as well as $D0_3$ order. An example of such a time-dependence of the B2, $D0_3$, and B32 order parameters is presented in Fig. 2.10. In this case there was a quick, and nearly equal, increase in the numbers of A atoms on the α and δ sublattices, while the number of A atoms on the β and γ sublattices approached zero. After about 4000 integration steps, the A atom population on the the δ sublattice began to decline, and the $D0_3$ and B2 order parameters increased to approximately their maximum values.

Figure 2.11 shows the evolution of the internal energy, configurational entropy, and free energy for the system of Fig. 2.10. All three quantities show a monotonic decrease as a function of integration step. Furthermore, all three quantities exhibit three distinct stages of quiescence. The first of these corresponds to the initial disordered state whereas the third corresponds to the final equilibrium state of B2 and $D0_3$ order. It is the second quiescent state which corresponds to the transient B32 state of Fig. 2.10, and the stationary nature of the free energy during this state that lends credence to the hypothesis that this transient B32 state corresponds to a nonequilibrium stationary point or saddle point in the free energy surface and is a pseudostable state.

We attempted to verify this conjecture by examining the free energy manifold for this particular choice of 1nn and 2nn interaction potentials. Unfortunately, even if we justifiably ignore the four order parameters or state variables p, q, r, and s, which correspond to vacancy occupancies on the four sublattices, we are still left with three independent variables among the four order parameters i, j, k, and l because of the constraint of Eq. 2.1. Displaying and visualizing such a three-dimensional free energy manifold can be daunting. For this reason, we chose

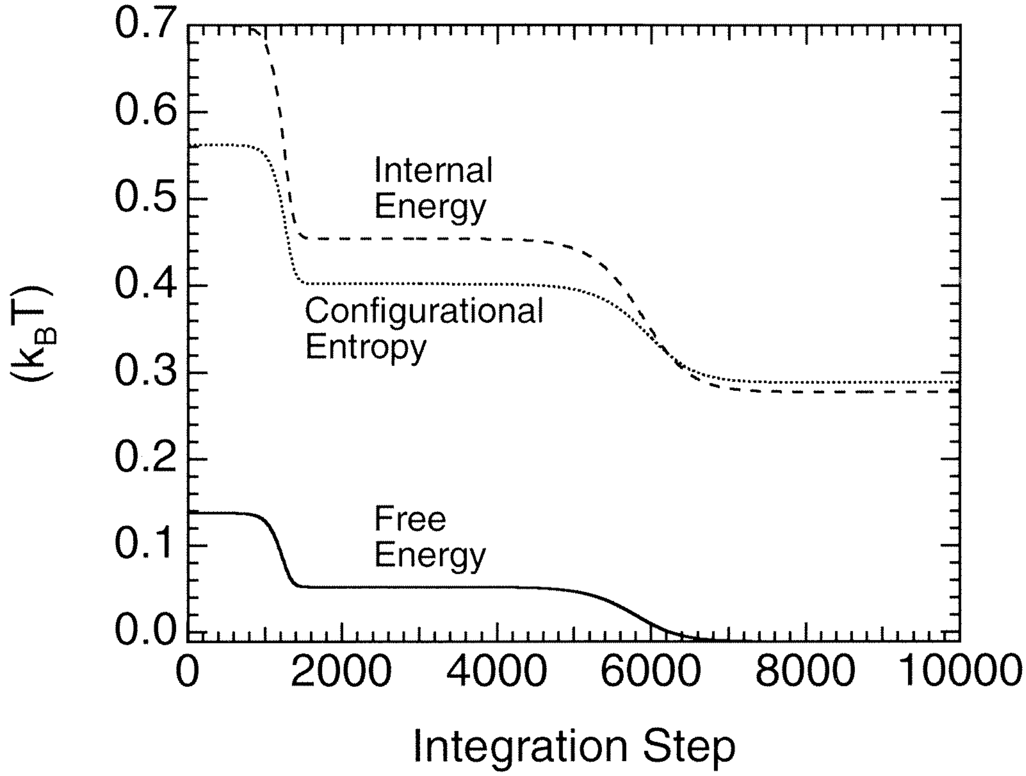

Figure 2.11: Evolution of the internal energy, configurational entropy, and the free energy for the system of Fig. 2.10 ($V^1_{\mathrm{AA}} = V^2_{\mathrm{AA}} = 1.60$; $T = 3.38T_c^{\mathrm{B2}} = 0.67T_c^{\mathrm{D0_3}}$).

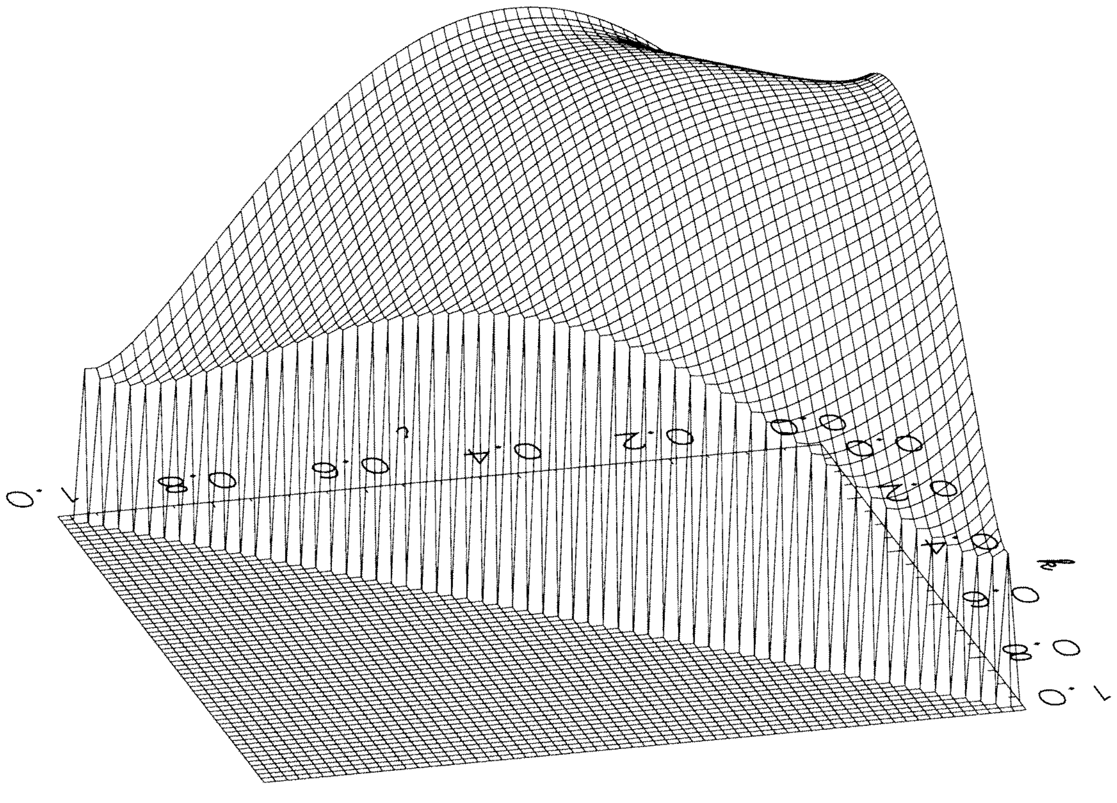

Figure 2.12: Surface plot of the free energy as a function of i and k for the system of Fig. 2.10 ($V^1_{\mathrm{AA}} = V^2_{\mathrm{AA}} = 1.60$; $T = 3.38T_c^{\mathrm{B2}} = 0.67T_c^{\mathrm{D0_3}}$).

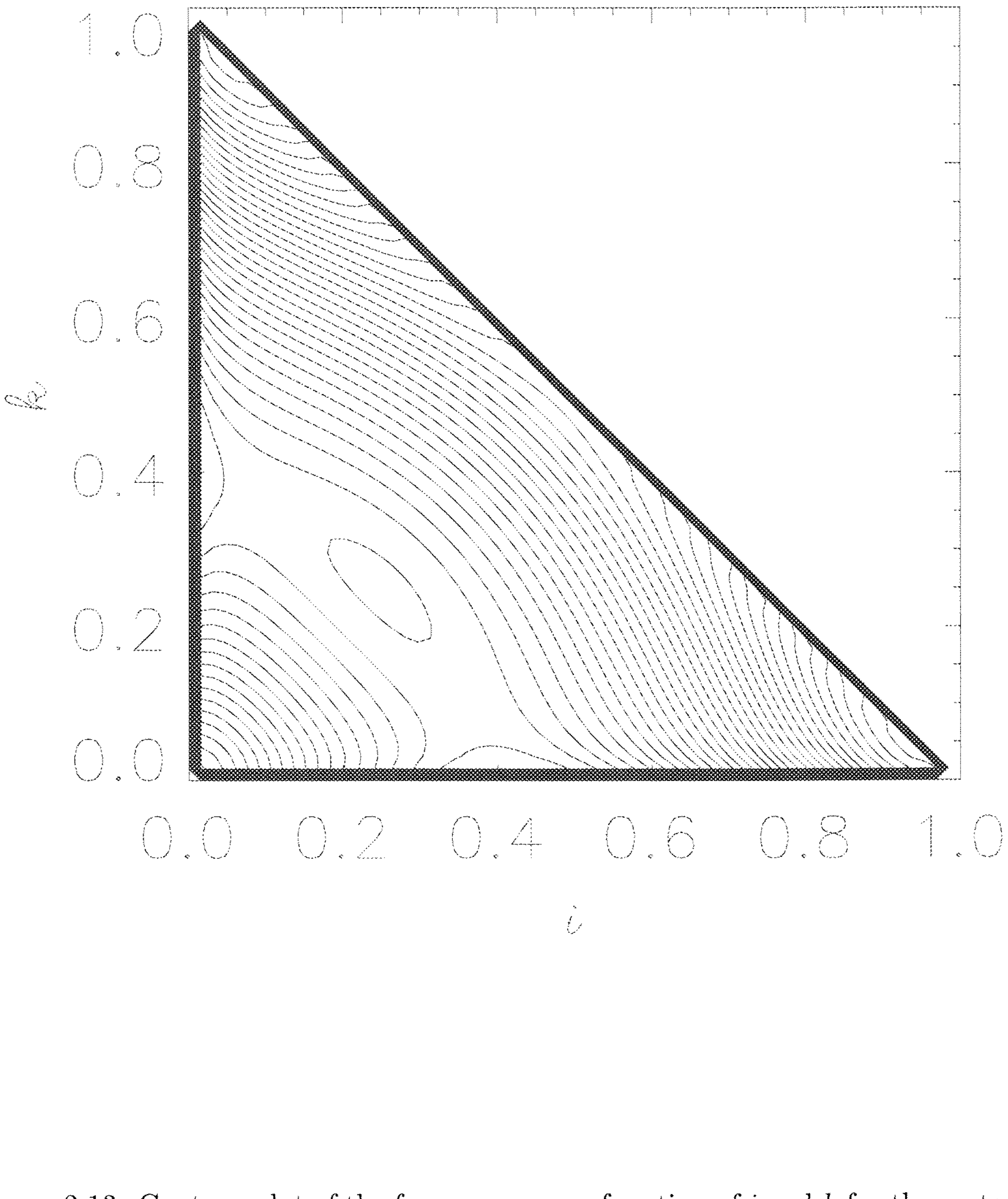

Figure 2.13: Contour plot of the free energy as a function of i and k for the system of Fig. 2.10 ($V^1_{\mathrm{AA}} = V^2_{\mathrm{AA}} = 1.60$; $T = 3.38T_c^{\mathrm{B2}} = 0.67T_c^{\mathrm{D0_3}}$).

to additionally impose the equality constraint

$$j = l. \tag{2.25}$$

Note that even though this is a somewhat artificial constraint, it is nevertheless a fairly reasonable one in that it still allows for the possibility of developing B2, $D0_3$, and B32 order. Equation 2.25 reduces the number of independent order parameters to two, say, i and k, and a two-dimensional free energy surface can be more readily visualized. Such a free energy surface is displayed as a function of i and k in Fig. 2.12. In preparing this free energy surface, we took N to be equal to 4, with the result that the maximum possible values of i, k, and $i + k$ was $c_{\mathrm{A}}N = 1$. For this reason, the range of allowed values of the ordered pair (i, k) is restricted to the triangle with vertices at $(0, 0)$, $(0, 1)$, and $(1, 0)$. To aid in visualizing Fig. 2.12, a contour plot of the same free energy surface is shown in Fig. 2.13.

The initial disordered state of Figs. 2.10 and 2.11 corresponds to the point $(i, k) = (0.25, 0.25)$ in Figs. 2.12 and 2.13. This point is a local maximum in the free energy surface and the system is in unstable equilibrium. Note that this is quite different from the initial disordered state at the point D in Fig. 1.7. In that figure, the axes correspond to short-range order parameters, in contrast to the axes of Figs. 2.12 and 2.13, which reflect long-range order parameters. Furthermore, the initial disordered state in Fig. 1.7 is *not* at a local maximum in the free energy surface, but sits on a steep slope in the free energy surface. This distinction is important for the following reason. A system that is at the point D in Fig. 1.7 will invariably move away from D in the general direction of the saddle point P since that is the direction of steepest descent. On the other hand, a system which is exactly at $(i, k) = (0.25, 0.25)$ in Figs. 2.12 and 2.13 will remain there indefinitely in the absence of external perturbations. In a real thermodynamic system at a finite nonzero temperature, there will always be thermal fluctuations which will provide the necessary perturbation to nudge the system off its apex. However, since there are no fluctuations in the analytical theory being considered here, it is necessary to introduce such a perturbation manually. This is what was done in the case of Figs. 2.10 and 2.11.

The kinetic path of the system initially took it from $(i, k) = (0.25, 0.25)$ to the neighborhood of $(i, k) \approx (0.5, 0.5)$, accompanied by a lowering of the free energy. The point near $(i, k) \approx (0.5, 0.5)$ corresponds to the transient B32 state observed in Fig. 2.10, and, as can be seen from Figs. 2.12 and 2.13, it is a saddle point in the free energy surface. This is entirely in keeping with our earlier conjecture. This saddle point is pseudostable, which helps account for the relatively long-lived nature of the transient B32 state. The system eventually leaves the neighborhood of the saddle point and evolves in the direction of the global minimum at $(i, k) \approx (1, 0)$ [or, equivalently, $(i, k) \approx (0, 1)$]. This corresponds to the disappearance of the transient B32 state and the development of equilibrium $D0_3$ order, as observed in Fig. 2.10.

We repeated the numerical integration of Fig. 2.10, but this time we set the the V^1_{AA} and V^2_{AA} potentials equal to zero after 10 000 integration steps. This corresponded to changing the temperature to ∞. By this time, equilibrium $D0_3$ and B2 order had developed. Figure 2.14 shows the variation of the B2, $D0_3$, and B32 order parameters that resulted. There was a very rapid decrease of the B2 and $D0_3$ order parameters to zero, but the time constant for the decay of $D0_3$ order was significantly greater than that of B2 order. Note that there was no appearance of a transient B32 state during the disordering process, unlike the case during the initial ordering stage.

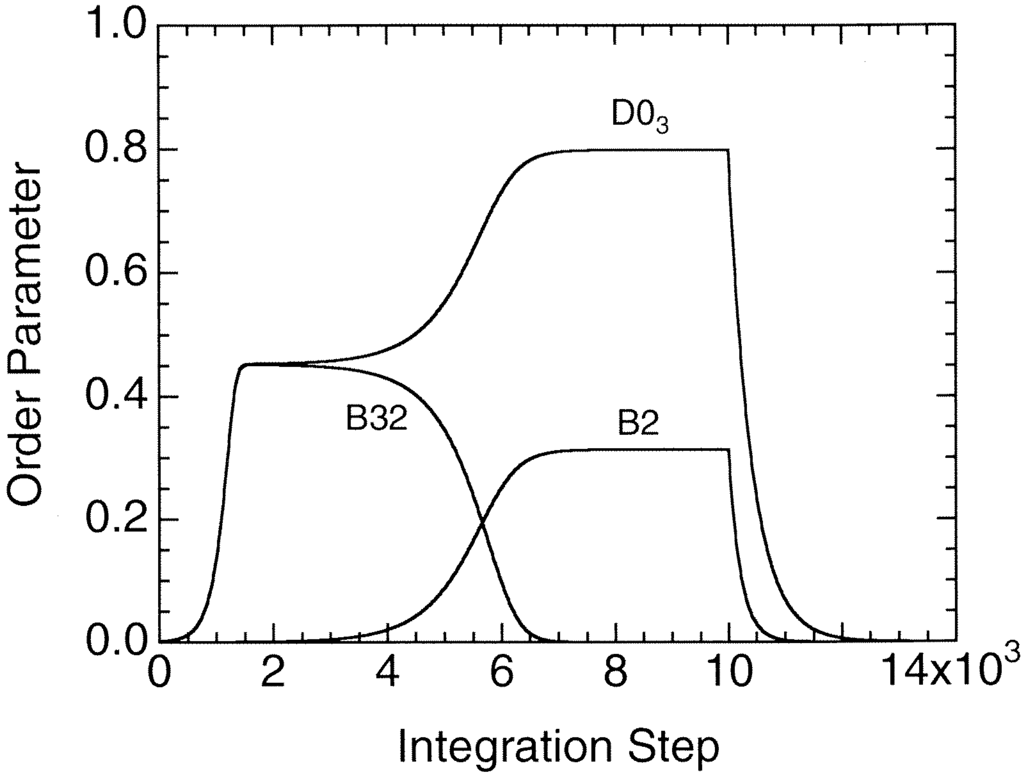

Figure 2.14: Evolution of B2, D0$_3$, and B32 order parameters ($V^1_{\mathrm{AA}} = V^2_{\mathrm{AA}} = 1.60$; $T = 3.38T_c^{\mathrm{B2}} = 0.67T_c^{\mathrm{D0_3}}$ for the first 10 000 steps and $V^1_{\mathrm{AA}} = V^2_{\mathrm{AA}} = 0.00$; $T = \infty$ thereafter).

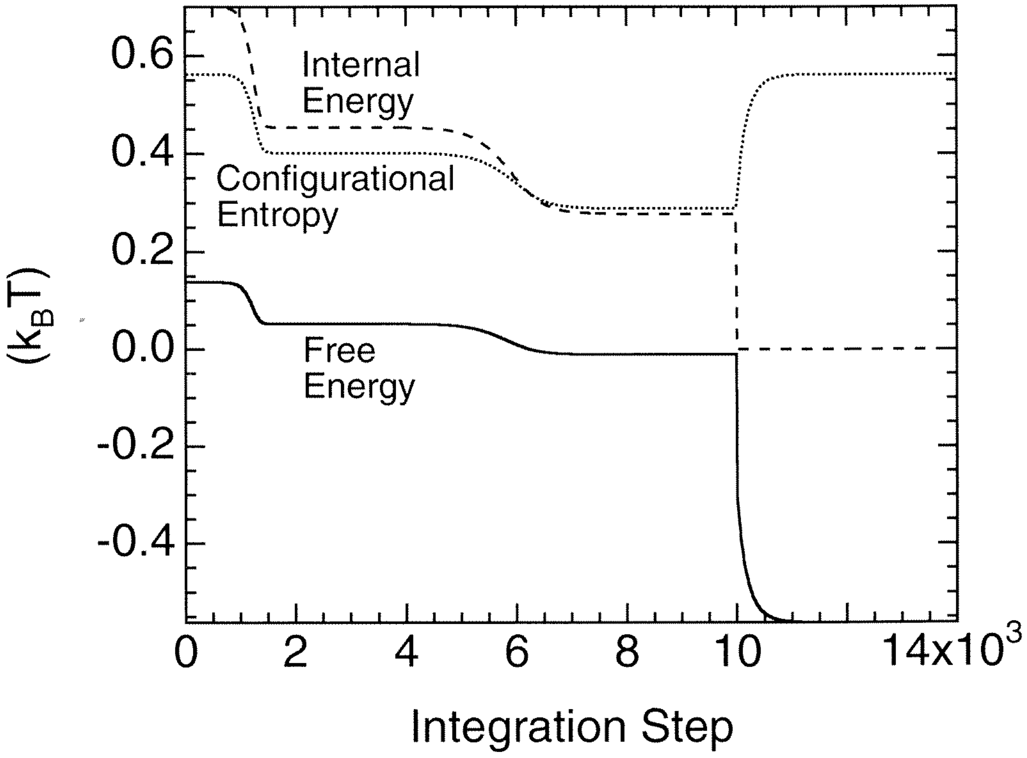

Figure 2.15: Evolution of the internal energy, configurational entropy, and the free energy for the system of Fig. 2.14 ($V^1_{\mathrm{AA}} = V^2_{\mathrm{AA}} = 1.60$; $T = 3.38T_c^{\mathrm{B2}} = 0.67T_c^{\mathrm{D0_3}}$ for the first 10 000 steps and $V^1_{\mathrm{AA}} = V^2_{\mathrm{AA}} = 0.00$; $T = \infty$ thereafter).

Figure 2.15 shows the corresponding variation of the internal energy, configurational entropy, and free energy. During the disordering stage, the internal energy is identically zero in the absence of any nonzero pair interaction potentials, whereas the configurational entropy rapidly returns to its initial (0 integration steps) value as the alloy recovers its initial random disordered configuration. During each of the two stages, ordering and disordering, the free energy decreases monotonically, as befitting an isothermal canonical ensemble.

2.1.5 Conclusions

We have developed a theory to describe the kinetic paths of ordering in alloys possessing both B2 and $D0_3$ order. For various values of the interatomic interaction energies, a rich variety of kinetic paths in $(S_{\mathrm{D0_3}}, S_{\mathrm{B2}})$-space was obtained during ordering of an initially disordered alloy. In general, a large value of V^2_{AA} relative to V^1_{AA} and V^1_{BB} tended to enhance the kinetics of $D0_3$ ordering relative to B2 ordering, changing the ordering process from one in which B2 ordering goes to completion before $D0_3$ ordering starts, through strong $D0_3$ ordering with the minimum consistent B2 ordering, to the case in which B32 order develops initially before being overtaken by $D0_3$ order. Although the B32 structure cannot be an equilibrium phase at low temperatures when 1nn interactions favor bonds between unlike atoms, in cases with very strong 2nn interactions we were able to observe a transient formation of B32 order before equilibrium B2 and $D0_3$ order developed. We were able to verify that this transient B32 structure corresponded to a saddle point in the free energy surface.

The kinetic paths also showed a marked dependence on the ordering temperature. For realistic $(V^1 > V^2)$ interactions, decreasing the annealing temperature tended to slow down the rate of $D0_3$ ordering relative to B2 ordering. This dependence of relative rates of ordering on annealing temperature suggests that by suitably varying the thermal treatments of these materials, it should be possible to choose from a wide variety of nonequilibrium combinations of B2 and $D0_3$ order.

2.2 The Path Probability Method in the Pair Approximation

A kinetic theory of ordering based on the path probability method was implemented in the pair (Bethe) approximation and used to study the kinetics of short- and long-range ordering in alloys with equilibrium states of B2, $D0_3$, or B32 order. The theory was developed in the superposition approximation for a vacancy mechanism on a bcc lattice with first- (1nn) and second-nearest neighbor (2nn) pair interactions. Chained 1nn conditional probabilities were used to account for the entropy of 2nn pair configurations. Comparisons are also made with the predictions from the kinetic theory of Section 2.1, which was implemented in the point (Bragg-Williams) approximation. For both calculations (point and pair), critical temperatures for B2 and $D0_3$ ordering are reported for different 1nn and 2nn interaction strengths. The influence of annealing temperature on the kinetic paths through the space of B2, $D0_3$, and B32 order parameters was found to be strong when the thermodynamic preferences of the alloy were not too great. Transient states of intermediate order were also studied. A transient formation of B32 order in an AB_3 alloy was found when 2nn interactions were strong, even when B32 order was neither a Richards-Allen-Cahn ground state nor a stable equilibrium state at that temperature. The formation of this transient B32 order can be argued consistently from a thermodynamic perspective. (However, as will be demonstrated in the next chapter, a second example of transient B2 order in an AB alloy with equilibrium B32 order cannot be explained by the same thermodynamic argument, and we believe that its origin is primarily kinetic.)

2.2.1 Introduction

In a previous section of this chapter, we developed and implemented a kinetic theory of B2 and $D0_3$ ordering using a master equation method (MEM) in the point (Bragg-Williams) approximation [14]. Those efforts were motivated by our experimental work on ordering kinetics in Fe_3Al [9]. In this section, we formulate an alternate theory of ordering in bcc alloys using the pair (Bethe) approximation and the 4-sublattice model of the previous theory. In addition to the increased accuracy obtained by using a larger base cluster, *viz.*, the pair instead of the point, the new theory also provides short-range order (SRO) parameters. It is interesting to identify the qualitative similarities of the long-range order (LRO) kinetics in the point and pair approximations. The point and pair approximations were compared by examining their predictions of the "kinetic paths" taken by the alloy.

One of the more surprising results from our work using the MEM in the point approximation [14] was the observation of transient B32 order that occurred for certain choices of the interaction potentials, particularly ones where the 2nn interactions were quite strong relative to the 1nn interactions, but both favored the formation of unlike pairs. Under these conditions, B32 order was neither a Richards-Allen-Cahn ground state [12,13] nor a stable equilibrium state at that temperature. Surprisingly, however, B32 order appeared transiently during the disorder→order transformation. This transient B32 order was not metastable in that it did not correspond to a local minimum in the free energy surface. One of the members of our group has obtained experimental evidence for the formation of such a pseudostable B32 state during low-temperature annealings of disordered

Fe_3Al [15]. Recent theoretical investigations have suggested that such transient or *pseudostable* states may correspond to saddle points in the free energy surface [16]. In the course of calculating kinetic paths of ordering, we found examples of transient states of order that are nonintuitive from thermodynamic arguments. We made some effort to maximize the appearance of these transient states, and we discuss them here.

2.2.2 Theory

One of the earliest successful applications [17,18] of the path probability method (PPM) was to the study of the kinetics of disorder→order transformations in binary body-centered cubic (bcc) alloys [1,19]. The present derivation is based on the PPM in the pair approximation. It applies to a bcc binary[3] alloy with first- (1nn) and second-nearest-neighbor (2nn) interactions, and which can have B2, $D0_3$, or B32 ordered structures. Vacancy motion is assumed to occur only between 1nn sites. The three species are the vacancies V, and the two atomic species A and B. They will be denoted by subscripts 0, 1, and 2, respectively. The four fcc sublattices are denoted α, β, γ, and δ [14]. In the manner of Sato and Kikuchi [1], we introduce the state variables, which describe the state of the system at time t. The probability that a ζ lattice site is occupied by the species i is $x_i^\zeta(t)$, where $\zeta \in \{\alpha, \beta, \gamma, \delta\}$, and $i \in \{0, 1, 2\}$. There are $4 \times 3 = 12$ such x state variables.

Similarly, the probability that *adjacent* lattice sites on the ζ and η sublattices are occupied by the species i and j, respectively, is $y_{ij}^{\zeta\eta}(t)$, where $(\zeta, \eta) \in \{(\alpha, \gamma), (\alpha, \delta), (\beta, \gamma), (\beta, \delta)\}$, and $i, j \in \{0, 1, 2\}$. There are $4 \times 3^2 = 36$ such y state variables. Note that in our notation, $y_{ij}^{\zeta\eta}(t) \equiv y_{ji}^{\eta\zeta}(t)$. (Table 2.1 summarizes

---

[3] It is straightforward to extend the derivation to ternary and quaternary alloys.

these and other definitions.)

In the manner of Sato and Kikuchi [1], we write the following constraints:

$$1 = \sum_{i=0}^{2} x_i^{\zeta}(t), \tag{2.26}$$

$$x_i^{\zeta}(t) = \sum_{j=0}^{2} y_{ij}^{\zeta\eta}(t). \tag{2.27}$$

There are a total of 1 × 4 × 1 = 4 constraints of the type in Eq. 2.26, and a total of 4 × 2 × 3 = 24 constraints of the type in Eq. 2.27.

Atom conservation requires:

$$x_i^{\alpha}(t) + x_i^{\beta}(t) + x_i^{\gamma}(t) + x_i^{\delta}(t) = 4\rho_i, \tag{2.28}$$

where ρ_i is the overall time-independent concentration of species i, and $i \in \{0, 1, 2\}$. There are a total of 3 such constraints. Furthermore, the ρ_i satisfy the closure relation:

$$\sum_{i=0}^{2} \rho_i = 1. \tag{2.29}$$

We also write the B2, $D0_3$, and B32 LRO parameters in terms of the x state variables. The conventional LRO parameters for B2 and $D0_3$ order are:

$$S_{\mathrm{B2}} \equiv |(x_1^{\alpha}(t) + x_1^{\beta}(t)) - (x_1^{\gamma}(t) + x_1^{\delta}(t))|, \tag{2.30}$$

$$S_{\mathrm{D0_3}}^{\alpha\cup\beta} \equiv x_1^{\alpha}(t) - x_1^{\beta}(t), \tag{2.31}$$

$$S_{\mathrm{D0_3}}^{\gamma\cup\delta} \equiv x_1^{\gamma}(t) - x_1^{\delta}(t), \tag{2.32}$$

$$S_{\mathrm{D0_3}} \equiv \mathrm{Max}(|S_{\mathrm{D0_3}}^{\alpha\cup\beta}|, |S_{\mathrm{D0_3}}^{\gamma\cup\delta}|), \tag{2.33}$$

where $0 \leq S_{\mathrm{B2}}, S_{\mathrm{D0_3}} \leq 1$. Following our previous work [14], we find it convenient to define order parameters for B32 order in terms of those for $D0_3$ order:

$$\begin{aligned} S_{\mathrm{B32}}^{\alpha\cup\gamma} &\equiv S_{\mathrm{D0_3}}^{\alpha\cup\beta} + S_{\mathrm{D0_3}}^{\gamma\cup\delta} - \mathrm{Max}(S_{\mathrm{D0_3}}^{\alpha\cup\beta}, S_{\mathrm{D0_3}}^{\gamma\cup\delta}) \\ &\equiv -S_{\mathrm{B32}}^{\beta\cup\delta}, \end{aligned} \tag{2.34}$$

$$\begin{aligned} S_{\mathrm{B32}}^{\alpha\cup\delta} &\equiv S_{\mathrm{D0_3}}^{\alpha\cup\beta} - S_{\mathrm{D0_3}}^{\gamma\cup\delta} - \mathrm{Max}(S_{\mathrm{D0_3}}^{\alpha\cup\beta}, -S_{\mathrm{D0_3}}^{\gamma\cup\delta}) \\ &\equiv -S_{\mathrm{B32}}^{\beta\cup\gamma}, \end{aligned} \tag{2.35}$$

$$S_{\mathrm{B32}} \equiv \mathrm{Max}(|S_{\mathrm{B32}}^{\alpha\cup\gamma}|, |S_{\mathrm{B32}}^{\alpha\cup\delta}|), \tag{2.36}$$

where $0 \leq S_{\mathrm{B32}} \leq 1$ and the third term in Eqs. 2.34 and 2.35 is subtracted, somewhat artificially, to distinguish B32 order from $\mathrm{D0_3}$ order.

In a parallel manner, we can write the path variables corresponding to the state variables. Following Kikuchi [17,18], the path variables are denoted by the corresponding upper-case letters. They represent the probability of a particular change in the corresponding state-variable in an infinitesimal time Δt. For instance, the probability that a lattice point on the ζ sublattice is occupied by an i species at time t and by an i' species at time $t + \Delta t$ is written as $X_{i;i'}^{\zeta}(t, t+\Delta t)$. Corresponding quantities can be written for the pair path variables, *viz.*, $Y_{ij;i'j'}^{\zeta\eta}(t, t + \Delta t)$. Since we are implicitly assuming a vacancy mechanism of ordering with nearest-neighbor jumps, only those path variables represented in Tbls. 2.2 and 2.3 are allowed. It is necessary to assign a "weight" to each path variable in order to account for its degeneracy.

Consider an i atom ($i \neq 0$) on a ζ sublattice. Its neighbor atoms will affect its energy through the pair potentials V_{ij}^1 and V_{ij}^2, and this chemical energy will affect its probability of exchange with a vacancy neighbor. $\Lambda_i^{\zeta\eta}$ is the average Boltzmann factor contributing to the jump probability of that i atom from an atom on the 1nn η sublattice. $\Lambda_i'^{\zeta\eta}$ is the average Boltzmann factor for that i atom from an atom on the 2nn η sublattice. For instance,

$$\Lambda_i^{\alpha\gamma} = \sum_{j=0}^{2} y_{ij}^{\alpha\gamma} \exp(V_{ij}^1) \tag{2.37}$$

$$\Lambda_i'^{\alpha\beta} = \sum_{j=0}^{2} \sum_{k=0}^{2} y_{ik}^{\alpha\gamma} (y_{jk}^{\beta\gamma} / x_k^{\gamma}) \exp(V_{ij}^2), \tag{2.38}$$

Path Variable	Weight	Note	Number of distinct variables
$X^{\zeta}_{i;i}(t, t+\Delta t)$	1		$4 \times 3 = 12$
$X^{\zeta}_{i;0}(t, t+\Delta t)$	8	$i \neq 0$	$4 \times 2 = 8$
$X^{\zeta}_{0;i}(t, t+\Delta t)$	8	$i \neq 0$	$4 \times 2 = 8$
			Total $= 28$

Table 2.2: The path variables for a point. Unless it is stated otherwise, $\zeta \in \{\alpha, \beta, \gamma, \delta\}$ and $i \in \{0, 1, 2\}$.

Path Variable	Weight	Note	Number of distinct variables
$Y^{\zeta\eta}_{ij;ij}(t, t+\Delta t)$	1		$4 \times 3 \times 3 = 36$
$Y^{\zeta\eta}_{ij;i0}(t, t+\Delta t)$	7	$j \neq 0$	$4 \times 3 \times 2 = 24$
$Y^{\zeta\eta}_{ij;0j}(t, t+\Delta t)$	7	$i \neq 0$	$4 \times 2 \times 3 = 24$
$Y^{\zeta\eta}_{i0;ij}(t, t+\Delta t)$	7	$j \neq 0$	$4 \times 3 \times 2 = 24$
$Y^{\zeta\eta}_{0j;ij}(t, t+\Delta t)$	7	$i \neq 0$	$4 \times 2 \times 3 = 24$
$Y^{\zeta\eta}_{i0;0i}(t, t+\Delta t)$	1	$i \neq 0$	$4 \times 2 = 8$
$Y^{\zeta\eta}_{0j;j0}(t, t+\Delta t)$	1	$j \neq 0$	$4 \times 2 = 8$
			Total $= 148$

Table 2.3: The path variables for a pair. Unless it is stated otherwise, $(\zeta, \eta) \in \{(\alpha, \gamma), (\alpha, \delta), (\beta, \gamma), (\beta, \delta)\}$, $i \in \{0, 1, 2\}$, and $j \in \{0, 1, 2\}$.

where $i \in \{1, 2\}$. Since our base cluster is a 1nn pair, we use a sum over conditional probabilities $\sum_{k=0}^{2} y_{ik}^{\alpha\gamma}(y_{jk}^{\beta\gamma}/x_k^{\gamma})$ in Eq. 2.38 above to obtain the 2nn pair probabilities. Similar expressions exist for $\Lambda_i^{\alpha\delta}$, $\Lambda_i^{\beta\gamma}$, $\Lambda_i^{\beta\delta}$, $\Lambda_i^{\gamma\alpha}$, $\Lambda_i^{\gamma\beta}$, $\Lambda_i^{\delta\alpha}$, $\Lambda_i^{\delta\beta}$, $\Lambda_i'^{\gamma\delta}$, $\Lambda_i'^{\beta\alpha}$, and $\Lambda_i'^{\delta\gamma}$. Also, $\Gamma_i^{\zeta\eta}$ is the total Boltzmann factor for a jump of that i atom from the ζ sublattice onto a 1nn vacant site on the η sublattice. For instance,

$$\Gamma_i^{\alpha\gamma} = (\Lambda_i^{\alpha\gamma}/x_i^{\alpha})^3 (\Lambda_i^{\alpha\delta}/x_i^{\alpha})^4 (\Lambda_i'^{\alpha\beta}/x_i^{\alpha})^6, \tag{2.39}$$

where $i \in \{1, 2\}$. The exponents 3, 4, and 6 in Eq. 2.39 above arise from the fact that the i atom on the α sublattice which is about to jump onto the γ sublattice has 3 neighbors on the γ sublattice, [4] 4 neighbors on the δ sublattice, and 6 neighbors on the β sublattice. Similar expressions exist for $\Gamma_i^{\alpha\delta}$, $\Gamma_i^{\beta\gamma}$, $\Gamma_i^{\beta\delta}$, $\Gamma_i^{\gamma\alpha}$, $\Gamma_i^{\gamma\beta}$, $\Gamma_i^{\delta\alpha}$, and $\Gamma_i^{\delta\beta}$.

With the above definitions, it is now possible to obtain expressions for the $Y_{ij;i'j'}^{\zeta\eta}(t, t + \Delta t)$ path variables.[5] There are three classes of $Y_{ij;i'j'}^{\zeta\eta}(t, t + \Delta t)$ path variables. The first set of $Y_{ij;i'j'}^{\zeta\eta}(t, t + \Delta t)$ path variables accounts for the probability that the pair configuration does not change in the interval Δt:

$$Y_{ij;ij}^{\zeta\eta}(t, t + \Delta t) = y_{ij}^{\zeta\eta}(t), \tag{2.40}$$

where $(\zeta, \eta) \in \{(\alpha, \gamma), (\alpha, \delta), (\beta, \gamma), (\beta, \delta)\}$ and $i, j \in \{0, 1, 2\}$.

The second set of $Y_{ij;i'j'}^{\zeta\eta}(t, t + \Delta t)$ path variables accounts for the probability that one of the members of the pair configuration changes identity due to a vacancy-atom interchange between that site and one other neighboring site. For instance:

$$Y_{ij;i0}^{\alpha\gamma}(t, t + \Delta t) = \frac{y_{ij}^{\alpha\gamma}(t) \exp(V_{ij}^{1})}{\Lambda_j^{\gamma\alpha}}$$

---

[4] One of the sites on the γ sublattice is the soon-to-be-occupied vacancy.

[5] It is not necessary to work with the $X_{i;i'}^{\zeta}(t, t + \Delta t)$ path variables in order to compute the $x_i^{\zeta}(t)$ state variables. The $x_i^{\zeta}(t)$ point state variables can more conveniently be obtained from the $y_{ij}^{\zeta\eta}(t)$ pair state variables.

$$\times \left[\frac{3}{7} y_{0j}^{\alpha\gamma}(t)\Gamma_j^{\gamma\alpha} + \frac{4}{7} y_{0j}^{\beta\gamma}(t)\Gamma_j^{\gamma\beta}\right], \tag{2.41}$$

$$Y_{i0;ij}^{\alpha\gamma}(t, t+\Delta t) = \frac{y_{i0}^{\alpha\gamma}(t)}{x_0^{\gamma}} \times \left[\frac{3}{7} y_{j0}^{\alpha\gamma}(t)\Gamma_j^{\alpha\gamma} + \frac{4}{7} y_{j0}^{\beta\gamma}(t)\Gamma_j^{\beta\gamma}\right], \tag{2.42}$$

where $i \in \{0, 1, 2\}$, and $j \in \{1, 2\}$. Similar expressions exist for $Y_{ij;i0}^{\alpha\delta}$, $Y_{i0;ij}^{\alpha\delta}$, $Y_{ij;i0}^{\beta\gamma}$, $Y_{i0;ij}^{\beta\gamma}$, $Y_{ij;i0}^{\beta\delta}$, $Y_{i0;ij}^{\beta\delta}$, $Y_{ij;0j}^{\alpha\gamma}$, $Y_{0j;ij}^{\alpha\gamma}$, $Y_{ij;0j}^{\alpha\delta}$, $Y_{0j;ij}^{\alpha\delta}$, $Y_{ij;0j}^{\beta\gamma}$, $Y_{0j;ij}^{\beta\gamma}$, $Y_{ij;0j}^{\beta\delta}$, and $Y_{0j;ij}^{\beta\delta}$.

The third set of $Y_{ij;i'j'}^{\zeta\eta}(t, t+\Delta t)$ path variables deals with a vacancy-atom exchange occurring between the two sites of the pair:

$$Y_{i0;0i}^{\zeta\eta}(t, t+\Delta t) = y_{i0}^{\zeta\eta}(t)\Gamma_i^{\zeta\eta}, \tag{2.43}$$

$$Y_{0i;i0}^{\zeta\eta}(t, t+\Delta t) = y_{0i}^{\zeta\eta}(t)\Gamma_i^{\eta\zeta}, \tag{2.44}$$

where $(\zeta, \eta) \in \{(\alpha, \gamma), (\alpha, \delta), (\beta, \gamma), (\beta, \delta)\}$ and $i \in \{1, 2\}$.

By identifying the path variables that connect the state variables at time t with the state variables at time $t + \Delta t$, and using a subscripted δ for the Kronecker delta function, we obtain the following relations:

$$x_i^{\zeta}(t) = X_{i;i}^{\zeta}(t, t+\Delta t) + 8(1-\delta_{i0})X_{i;0}^{\zeta}(t, t+\Delta t) + 8\delta_{i0}\sum_{m\neq 0} X_{i;m}^{\zeta}(t, t+\Delta t), \tag{2.45}$$

$$x_i^{\zeta}(t+\Delta t) = X_{i;i}^{\zeta}(t, t+\Delta t) + 8(1-\delta_{i0})X_{0;i}^{\zeta}(t, t+\Delta t) + 8\delta_{i0}\sum_{m\neq 0} X_{m;i}^{\zeta}(t, t+\Delta t), \tag{2.46}$$

where $\zeta \in \{\alpha, \beta, \gamma, \delta\}$.

$$\begin{aligned} y_{ij}^{\zeta\eta}(t) = {} & Y_{ij;ij}^{\zeta\eta}(t, t+\Delta t) \\ & + 7(1-\delta_{i0})Y_{ij;0j}^{\zeta\eta}(t, t+\Delta t) + 7(1-\delta_{j0})Y_{ij;i0}^{\zeta\eta}(t, t+\Delta t) \\ & + 7\delta_{i0}\sum_{m\neq 0} Y_{ij;mj}^{\zeta\eta}(t, t+\Delta t) + 7\delta_{j0}\sum_{m\neq 0} Y_{ij;im}^{\zeta\eta}(t, t+\Delta t) \end{aligned}$$

$$+ \Big[\delta_{i0}(1-\delta_{j0}) + \delta_{j0}(1-\delta_{i0})\Big] Y^{\zeta\eta}_{ij;ji}(t, t+\Delta t), \tag{2.47}$$

$$\begin{aligned}
y^{\zeta\eta}_{ij}(t+\Delta t) &= Y^{\zeta\eta}_{ij;ij}(t, t+\Delta t) \\
&+ 7(1-\delta_{i0}) Y^{\zeta\eta}_{0j;ij}(t, t+\Delta t) + 7(1-\delta_{j0}) Y^{\zeta\eta}_{i0;ij}(t, t+\Delta t) \\
&+ 7\delta_{i0} \sum_{m\neq 0} Y^{\zeta\eta}_{mj;ij}(t, t+\Delta t) + 7\delta_{j0} \sum_{m\neq 0} Y^{\zeta\eta}_{im;ij}(t, t+\Delta t) \\
&+ \Big[\delta_{i0}(1-\delta_{j0}) + \delta_{j0}(1-\delta_{i0})\Big] Y^{\zeta\eta}_{ji;ij}(t, t+\Delta t),
\end{aligned} \tag{2.48}$$

where $(\zeta, \eta) \in \{(\alpha,\gamma), (\alpha,\delta), (\beta,\gamma), (\beta,\delta)\}$.

The changes in the state variables can then be written as:

$$\begin{aligned}
\Delta x^{\zeta}_{i} &\equiv x^{\zeta}_{i}(t+\Delta t) - x^{\zeta}_{i}(t) \\
&= 8(1-\delta_{i0})\Big[X^{\zeta}_{0;i}(t, t+\Delta t) - X^{\zeta}_{i;0}(t, t+\Delta t)\Big] \\
&+ 8\delta_{i0} \sum_{m\neq 0} \Big[X^{\zeta}_{m;i}(t, t+\Delta t) - X^{\zeta}_{i;m}(t, t+\Delta t)\Big],
\end{aligned} \tag{2.49}$$

where $\zeta \in \{\alpha, \beta, \gamma, \delta\}$.

$$\begin{aligned}
\Delta y^{\zeta\eta}_{ij} &\equiv y^{\zeta\eta}_{ij}(t+\Delta t) - y^{\zeta\eta}_{ij}(t) \\
&= 7(1-\delta_{i0})\Big[Y^{\zeta\eta}_{0j;ij}(t, t+\Delta t) - Y^{\zeta\eta}_{ij;0j}(t, t+\Delta t)\Big] \\
&+ 7(1-\delta_{j0})\Big[Y^{\zeta\eta}_{i0;ij}(t, t+\Delta t) - Y^{\zeta\eta}_{ij;i0}(t, t+\Delta t)\Big] \\
&+ 7\delta_{i0} \sum_{m\neq 0} \Big[Y^{\zeta\eta}_{mj;ij}(t, t+\Delta t) - Y^{\zeta\eta}_{ij;mj}(t, t+\Delta t)\Big] \\
&+ 7\delta_{j0} \sum_{m\neq 0} \Big[Y^{\zeta\eta}_{im;ij}(t, t+\Delta t) - Y^{\zeta\eta}_{ij;im}(t, t+\Delta t)\Big] \\
&+ \Big[\delta_{i0}(1-\delta_{j0}) + \delta_{j0}(1-\delta_{i0})\Big] \\
&\times \Big[Y^{\zeta\eta}_{ji;ij}(t, t+\Delta t) - Y^{\zeta\eta}_{ij;ji}(t, t+\Delta t)\Big],
\end{aligned} \tag{2.50}$$

where $(\zeta, \eta) \in \{(\alpha,\gamma), (\alpha,\delta), (\beta,\gamma), (\beta,\delta)\}$.

For the most probable path, the path variable for, say, $Y^{\gamma\alpha}_{i0;0i}(t, t+\Delta t)$ is proportional to:

- the probability of the corresponding initial state, $y^{\gamma\alpha}_{i0}(t)$,

- the attempt frequency of the atom belonging to species i, ν_i,
- the corresponding Boltzmann factor for the jump, $\Gamma_{i0}^{\gamma\alpha}$,
- the time interval, Δt.

The Boltzmann factor, $\Gamma_{i0}^{\gamma\alpha}$, depends on the identities of the 1nn's and 2nn's of the jumping atom of species i. Of these neighboring atoms, $\frac{z}{2} - 1$ are on the α sublattice $\frac{z}{2}$ are on the β sublattice, and z' are on the δ sublattice.

In the limit $\Delta t \rightarrow 0$, Eq. 2.50 results in a set of coupled nonlinear first-order differential equations, which may be integrated to obtain the kinetic path of the alloy. The numerical integrations were performed for a variety of initial configurations and interaction energies $\{V\}$. The computer code was written in C and executed on a DECstation 3100. A fourth-order Runge-Kutta method with adaptive step-size control was used to integrate the differential equations.

2.2.3 Results and Discussion

Kinetic and Thermodynamic Trends

The steady state of any viable kinetic theory of ordering and disordering should be the appropriate state of thermodynamic equilibrium. In particular, the kinetic theory in the pair approximation should be consistent with the cluster variation method (CVM) in the pair approximation. This is what we found when we calculated the critical temperatures for B2 and $\mathrm{D0_3}$ LRO using our kinetic theory in the pair approximation. Figure 2.16 shows the resulting critical potentials for B2 and $\mathrm{D0_3}$ order as a function of V_{AA}^2/V. These curves were obtained by considering alloys which had $V_{\mathrm{AA}}^1 = V_{\mathrm{BB}}^1 \equiv V$ and V_{AA}^2 as the only nonzero pair potentials, varying V for a fixed ratio of V_{AA}^2/V. This is equivalent to maintaining the same interatomic potentials and varying the temperature. We tried a range of different

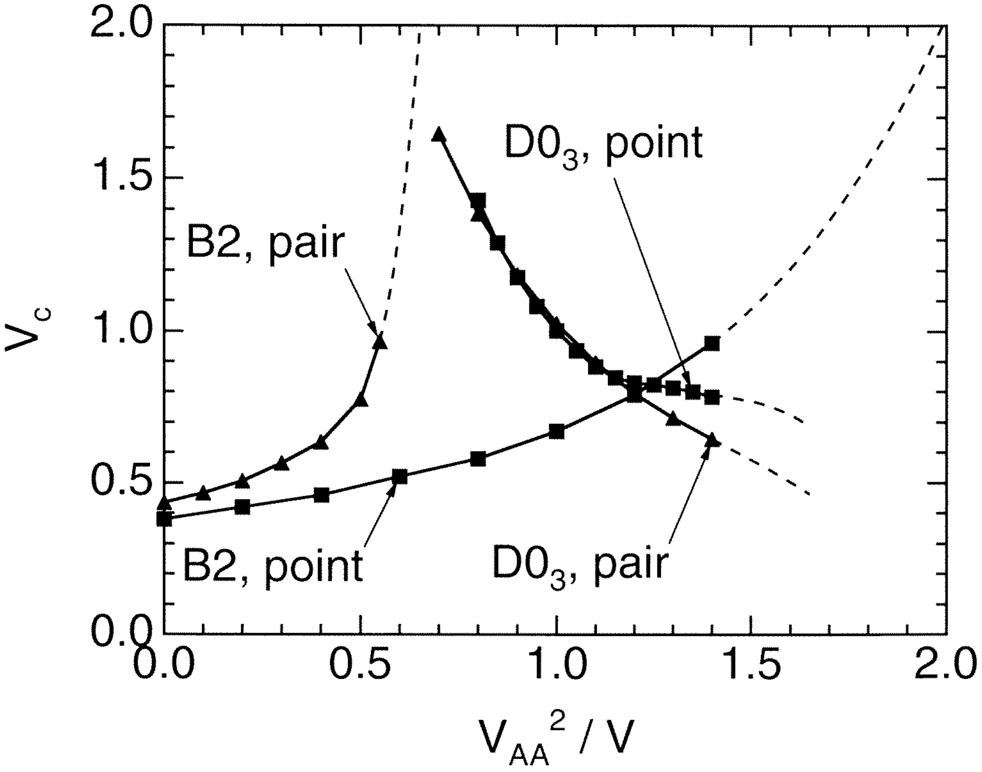

Figure 2.16: Critical potentials V_c^{B2} and $V_c^{\mathrm{D0_3}}$ at the AB$_3$ stoichiometry as a function of V_{AA}^2/V, where $V \equiv V_{\mathrm{AA}}^1 = V_{\mathrm{BB}}^1$, for two different kinetic models: a. point approximation and b. pair approximation.

values of V, and tested for the occurrence of incipient B2 and D0$_3$ ordering. Also included in Fig. 2.16 are the corresponding critical potential curves from our earlier work with the MEM in the point approximation (see Fig. 2.8). Both sets of critical potentials display similar general trends. The ordinate intercepts of the V_c^{B2} curves correspond to the B2 critical potentials for the familiar case of 1nn interactions only. These B2 critical potentials agree with corresponding critical potentials obtained from equilibrium theory. As the 2nn interactions are turned on (increasing V_{AA}^2/V), the V_c^{B2} curves increase and the $V_c^{\mathrm{D0_3}}$ curves decrease. This is the expected behavior since the positive 2nn interactions (V^2) tend to suppress B2 ordering and enhance D0$_3$ ordering.

The same interatomic interactions that determine the thermodynamic critical potentials also set the Boltzmann factors in the kinetic rate equations. Although the rate equations depend also on the number of available paths between the various state variables, the kinetic rate equations can be dominated by the interatomic potentials when the ratio of V^2/V^1 is near zero or infinity and $V^1, V^2 > 0$. In these extreme cases of all 1nn (or all 2nn) interactions, there is no possibility for the evolution of D0$_3$ (or B2) order. The thermodynamic equilibrium states of B2 (or D0$_3$) order are forced to evolve, and there is little of interest in the kinetic path through the parameter space of B2 and D0$_3$ order. We expect that for kinetic tendencies to produce thermodynamically nonintuitive behavior, the best choices of V^2/V^1 will be near the intersections of the V_c^{B2} and $V_c^{\mathrm{D0_3}}$ critical potential curves in Fig. 2.16.[6] It is in the neighborhood of these intersections, where the critical

---

[6] We were unable to determine the intersection point of the V_c^{B2} and $V_c^{\mathrm{D0_3}}$ critical potential curves for the case of the pair approximation. These critical potential curves rose sharply in the neighborhood of the presumed intersection of these curves and the integration of the resulting differential equations became prohibitively slow. This steep rise in the critical potential curves may be an artifact of the fact that the pair approximation used only the 1nn pair as the base cluster, but used both 1nn as well as 2nn pair interaction potentials.

potentials for B2 and $D0_3$ are of comparable magnitude, that we would expect to see strong temperature-dependence of the kinetic paths. This is because the thermodynamic driving forces for B2 and $D0_3$ ordering are approximately equal for values of V_{AA}^2/V corresponding to these intersections. It is then possible for the kinetic path to be influenced strongly by kinetic factors such as the number of paths between state variables. This conjecture was borne out in our earlier work in the point approximation, where the strong variations in kinetic paths depicted in Fig. 2.7 were obtained for $V_{\mathrm{AA}}^2/V = 1.25$, which is near the intersection of the B2 and $D0_3$ critical potential curves for the point approximation (see Fig. 2.16).

We used temperature to control the shapes of kinetic paths, such as those in Fig. 2.7. Figure 2.17 shows kinetic paths in $(S_{\mathrm{D0_3}}, S_{\mathrm{B2}})$-space for $V_{\mathrm{AA}}^1 = V_{\mathrm{BB}}^1 \equiv V, V_{\mathrm{AA}}^2/V = 0.75$ in the pair approximation for three different values of V ($V = 1.60$, $V = 1.80$, and $V = 2.00$). The kinetic paths began at near-complete disorder in the lower left corner $[(S_{\mathrm{D0_3}}, S_{\mathrm{B2}}) = (0,0)]$ and evolved toward equilibrium order near the upper right corner $[(S_{\mathrm{D0_3}}, S_{\mathrm{B2}}) = (1,1)]$. The kinetic paths for the cases $V = 1.80$ and $V = 2.00$ showed a distinct two-stage ordering process. Such a two-stage ordering process was absent for the case of $V = 1.60$. For the cases $V = 1.80$ and $V = 2.00$, a significant amount of $D0_3$ order had evolved before the B2 order parameter began to increase. We attribute this rapid relaxation of $D0_3$ order to the stronger driving force for $D0_3$ ordering relative to B2 ordering at this particular value of V_{AA}^2/V. The degree of $D0_3$ order obtained before significant B2 order began to develop varied inversely with annealing temperature. In other words, the two-stage nature of the evolution of order in the alloy was accentuated by lowering the annealing temperature. This heightening of the two-stage ordering process with decreasing temperature had been observed earlier in our work using the MEM in the point approximation [14] and in our experimental work on B2 and

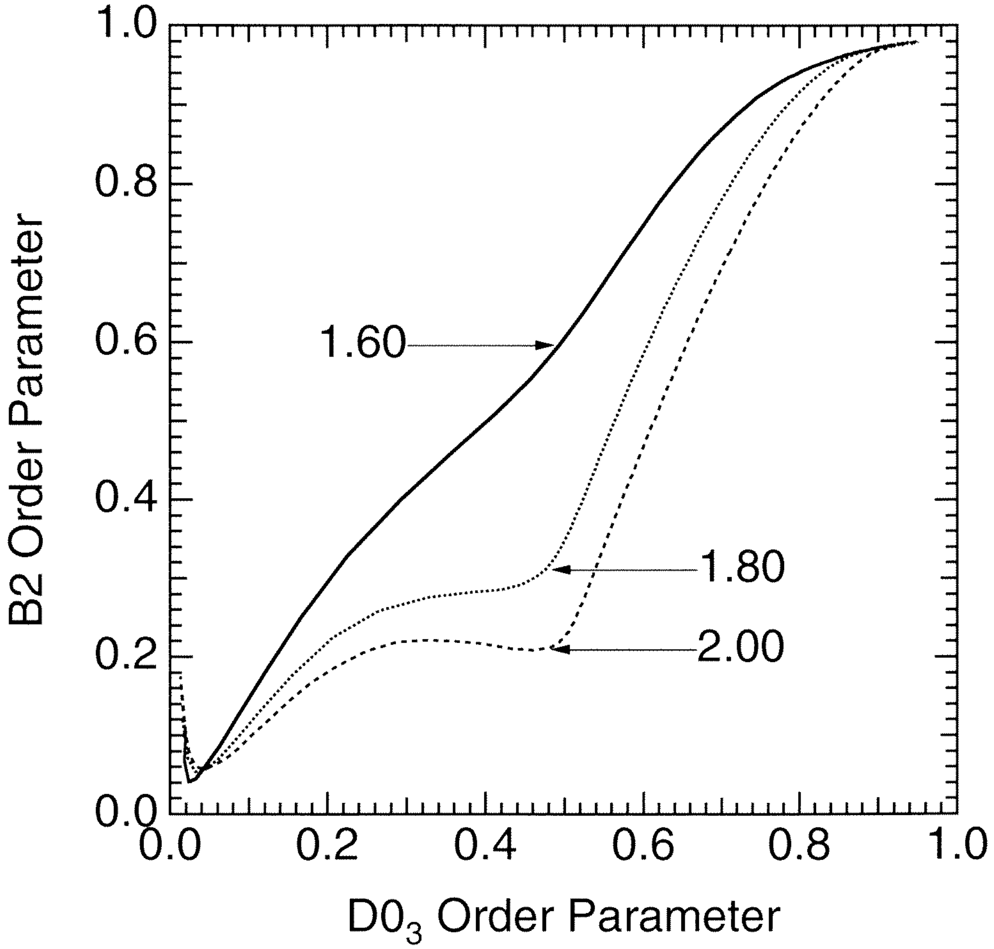

Figure 2.17: Kinetic paths depicting the temperature-dependence of order evolution in $(S_{\mathrm{D0_3}}, S_{\mathrm{B2}})$-space at the $\mathrm{AB_3}$ stoichiometry. Curves were obtained using the pair approximation. Labels indicate values of V, where $V \equiv V^1_{\mathrm{AA}} = V^1_{\mathrm{BB}} = \frac{4}{3}V^2_{\mathrm{AA}}$ $(V^2_{\mathrm{AA}}/V = 0.75)$.

$D0_3$ ordering in Fe_3Al [9]. This characteristic is a general feature of temperature-dependent kinetic paths, caused by the larger range in Boltzmann factors at lower temperatures. (The paths between state variables are of course independent of temperature.)

Transient B32 and B2 order

We attempted to reproduce the formation of transient B32 order using the pair approximation with the same set of interaction potentials used previously in the MEM in the point approximation ($V^1_{\mathrm{AA}} = V^2_{\mathrm{AA}} = 1.60$) [14]. Figure 2.18 shows the result, which includes a transient appearance of B32 order. This figure is qualitatively similar to Fig. 6 of Ref. [14], but in the present case, the transient B32 state is not as persistent. As in the case of the point approximation, the details of the transient behavior were found to be sensitive to the choice of initial conditions of the alloy.

The transient appearance of B32 order can be argued consistently by the theory of spinodal ordering, which is based on the sensitivity of a free energy to static chemical concentration waves [20,21]. The AB_3 alloy of Fig. 2.18 is unstable against the $\langle\frac{1}{2}\frac{1}{2}\frac{1}{2}\rangle$ concentration wave, which would normally produce B32 order in equilibrium. However, the AB_3 stoichiometry cannot support the B32 structure. As the intensity of the $\langle\frac{1}{2}\frac{1}{2}\frac{1}{2}\rangle$ concentration wave grows, the free energy difference between the disordered state and that of the alloy increases as well. It is no longer sufficient to consider only the quadratic term in the free energy expression—the higher order terms in Eq. 5 of Ref. [21] will become significant when the alloy is partially ordered. In particular, the cubic term in the free energy expression would lead to a mixing of two different $\langle\frac{1}{2}\frac{1}{2}\frac{1}{2}\rangle$ concentration waves, giving rise to a $\langle 111\rangle$ concentration wave. On a bcc lattice, the $\langle 111\rangle$ concentration wave

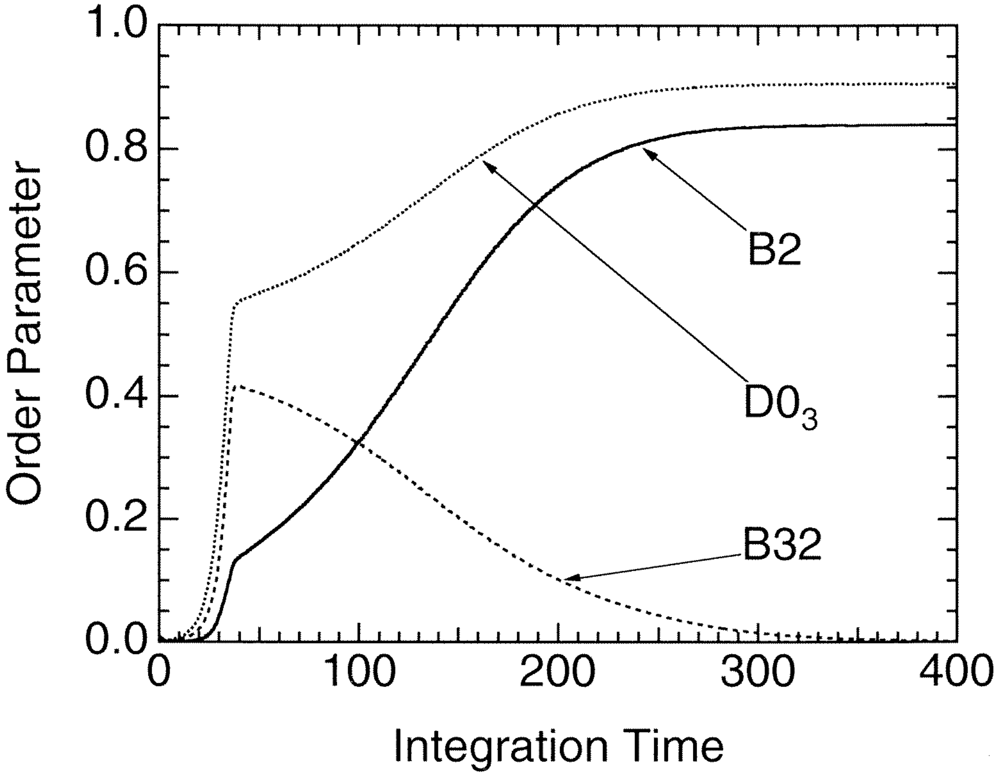

Figure 2.18: Time dependence of B2, D0$_3$, and B32 order parameters obtained using the pair approximation at the AB$_3$ stoichiometry ($V^1_{\text{AA}} = V^2_{\text{AA}} = 1.60$).

is equivalent to a $\langle 100 \rangle$ concentration wave. The combination of the $\langle \frac{1}{2}\frac{1}{2}\frac{1}{2} \rangle$ and $\langle 100 \rangle$ concentration waves will provide the growth of $D0_3$ order. While the theory of spinodal ordering is consistent with our present observations of transient B32 order at the AB_3 stoichiometry, we will find in the next chapter, an example of transient order at the AB stoichiometry which cannot be explained by spinodal ordering.

2.2.4 Conclusions

We have developed a theory of ordering kinetics with vacancies in the pair approximation using the superposition approximation with chained probabilities for alloys with equilibrium states of B2, $D0_3$, or B32 order. By varying the interatomic pair potentials and the annealing temperature, a rich variety of kinetic paths through order parameter space was obtained. These kinetic paths were qualitatively similar to those obtained previously using a point approximation. Significant variations of kinetic paths were obtained when the critical temperatures for B2 and $D0_3$ ordering were not strongly different. In these cases the annealing temperature can be used as a means of controlling kinetically the formation of a wide variety of nonequilibrium states of order. We were also able to reproduce the previously-reported transient B32 order in alloys with AB_3 stoichiometry using both the path probability method in the pair approximation.

References

[1] H. Sato and R. Kikuchi, *Acta Metall.* **24**, 797 (1976).

[2] H. Sato, K. Gschwend, and R. Kikuchi, *J. de Physique* **C7**, 357 (1977).

[3] Y. Saito and R. Kubo, *J. Stat. Phys.* **15**, 233 (1976).

[4] S. Radelaar, *J. Phys. Chem. Solids* **31**, 219 (1970).

[5] D. de Fontaine, *J. Phys. Chem. Solids* **34**, 1285 (1973).

[6] M. Murakami, D. de Fontaine, J. M. Sanchez and J. Fodor, *Acta Metall.* **22**, 709 (1974).

[7] B. Fultz, *Acta Metall.* **37**, 823 (1989).

[8] B. Fultz, H. H. Hamdeh, and D. H. Pearson, *Acta Metall.* **37**, 2841 (1989).

[9] L. Anthony and B. Fultz, *J. Mater. Res.* **4**, 1140 (1989).

[10] W. H. Press, B. P. Flannery, S. A. Teukolsky and W. T. Vetterling, *Numerical Recipes: The Art of Scientific Computing*, Cambridge University Press, Cambridge, (1986).

[11] C. W. Gear, *Numerical Initial Value Problems in Ordinary Differential Equations*, Prentice-Hall, Englewood Cliffs, (1971).

[12] M. J. Richards and J. W. Cahn, *Acta Metall.* **19**, 1263 (1971).

[13] S. M. Allen and J. W. Cahn, *Acta Metall.* **20**, 423 (1972).

[14] L. Anthony and B. Fultz, *J. Mater. Res.* **4**, 1132 (1989).

[15] Z. Q. Gao and B. Fultz, "Transient B32-like order during the early stages of ordering in undercooled Fe_3Al," *Philos. Mag. B*, in press.

[16] B. Fultz, *Philos. Mag. B* **67**, 253 (1993).

[17] R. Kikuchi, *Ann. Phys.* **10**, 127 (1960).

[18] R. Kikuchi, *Prog. Theor. Phys. Suppl.* **35**, 1 (1966).

[19] K. Gschwend, H. Sato, and R. Kikuchi, *J. Chem. Phys.* **69**, 5006 (1978).

[20] A. G. Khachaturyan, *Phys. Status Solidi B* **60**, 9 (1973).

[21] D. de Fontaine, *Acta Metall.* **23**, 553 (1975).

Chapter 3

Monte Carlo Simulations of Disorder→Order Transformations

In this chapter, I present the results of my investigations into the kinetics of disorder→order transformations in binary bcc alloys using Monte Carlo simulations. The method was used to study the development of short- and long-range order in alloys with equilibrium states of B2, $D0_3$, or B32 order. The Monte Carlo method was implemented on a simulated crystal lattice containing up to approximately half a million atoms and employed a vacancy mechanism for atom movement. Both first- (1nn) and second-nearest neighbor (2nn) pair interactions were considered. The results of the Monte Carlo simulations were compared with the results that were obtained using two different analytical techniques in Chapter 2. For all three calculations (point, pair, and Monte Carlo), critical temperatures for B2 and $D0_3$ ordering are reported for different 1nn and 2nn interaction strengths. The influence of annealing temperature on the kinetic paths through the space of B2, $D0_3$, and B32 order parameters was found to be strong when the thermodynamic preferences of the alloy were not too great. Transient states of intermediate order were also studied. A transient formation of B32 order in an AB_3 alloy was found when 2nn interactions were strong, even when B32 order was neither a Richards-Allen-Cahn ground state nor a stable equilibrium state at that temperature. The formation of this transient B32 order can be argued consistently from a thermodynamic perspective. However, a second example of transient B2 order in an AB alloy with equilibrium B32 order cannot be explained by the same thermodynamic argument, and we believe that its origin is primarily kinetic.

3.1 Introduction

In the previous chapter, we developed and implemented a kinetic theory of B2 and $D0_3$ ordering using a master equation method (MEM) in the point (Bragg-Williams) approximation [1]. Those efforts were motivated by our experimental work on ordering kinetics in Fe_3Al [2]. We also formulated an alternate theory of ordering in bcc alloys using the pair (Bethe) approximation and the 4-sublattice model of the previous theory. In addition to the increased accuracy obtained by using a larger base cluster, *viz.*, the pair instead of the point, the new theory also provided short-range order (SRO) parameters. It was instructive to identify the qualitative similarities of the long-range order (LRO) kinetics in the point and pair approximations by comparing their predicted "kinetic paths" for the alloy. In this chapter, we test further the reliability of those computations by performing Monte Carlo simulations (MCS) of ordering [3–7]. These MCS employ a single vacancy and the same mechanism of atom movement as the analytical theories, but are essentially exact for the large crystal lattices (containing up to half a million atoms) used in the present work.

One of the more surprising results from our work using the MEM in the point approximation [1] was the observation of transient B32 order that occurred for certain choices of the interaction potentials, particularly ones where the 2nn interactions were quite strong relative to the 1nn interactions, but both favored the formation of unlike pairs. Under these conditions, B32 order was neither a Richards-Allen-Cahn ground state [8,9] nor a stable equilibrium state at that temperature. Surprisingly, however, B32 order appeared transiently during the disorder→order transformation. This transient B32 order was not metastable in that it did not correspond to a local minimum in the free energy surface. One of the members of our group has obtained experimental evidence for the formation of such a pseudostable B32 state during low-temperature annealings of disordered Fe_3Al [10]. Recent theoretical investigations have suggested that such transient or *pseudostable* states may correspond to saddle points in the free energy surface [11]. In the course of calculating kinetic paths of ordering, we found examples of transient states of order that are nonintuitive from thermodynamic arguments. We made some effort to optimize the appearance of these transient states, and we discuss them here.

3.2 Theory

The algorithm for our MCS is identical to that used in our earlier studies of vacancy diffusion and ordering, and is described in detail elsewhere [3–7]. In brief, we employed a bcc lattice of $32 \times 32 \times 32 \times 2 = 65536$ atoms for most of this work, although we performed some work with larger lattices. Initially the lattice was randomly populated with A and B atoms in a $1 : 3$ ratio for the AB_3 stoichiometry (or $1 : 1$ for the AB stoichiometry) except for one of the sites which was left vacant. This solitary vacancy was the agent for the atom movements that produced ordering. Prior to each vacancy jump, the bond energies for the eight first-nearest neighbor (1nn) atoms surrounding the vacancy were computed, together with the corresponding Boltzmann factors. This Boltzmann factor was of the form

$$\exp\left[N^1_{\mathrm{AA}}V^1_{\mathrm{AA}} + N^1_{\mathrm{BB}}V^1_{\mathrm{BB}} + N^1_{\mathrm{AB}}V^1_{\mathrm{AB}} + N^2_{\mathrm{AA}}V^2_{\mathrm{AA}} + N^2_{\mathrm{BB}}V^2_{\mathrm{BB}} + N^2_{\mathrm{AB}}V^2_{\mathrm{AB}}\right], \quad (3.1)$$

where, for instance, N^1_{AA} is the number of 1nn A–A bonds, and V^1_{AA} their energy in units of k_BT. It was necessary to consider second-nearest neighbor (2nn) as well as 1nn bond strengths since D0$_3$ order cannot develop with 1nn interactions alone. Competition among the eight 1nn atoms for the vacant site was resolved probabilisticaqlly with the outcome weighted by the respective Boltzmann factors.

Periodically during the MCS runs, information on the SRO and LRO was extracted from the simulated lattice. The Warren-Cowley SRO parameters were obtained by counting the numbers of A–A, B–B, and A–B pairs for various coordination shells. The LRO parameters were obtained by simulating the diffraction pattern of the lattice. Besides its similarity to experimental observations, this method had the added advantage of not being adversely affected by the domain structure [12]. (The domain structure in our MCS alloys impeded quantification of LRO by overlaying the ordered structure on the lattice.) To determine the kinematical diffraction intensities from our MCS lattice, we performed the following sum of phase factors

$$I(\Delta\mathbf{k}) = \left|\sum_{\mathbf{r}_{\mathrm{A}}} \exp[i\Delta\mathbf{k}\cdot\mathbf{r}_{\mathrm{A}}]\right|^2, \quad (3.2)$$

where the summation is performed over the positions of the A-atoms, $\mathbf{r}_{\mathrm{A}}$, for a cubic volume of edge length $\frac{1}{8}\frac{2\pi}{a_{\mathrm{bcc}}}$ around the $\frac{1}{2}\frac{1}{2}\frac{1}{2}$, 100, and 110 points in $\Delta\mathbf{k}$-space. These superlattice and fundamental diffraction intensities were monitored during the MCS runs, and were converted into B2, D0$_3$, and B32 LRO parameters as follows. We used the square root of the $(\frac{1}{2}\frac{1}{2}\frac{1}{2})$ and (100) superlattice intensities, normalized by the intensity of the (110) fundamental, and corrected for multiplicity. The conventional B2, D0$_3$, and B32 LRO parameters for the AB$_3$ (1 : 3) stoichiometry were then obtained as:

$$S_{\mathrm{D0_3}}^{25\%} = \left[\frac{\mathrm{Min}(I_{\frac{1}{2}\frac{1}{2}\frac{1}{2}}, I_{100})}{I_{110}}\right]^{\frac{1}{2}}, \tag{3.3}$$

$$S_{\mathrm{B2}}^{25\%} = \left[\frac{I_{100}}{I_{110}}\right]^{\frac{1}{2}} - S_{\mathrm{D0_3}}^{25\%}, \tag{3.4}$$

$$S_{\mathrm{B32}}^{25\%} = \left[\frac{I_{\frac{1}{2}\frac{1}{2}\frac{1}{2}}}{I_{110}}\right]^{\frac{1}{2}} - S_{\mathrm{D0_3}}^{25\%}, \tag{3.5}$$

where $0 \leq S_{\mathrm{D0_3}}^{25\%}, S_{\mathrm{B2}}^{25\%}, S_{\mathrm{B32}}^{25\%} \leq 1$. For the AB (1 : 1) stoichiometry, the conventional B2 and B32 LRO parameters were given by:[1]

$$S_{\mathrm{B2}}^{50\%} = \left[\frac{I_{100}}{I_{110}}\right]^{\frac{1}{2}}, \tag{3.6}$$

$$S_{\mathrm{B32}}^{50\%} = \left[\frac{2I_{\frac{1}{2}\frac{1}{2}\frac{1}{2}}}{I_{110}}\right]^{\frac{1}{2}}, \tag{3.7}$$

where $0 \leq S_{\mathrm{B2}}^{50\%}, S_{\mathrm{B32}}^{50\%} \leq 1$.

3.3 Results and Discussion

3.3.1 Kinetic and Thermodynamic Trends

The steady state of any viable kinetic theory of ordering and disordering should be the appropriate state of thermodynamic equilibrium. In particular, the kinetic theory in the pair approximation should be consistent with the cluster variation method (CVM) in the pair approximation and the MCS critical potentials should provide essentially exact results (making allowance for finite-size effects). This is what we found when we calculated the critical temperatures for B2 and D0$_3$ LRO by these two methods. Figure 3.1 shows the critical potentials for B2 and D0$_3$ order as a function of V_{AA}^2/V. These curves were obtained by considering alloys

---

[1] Since the AB (1 : 1) stoichiometry is not conducive to the formation of D0$_3$ order, we are able to identify the $(\frac{1}{2}\frac{1}{2}\frac{1}{2})$ peak with the presence of B32 order and the (100) peak with the presence of B2 order without any ambiguity.

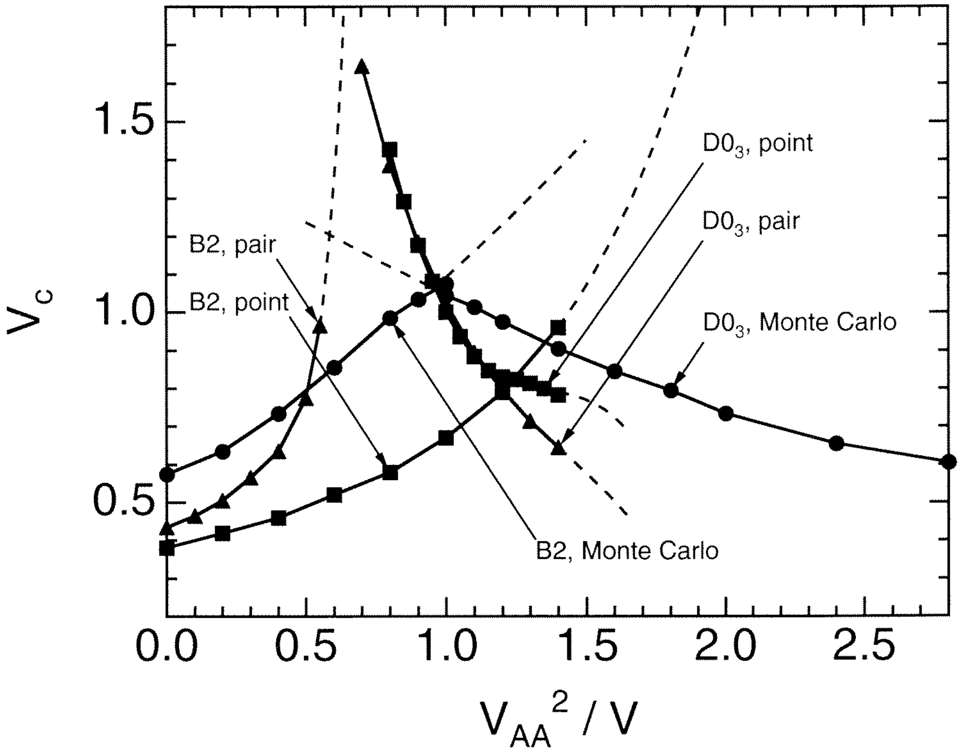

Figure 3.1: Critical potentials V_c^{B2} and $V_c^{\mathrm{D0_3}}$ at the AB$_3$ stoichiometry as a function of V_{AA}^2/V, where $V \equiv V_{\mathrm{AA}}^1 = V_{\mathrm{BB}}^1$, for three different kinetic models: a. point approximation, b. pair approximation, and c. Monte Carlo simulation.

which had $V^1_{\mathrm{AA}} = V^1_{\mathrm{BB}} \equiv V$ and V^2_{AA} as the only nonzero pair potentials, varying V for a fixed ratio of V^2_{AA}/V. This is equivalent to maintaining the same interatomic potentials and varying the temperature. We tried a range of different values of V, and tested for the occurrence of incipient B2 and $\mathrm{D0_3}$ ordering. Also included in Fig. 3.1 are the corresponding critical potential curves from our earlier work with the MEM in the point approximation (see Fig. 5a of Ref. [1]). All three sets of critical potentials display similar general trends. The ordinate intercepts of the V_c^{B2} curves correspond to the B2 critical potentials for the familiar case of 1nn interactions only. These B2 critical potentials agree with corresponding critical potentials obtained from equilibrium theory. As the 2nn interactions are turned on (increasing V^2_{AA}/V), the V_c^{B2} curves increase and the $V_c^{\mathrm{D0_3}}$ curves decrease. This is the expected behavior since the positive 2nn interactions (V^2) tend to suppress B2 ordering and enhance $\mathrm{D0_3}$ ordering.

The same interatomic interactions that determine the thermodynamic critical potentials also set the Boltzmann factors in the kinetic rate equations. Although the rate equations depend also on the number of available paths between the various state variables, the kinetic rate equations can be dominated by the interatomic potentials when the ratio of V^2/V^1 is near zero or infinity and $V^1, V^2 > 0$. In these extreme cases of all 1nn (or all 2nn) interactions, there is no possibility for the evolution of $\mathrm{D0_3}$ (or B2) order. The thermodynamic equilibrium states of B2 (or $\mathrm{D0_3}$) order are forced to evolve, and there is little of interest in the kinetic path through the parameter space of B2 and $\mathrm{D0_3}$ order. We expect that for kinetic tendencies to produce thermodynamically nonintuitive behavior, the best choices of V^2/V^1 will be near the intersections of the V_c^{B2} and $V_c^{\mathrm{D0_3}}$ critical potential curves in Fig. 3.1. It is in the neighborhood of these intersections, where the critical potentials for B2 and $\mathrm{D0_3}$ are of comparable magnitude, that we would expect to see strong temperature-dependence of the kinetic paths. This is because the thermodynamic driving forces for B2 and $D0_3$ ordering are approximately equal for values of V^2_{AA}/V corresponding to these intersections. It is then possible for the kinetic path to be influenced strongly by kinetic factors such as the number of paths between state variables. This conjecture was borne out in our earlier work in the point approximation, where the strong variations in kinetic paths depicted in Fig. 4 of Ref. [1] were obtained for $V^2_{\mathrm{AA}}/V = 1.25$, which is near the intersection of the B2 and $D0_3$ critical potential curves for the point approximation (see Fig. 3.1).

3.3.2 Transient B32 and B2 order

We attempted to reproduce the formation of transient B32 order that had been obtained previously in Chapter 2 using both the master equation method in point approximation and the path probability method in the pair approximation. Figure 3.2 depicts the B2, $D0_3$, and B32 LRO parameters as a function of Monte Carlo step (analogous to a time axis). The interaction potentials used in obtaining this figure were $V^1_{\mathrm{AA}} = V^1_{\mathrm{BB}} = 1.00$ and $V^2_{\mathrm{AA}} = 2.00$. We observed that after about 200 Monte Carlo steps, a significant quantity of B32 order had developed, without much $D0_3$ order. However, as the simulated lattice continued to evolve toward equilibrium, the B32 LRO began to decrease while the $D0_3$ LRO continued to increase to its equilibrium value. The equilibrium condition consisted almost entirely of $D0_3$ order; the residual quantity of B32 LRO that seemed to persist at equilibrium can be attributed to the manner in which we have extracted our LRO parameters using Eqs. 3.3 – 3.5. The noticeable kink in the two LRO curves between 10 000 and 15 000 Monte Carlo steps is due to the annihilation of antiphase domain boundaries.

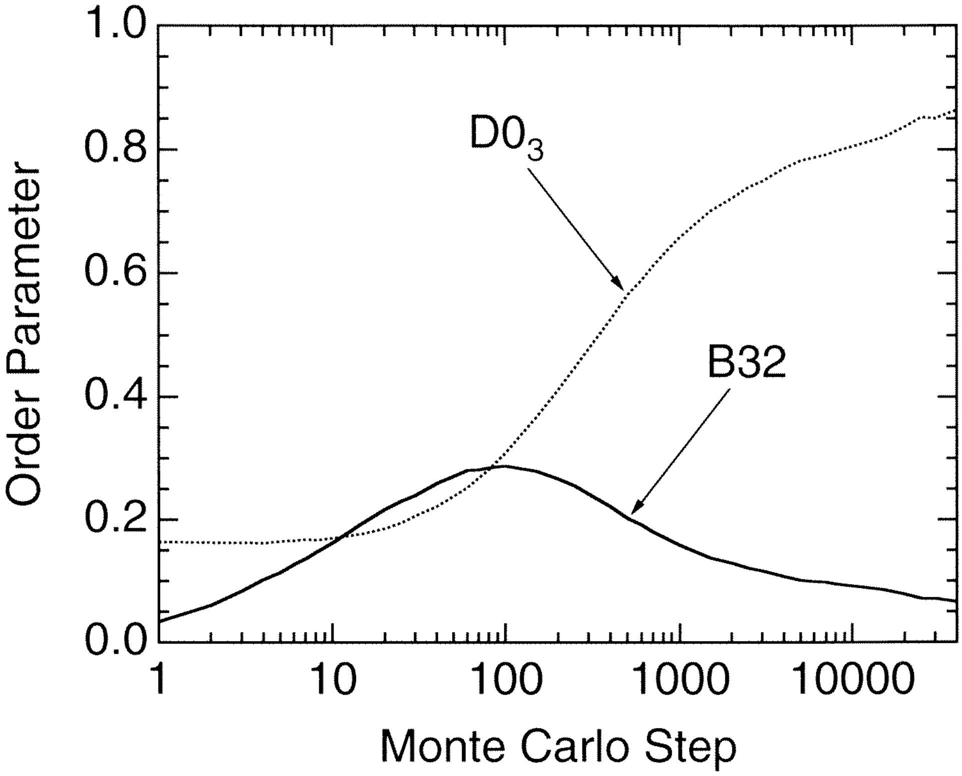

Figure 3.2: Time dependence of D0$_3$ and B32 order parameters obtained using Monte Carlo simulation at the AB$_3$ (1 : 3) stoichiometry ($V^1_{\mathrm{AA}} = V^1_{\mathrm{BB}} = 1.00$, $V^2_{\mathrm{AA}} = 2.00$). The curves were obtained from the integrated intensities of the ($\frac{1}{2}\frac{1}{2}\frac{1}{2}$) and (100) superlattice peaks and the (110) fundamental peak using Eqs. 3.3 – 3.5.

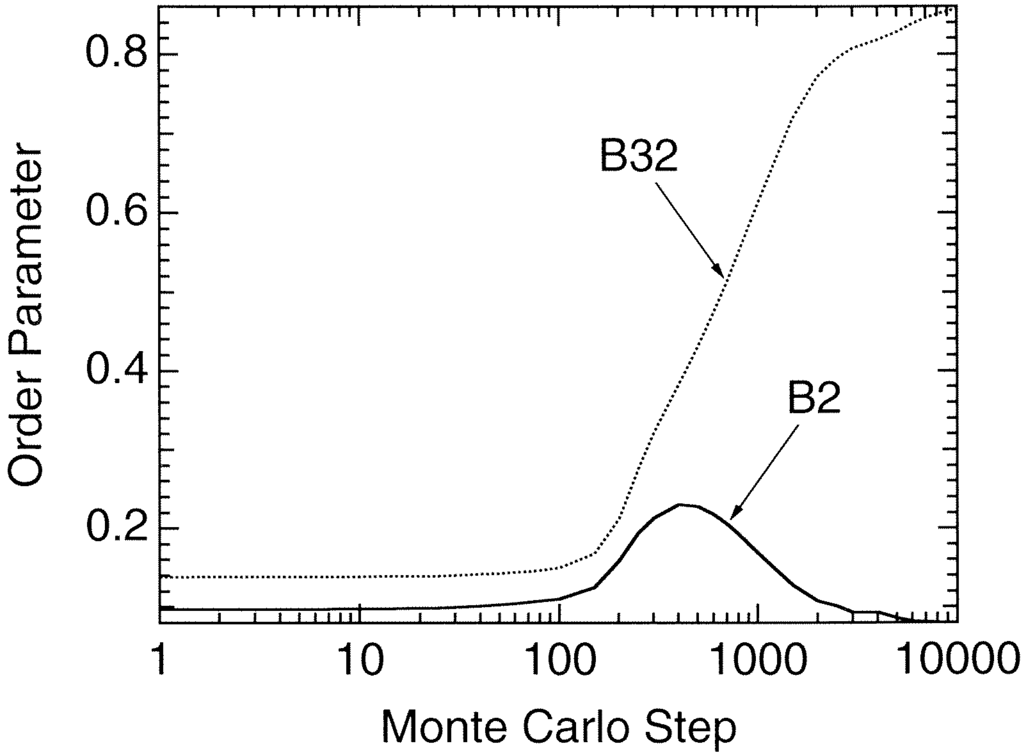

Figure 3.3: Time dependence of B2 and B32 order parameters obtained using Monte Carlo simulation at the AB (1 : 1) stoichiometry ($V^1_{\mathrm{AA}} = V^1_{\mathrm{BB}} = 1.00$, $V^2_{\mathrm{AA}} = 1.40$). The curves were obtained from the integrated intensities of the $(\frac{1}{2}\frac{1}{2}\frac{1}{2})$ and (100) superlattice peaks and the (110) fundamental peak using Eqs. 3.6 and 3.7.

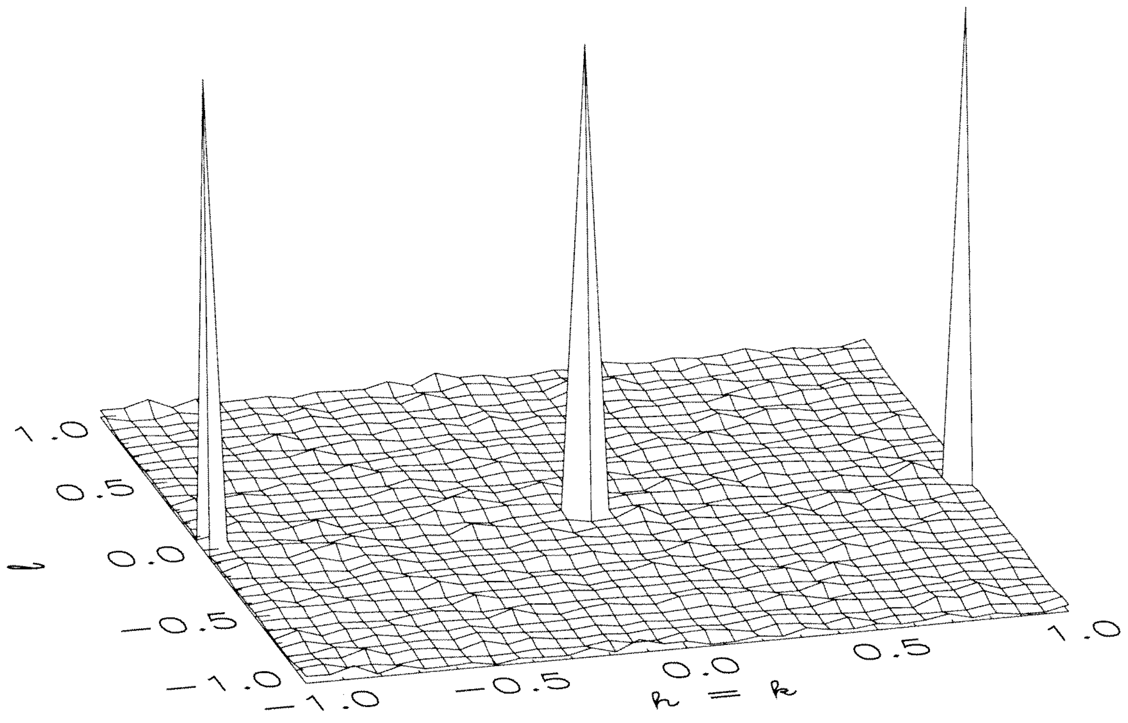

Figure 3.4: Surface plot of [110] zone axis diffraction pattern obtained from the Monte Carlo simulated lattice of Fig. 3.3 at 0 Monte Carlo steps.

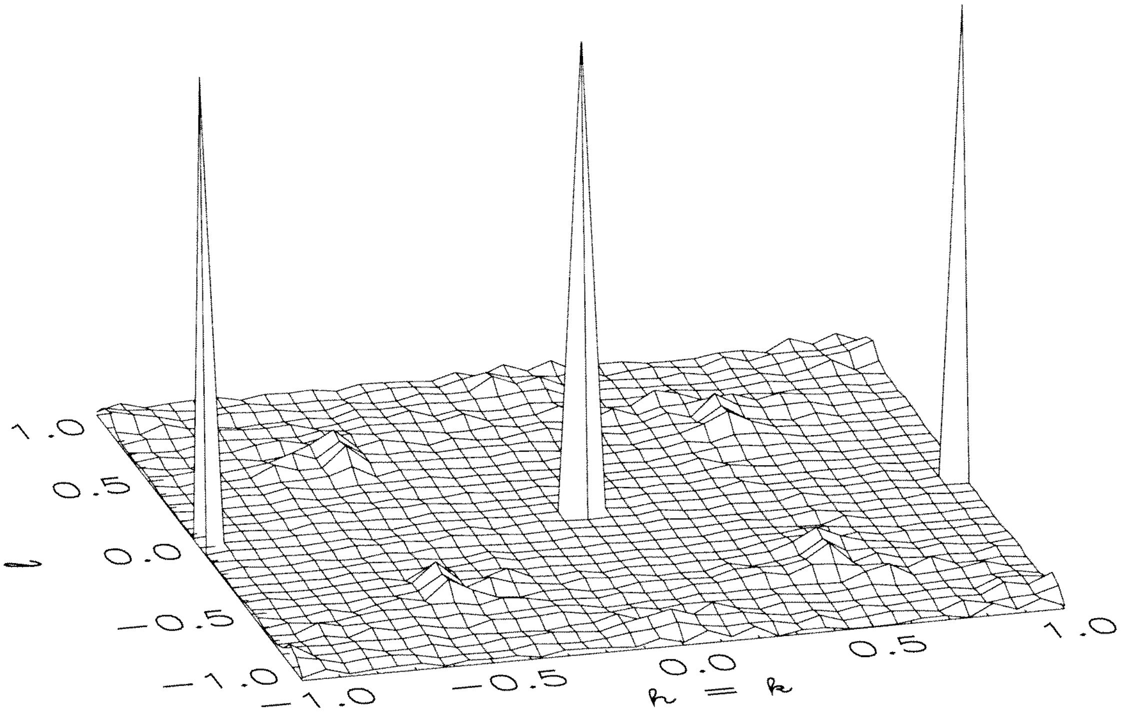

Figure 3.5: Surface plot of [110] zone axis diffraction pattern obtained from the Monte Carlo simulated lattice of Fig. 3.3 at 300 Monte Carlo steps.

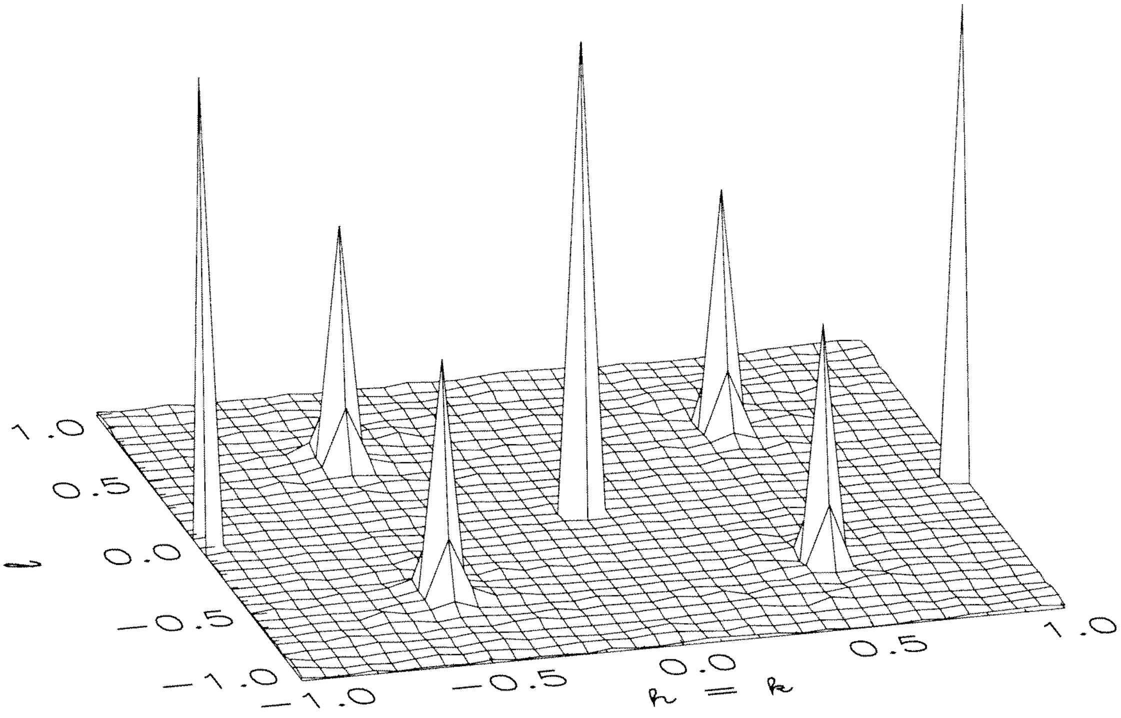

Figure 3.6: Surface plot of [110] zone axis diffraction pattern obtained from the Monte Carlo simulated lattice of Fig. 3.3 at 3000 Monte Carlo steps.

All of the results discussed thus far were obtained for the AB_3 (1 : 3) stoichiometry. We repeated the MCS discussed in the previous paragraph for the AB (1 : 1) stoichiometry and a slightly different choice of interaction potentials ($V^1_{\mathrm{AA}} = V^1_{\mathrm{BB}} = 1.00$, $V^2_{\mathrm{AA}} = 1.40$). Figure 3.3 depicts the corresponding variation of the B2 and B32 LRO parameters with Monte Carlo step. Here, the equilibrium state exhibits a strong $(\frac{1}{2}\frac{1}{2}\frac{1}{2})$ peak with negligible intensity in the (100) superlattice peak. This is indicative of equilibrium B32 order. However, the appearance of a transient (100) superlattice peak after about 300 Monte Carlo steps indicates transient B2 order. This can be clearly seen in Figs. 3.4 – 3.6 which shows surface plots of the [110] zone axis diffraction pattern obtained from the simulated lattice after 0, 300, and 3000 Monte Carlo steps. Compared with the previous behavior at the AB_3 stoichiometry, we have gone from a condition of equilibrium $D0_3$ order with transient B32 order to one of equilibrium B32 order with transient B2 order. By altering the stoichiometry of the alloy and its interaction potentials, we were able to alter not only its equilibrium state but also its transient microstructure. We also examined the simulated AB lattice at 300 Monte Carlo steps, and found that it consisted of small well-defined domains of B2 and B32 order of a few lattice constants in diameter.

The transient appearance of B32 order can be argued consistently by the theory of spinodal ordering, which is based on the sensitivity of a free energy to static chemical concentration waves [13,14]. The AB_3 alloy of Fig. 3.2 is initially unstable against the $\langle\frac{1}{2}\frac{1}{2}\frac{1}{2}\rangle$ concentration wave, which would normally produce B32 order in equilibrium. However, the AB_3 stoichiometry cannot support the B32 structure. As the intensity of the $\langle\frac{1}{2}\frac{1}{2}\frac{1}{2}\rangle$ concentration wave grows, the free energy difference between the disordered state and that of the alloy increases as well. It is no longer sufficient to consider only the quadratic term in the free energy expression—

Ref. [14] will become significant when the alloy is partially ordered. In particular, the cubic term in the free energy expression would lead to a mixing of two different $\langle\frac{1}{2}\frac{1}{2}\frac{1}{2}\rangle$ concentration waves, giving rise to a $\langle 111\rangle$ concentration wave. On a bcc lattice, the $\langle 111\rangle$ concentration wave is equivalent to a $\langle 100\rangle$ concentration wave. The combination of the $\langle\frac{1}{2}\frac{1}{2}\frac{1}{2}\rangle$ and $\langle 100\rangle$ concentration waves will provide the growth of $D0_3$ order.

While the theory of spinodal ordering is consistent with our observations for the AB_3 stoichiometry, it cannot explain the transient formation of B2 order at the AB stoichiometry. It is impossible to mix two $\langle 100\rangle$ concentration waves to create a $\langle\frac{1}{2}\frac{1}{2}\frac{1}{2}\rangle$ concentration wave. Spinodal ordering is a thermodynamic idea without any features that are uniquely kinetic, *e.g.*, paths between state variables. Although spinodal ordering may be a useful concept for alloys near thermodynamic equilibrium, it is not generally applicable to kinetic phenomena in alloys far from thermodynamic equilibrium.

3.4 Conclusions

We have used Monte Carlo simulations to study the ordering kinetics of alloys with equilibrium states of B2, $D0_3$, or B32 order. By varying the interatomic pair potentials and the annealing temperature, a rich variety of kinetic paths through order parameter space was obtained. These kinetic paths were qualitatively similar to those obtained in the previous chapter using the point and pair approximations. Significant variations of kinetic paths were obtained when the critical temperatures for B2 and $D0_3$ ordering were not strongly different. In these cases the annealing temperature can be used as a means of controlling kinetically the formation of a wide variety of nonequilibrium states of order.

We were also able to reproduce the previously-reported transient B32 order in

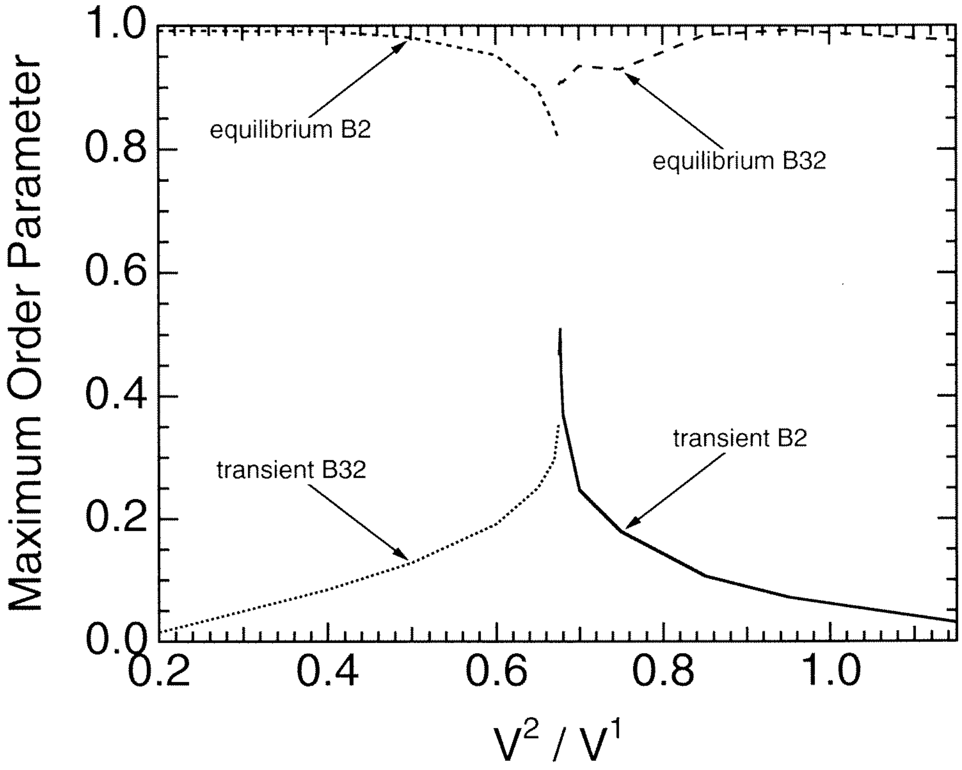

Figure 3.7: Maximum quantity of transient and equilibrium order as a function of $\frac{V^2}{V^1}$ obtained using Monte Carlo simulations at the AB (1 : 1) stoichiometry ($V^1_{\mathrm{AA}} = V^1_{\mathrm{BB}} = 1.00$, V^2_{AA} variable). The curves were obtained from the integrated intensities of the $(\frac{1}{2}\frac{1}{2}\frac{1}{2})$ and (100) superlattice peaks and the (110) fundamental peak using Eqs. 3.6 and 3.7.

alloys with AB_3 stoichiometry using Monte Carlo simulations. For another alloy with AB stoichiometry we were able to obtain transient B2 order with $D0_3$ order as the equilibrium state. The transient microstructure was an admixture of B2 and B32 ordered domains of a few lattice constants in diameter. It is not possible to account for the formation of these transient kinetic states using conventional thermodynamic arguments.

References

[1] L. Anthony and B. Fultz, J. Mater. Res. **4**, 1132 (1989).

[2] L. Anthony and B. Fultz, J. Mater. Res. **4**, 1140 (1989).

[3] B. Fultz, J. Chem. Phys. **87**, 1604 (1987).

[4] B. Fultz, J. Chem. Phys. **88**, 3227 (1988).

[5] B. Fultz and L. Anthony, in *Diffusion in High Technology Materials*, edited by D. Gupta, A. D. Romig, Jr., and M. A. Dayananda, (The Minerals, Metals and Materials Society, Warrendale, Pennsylvania, 1988).

[6] B. Fultz and L. Anthony, Philos. Mag. Lett. **59**, 237 (1989).

[7] H. Ouyang and B. Fultz, J. Appl. Phys. **66**, 4752 (1989).

[8] M. J. Richards and J. W. Cahn, Acta Metall. **19**, 1263 (1971).

[9] S. M. Allen and J. W. Cahn, Acta Metall. **20**, 423 (1972).

[10] Z. Q. Gao and B. Fultz, "Transient B32-like order during the early stages of ordering in undercooled Fe_3Al," *Philos. Mag. B*, in press.

[11] B. Fultz, *Philos. Mag. B* **67**, 253 (1993).

[12] B. E. Warren, *X-ray Diffraction*, (Addison-Wesley, Reading, Massachusetts, 1969), Sec. 12.3.

[13] A. G. Khachaturyan, Phys. Status Solidi B **60**, 9 (1973).

[14] D. de Fontaine, Acta Metall. **23**, 553 (1975).

Chapter 4

The Hybrid Monte Carlo–Cluster Variation Method

In the previous two chapters of this thesis, I presented two philosophically different approaches to the study of kinetic phenomena in general and order-disorder transformations in particular. In Chapter 2, I considered two analytical models (the master equation method and the path probability method) as used in the study of disorder→order kinetics in binary bcc alloys exhibiting B2, $D0_3$, and/or B32 order as possible ordered states. Chapter 3, in contrast, presented a more brute-force approach to alloy kinetics (the Monte Carlo method) as applied to various systems in two and three dimensions.

Each of these two approaches has its own particular merits and demerits. With the analytical techniques (cluster approximations), we are able to obtain closed-form albeit approximate expressions for the configurational entropy and the free energy. On the debit side, such mean-field approaches are inaccurate unless the clusters involved are fairly large. Unfortunately, any increase in the size of clusters considered is generally accompanied by increased complexity of the path probability expressions as well as the configurational entropy and free energy expressions.[1]

---

[1] There are notable exceptions to this rule. For instance, in the two-dimensional triangle and square lattices, there exist sequences of base clusters, sometimes called "ladder clusters," for

The resulting path probability expressions in the path probability method are difficult to maximize with respect to their constituent path variables. The same is in general true for minimizing the free energy expressions with respect to their constituent state variables in the corresponding cluster variation method. However, the situation is not as dire in the latter case since for a given base cluster set, the free energy expression is far less complicated than the corresponding path probability expression (there is no time dependence to be considered). Furthermore, it is possible to avoid the multivariable minimization of the free energy altogether by using a technique known as the natural iteration method [2]. The natural iteration method has been proved rigorously to converge to the minimum free energy and in practice does so quite rapidly [2].

The Monte Carlo simulations, on the other hand, face no such daunting proposition of having to deal with a multivariable maximization or minimization. If the critical temperature of ordering is to be used as a measure of the method's worth, Monte Carlo simulations are also quite accurate provided the lattice sizes are sufficiently large. In any event extending the method to larger crystal lattices is trivial compared to the effort required to extend the path probability method to larger base clusters. Monte Carlo simulations of vacancy ordering are also a reasonable model of the actual ordering process from a mechanistic viewpoint. The concepts of bond-breaking energies and activation barrier heights have a certain logical and intuitive appeal.

However, there is no simple method of obtaining the configurational entropy and free energy directly from the crystal lattice during a kinetic Monte Carlo simulation, such as those of the previous chapter. There do exist indirect tech-

---

which simple recursion relations can be written for the cluster configurational entropy. Using these, it is possible to obtain expressions for the cluster configurational entropy and free energy which contain relatively few terms, even when the base cluster is very large [1].

niques for calculating the configurational entropy and free energy but these have only been demonstrated for equilibrium Monte Carlo systems and in any event are computationally quite expensive [3].

In this chapter, I present a novel technique for calculating free energies of alloys during kinetic Monte Carlo simulations. We are particularly interested in the changes of the free energy during the evolution of chemical order. As mentioned previously, it has always been possible to keep track of the free energy in kinetic studies using the path probability method (PPM) [4,5]—the present method confers a similar capability upon kinetic Monte Carlo simulations. To calculate the free energy during a Monte Carlo simulation, we borrow ideas from the cluster variation method (CVM) [6,7]. In practice, the Monte Carlo simulations are carried out in the usual manner. In addition, however, the simulated crystal lattice is periodically sampled for the probabilities of various cluster types. These cluster probabilities are used directly in the CVM formulae for the configurational entropy and free energy. This simple but powerful idea combines synergistically the best of both worlds—the relationship between free energy and kinetics (such as provided by PPM) and the accuracy of Monte Carlo simulations. This method of obtaining the free energy of the Monte Carlo simulated lattice is also computationally cheap since it is only required to quantify the frequencies of occurrence of the various clusters—again no multivariable minimization of the free energy expression is required.

After this idea of using CVM entropy and free energy expressions in Monte Carlo simulations was developed and implemented, we were made aware of similar exploratory work by Schlijper [8,9] and others [10]. Schlijper *et al.* [8,9] demonstrated a CVM–Monte Carlo method for the estimation of free energies in the two- and three-dimensional three-state Potts model. In additon to the CVM entropy expressions, their method used an alternative Markovian estimate for the configurational entropy. Bichara *et al.* [10] then applied the CVM–Monte Carlo portion of Schlijper's technique to the study of Fe–Al alloys in the tetrahedron approximation. However, those efforts were directed at equilibrium systems. To the best of our knowledge, the present work is the first application of such hybrid CVM–Monte Carlo techniques to the study of nonequilibrium systems.

Before plunging headlong into the details of this hybrid CVM–Monte Carlo method, it will probably be useful to present a brief synopsis of the rest of the chapter. I will set the stage by briefly reviewing the original cluster variation method of Kikuchi [6,7]. In the process I will point out those aspects of the method that are of particular relevance to our needs. While on the subject of the cluster variation method, I will present a computer algorithm for the automatic generation of CVM free energy expressions for a specified set of base clusters. This algorithm makes use of ideas from an elegant reformulation of the cluster variation method using group theory [11]. The original cluster variation method is silent on the choice of base clusters to be used except for a vague notion that bigger is better. However, it is not always true that increasing the size of the base cluster improves the accuracy of the approximation. I will deliberate at some length on the various criteria and conventional choices for the cluster hierarchy and I will supplement these with some heuristic ideas of my own. With these preliminaries out of the way, I will enter into the description of the hybrid cluster variation–Monte Carlo method. Finally, I will conclude by presenting and discussing some representative results obtained with this method.

4.1 The Cluster Variation Method

The statistical mechanical basis of the CVM has been treated at great length in the many papers by Kikuchi and his coworkers [6,7]. Many workers have also attempted to clarify or reformulate its mathematical machinery [12–14,11,15,16]. The exposition of the cluster variation method in this chapter follows that of Refs. [14] and [11] but will be somewhat terse—the reader is referred to the above references for details. The essence of the cluster variation method can be summarized as follows: Given a specification of base (or maximal) cluster(s) of the parent crystal lattice (the choice of base cluster(s) essentially sets the degree of the approximation and the range of correlations to be considered), the CVM formalism provides an explicit albeit approximate expression for the configurational entropy and free energy of the system in terms of cluster probabilities of the base cluster(s) and its subclusters. In general, the equilibrium free energy is obtained by minimizing the free energy expression with respect to these cluster probabilities subject to one or more constraints, such as composition, long-range order (LRO), short-range order (SRO), etc. These constraints are typically incorporated through the use of Lagrange multipliers in the free energy expression. Such enterprises do not interest us here as we are only concerned with the free energy expression as a function of the various cluster probabilities—the Monte Carlo portion of the method will automatically take the necessary constraints into account.

Although the CVM was originally developed to deal with equilibrium structures, the CVM free energy expression remains a useful quantity in the consideration of nonequilibrium systems as well. In fact, in the PPM (the extension of the CVM to time-dependent processes), the (nonequilibrium) free energy is obtained as a by-product of maximizing the path probability. Some may question the applicability of the free energy concept to nonequilibrium systems in general and kinetic Monte Carlo simulations in particular. Consider the familiar expression for the Helmholtz free energy[2],

$$F = E - TS_{\mathrm{config}}, \tag{4.1}$$

as it applies to Monte Carlo kinetics. In the canonical Monte Carlo simulations employed here, the temperature T is always a well-defined quantity. In a pair interaction model, the internal energy E can, at any time, be obtained by simply examining all the atom pairs in the Monte Carlo crystal and summing their interaction energies. Whereas the configurational entropy S_{config} is proportional to the logarithm of, in principle, at least, a purely combinatorial term—one that is divorced from considerations of whether the system is in equilibrium. So we can conclude that both S_{config} and F are well-defined quantities in our Monte Carlo simulations. It remains, however, to demonstrate that they are useful for understanding the kinetic evolution of an alloy.

4.1.1 The Cluster Configurational Entropy

A cluster is simply a set, usually finite, of points in a crystal lattice, usually infinite. It can be specified uniquely by two variables, r and t, and is frequently denoted by the ordered pair (r, t). Here, r is an integer equal to the number of points in the cluster and t is a cardinal number used to distinguish between distinct clusters having the same number of points, r (r and t are positive integers). A cluster containing r points is also sometimes referred to as an r-point cluster [14]. Any two r-point clusters are considered equivalent if they are related to each other by the symmetry operations of the crystal lattice, *i.e.*, if at least one of the elements

---

[2] The present Monte Carlo simulations employ a rigid crystal lattice. Consequently, the Helmholtz and Gibbs free energies only differ by a fixed constant, PV.

of the space group of the lattice maps one of the r-point clusters onto the other. We will use this property later in our computer algorithm to determine if any two given r-point clusters are equivalent.

For a crystal lattice with p atomic species, there are p^r possible configurations of a particular (r,t) cluster if we allow each site of the (r,t) cluster to be independently occupied by one of the p atomic species. However, some of these p^r configurations may be indistinguishable from each other. Such equivalent configurations are related by an element of the point group of the (r,t) cluster. In general, then, the number of distinguishable (r,t) cluster configurations is given by the variable $s_{(r,t)}$, where $s_{(r,t)} \leq p^r$. We can therefore denote any given configuration of the (r,t) cluster by (r,t,l), where $1 \leq l \leq s_{(r,t)}$. The degeneracy of a given (r,t,l) configuration, $\alpha(r,t,l)$, is the number of distinguishable (r,t,l) configurations that are related by the point group of the (r,t) cluster. It follows, then, that

$$\sum_{l=1}^{s_{(r,t)}} \alpha(r,t,l) = p^r \tag{4.2}$$

for any given (r,t) cluster.

We can now write the configurational entropy density (the configurational entropy per lattice point or per atom) as

$$S = k_B \sum_{(r,t)} \gamma(r,t) \sum_{l=1}^{s_{(r,t)}} \alpha(r,t,l)\, x(r,t,l) \log\, x(r,t,l), \tag{4.3}$$

where k_B is Boltzmann's constant and $x(r,t,l)$ is the concentration of the (r,t) cluster in the l configuration with the normalization condition

$$\sum_{l=1}^{s_{(r,t)}} x(r,t,l) = 1. \tag{4.4}$$

In Eq. 4.3 above, the summation over (r,t) is carried out over the base cluster(s) and all subclusters of these base cluster(s). When (r,t) is one of the base clusters, the quantity $\gamma(r,t)$ is given by

$$\gamma(r,t) = -N(r,t), \tag{4.5}$$

where $N(r,t)$ is the number density of that cluster (the number of such clusters per lattice point or per atom). For all other (r,t) (that are subclusters of the base clusters), we have

$$\gamma(r,t) = -N(r,t) - \sum_{q=r+1}^{r_{\max}} \sum_{s} M(r,t;q,s)\gamma(q,s), \tag{4.6}$$

where $M(r,t;q,s)$ is the number of (r,t) clusters contained in a (q,s) cluster.

In general, the summation over (r,t) in Eq. 4.3 should be carried out over all subclusters of the base clusters. It would seem, therefore, that we would need to calculate $\gamma(r,t)$ for all subclusters of the base clusters. However, the structure of the expressions for $\gamma(r,t)$ in Eqs. 4.5 and 4.6 is such that many of these $\gamma(r,t)$ are identically zero. For instance, if (r',t') is the largest proper subcluster[3] and if it is not wholly included in the intersection of any two of the base clusters, the latter being related by the symmetry operations of the crystal lattice, we can write

$$N(r',t') = \sum_{(r,t)} M(r',t';r,t)N(r,t), \tag{4.7}$$

where the summation over (r,t) takes into consideration all the base clusters greater than the (r',t') cluster. The result is that $\gamma(r',t')$ vanishes according to Eqs. 4.5 and 4.6. It follows then that beginning with the base clusters and working our way down to smaller and smaller proper subclusters, we need consider only those proper subclusters that are wholly contained in the intersection of any two of the larger subclusters with nonvanishing γ, the latter once again being related by the symmetry operations of the crystal lattice. Finding all nonvanishing γ is thus quite straightforward.

---

[3] A proper subcluster is a subcluster that is not identical to any of the base clusters. (*c.f.* proper subset)

4.1.2 Computer Calculation of Cluster Entropy Expressions

Although we have shown in the previous section that many of the $\gamma(r,t)$ coefficients in Eq. 4.3 vanish, there can still be enough nonvanishing $\gamma(r,t)$ to be a nuisance. This is especially true as the sizes of the base clusters are increased in a desire for greater accuracy. It would be useful to have a means of automating the calculation of the $\gamma(r,t)$ coefficients. Successful implementation of an algorithm for doing so requires, among other things, a simple and efficient means of calculating $N(r,t)$ and $M(r,t;q,s)$ in Eqs. 4.5 and 4.6. We therefore introduce a few concepts from group theory that should prove useful for the purpose of quantifying $N(r,t)$ and $M(r,t;q,s)$ for arbitrary clusters.

We begin with the definition of the *normalizer* of a cluster [11]. The normalizer $\mathcal{N}_{(r,t)}(G)$ of a cluster (r,t) with respect to the space group G of a crystal lattice is the subset of the elements of G which leave the cluster (r,t) invariant:

$$\mathcal{N}_{(r,t)}(G) \equiv \{g \in G; g\,(r,t) = (r,t)\}. \tag{4.8}$$

$\mathcal{N}_{(r,t)}(G)$ is a subgroup of G of finite order. Furthermore, the order of the point group Γ of the crystal lattice is an integral multiple of the order of $\mathcal{N}_{(r,t)}(G)$. This follows from the fact that $\mathcal{N}_{(r,t)}(G)$ is also a (finite) subgroup of Γ, which latter also happens to be finite. The number density $N(r,t)$ of the cluster (r,t) is then given by the order $|\Gamma|$ of Γ divided by the order $|\mathcal{N}_{(r,t)}(G)|$ of $\mathcal{N}_{(r,t)}(G)$:

$$N(r,t) = |\Gamma|/|\mathcal{N}_{(r,t)}(G)|. \tag{4.9}$$

So we see that a simple means of calculating $N(r,t)$ for arbitrary (r,t) presents itself: We simply count the number of elements of Γ which leave $N(r,t)$ invariant and apply Eq. 4.9. This algorithm is the core of the subroutine `clus_count()` in Appendix C.

We illustrate the above method by calculating $N(r,t)$ for the 4-point irregular tetrahedron cluster on the body-centered cubic lattice and the 4-point square cluster on the two-dimensional square lattice. The point group Γ is $m3m$ for (face-centered, body-centered, and simple) cubic lattices and its order $|\Gamma|$ is 48. The normalizer $\mathcal{N}_{(r,t)}(G)$ of the tetrahedron cluster with respect to $m3m$ is $mm2$ and its order $|\mathcal{N}_{(r,t)}(G)|$ is 12. Using Eq. 4.9, we obtain $48/12 = 4$ for the number density $N(r,t)$ of the tetrahedron cluster on the body-centered cubic lattice. The point group of the two-dimensional square lattice is $4mm$, which has order 8 and is also the normalizer of the square cluster with respect to the square lattice. It comes as no surprise then that the number density of square cluster on the square lattice is 1.

We next require a scheme for calculating $M(r,t;q,s)$ for arbitrary clusters (r,t) and (q,s). The idea which comes to mind is to consider all $\binom{q}{r}$ r-point subclusters of (q,s) and keep a running tally of how many of these are equivalent to the given (r,t) cluster. This is in fact the algorithm that is used in the subroutine `sub_count()` in Appendix C. The source file `clus.c`, which contains the subroutine `sub_count()`, is generated by the program `gen_clus`.

We had mentioned in the previous section that only relatively few of the subclusters of the base clusters contribute terms with nonvanishing $\gamma(r,t)$ to Eq. 4.6. There we outlined a method for weeding out subclusters with trivial $\gamma(r,t)$. In the present implementation of the program for calculating the $\gamma(r,t)$ coefficients, we use the more straightforward technique of checking *all* subclusters of the base cluster. This brute force method for considering subclusters of the base clusters, while easy to implement, has a computational cost that goes as 2^r for each r-point base cluster. This results in the execution time of the program increasing quite rapidly with the size of the base clusters. While this was not a major obstacle for the results presented here—the largest base cluster considered here was the 15-point "stellated cube" cluster on the body-centered cubic lattice—we intend to improve upon this procedure along the lines sketched above in future work.

We are not yet done, however. We still need a means of deciding if any two given clusters are equivalent. Obviously, for this to be true it is, at a minimum, necessary that the two clusters have the same number of points. Given this fact, we then use the property mentioned in the previous section that any two r-point cluster are equivalent if they are related to each other by at least one of the symmetry operations (space group elements) of the crystal lattice. Finding such a space group element is not as formidable as it may seem. This is because although the space group G of the crystal lattice is of infinite order, it is, thankfully, not necessary to consider all its elements. We need only consider all the elements of the (finite) point group Γ of the crystal lattice and determine if the result of the operation of one of these point group elements on one of the clusters differs from the other cluster by a translational vector of the crystal lattice. If we can find at least one such point group element, the two clusters are equivalent. The above method for determining if two arbitrary clusters are equivalent is used in the subroutine `clus_comp()` in Appendix C.

In summary, the algorithm for the determination of $\gamma(r,t)$ for an arbitrary set of base clusters is as follows:

- calculate the number densities $N(r,t)$ of the base clusters,
- enumerate all distinct subclusters of the base clusters,
- calculate the number densities $N(r,t)$ of the nonequivalent subclusters of the base clusters,
- beginning with the largest clusters and working our way down to the smallest, calculate $M(r,t;q,s)$ and $\gamma(r,t)$.

The implementational details are somewhat more involved than this but have less to do with the physics of the problem than with mere computational contrivances, and need not concern us here. The complete source code for the computer program `gcvm` for the calculation of the $\gamma(r,t)$ coefficients is given in Appendix C.

4.2 The Choice of Base Clusters

It has been pointed out earlier that the CVM formalism does not prescribe the choice of base cluster(s) to be used. Traditionally, the critical temperature T_c predicted by a particular choice of base cluster(s) has been used as one of the measures of that method's accuracy. By this yardstick, it has been found that employing larger base clusters generally gives better approximations [14,17–19]. Exceptions abound however—for instance, it is well known that in fcc systems that the double-tetrahedron approximation gives a less accurate value for T_c than the (single) tetrahedron approximation in spite of the larger base cluster of the former [14]. For the purpose of the present work, we employed the entropy and free energy expressions corresponding to a variety of base cluster sets on the bcc lattice. In order of increasing accuracy, these are the: a) point, b) pair, c) tetrahedron, d) octahedron, and e) octahedron–cube approximations (see Fig. 4.1).

4.3 The Hybrid Monte Carlo–Cluster Variation Method

The algorithm for our Monte Carlo simulations has been described in detail elsewhere (see Ref. [20] and the references therein) as well as in Chapter 3 of this thesis. For the present work we used a bcc lattice of $64 \times 64 \times 64 \times 2 = 524\ 288$ atoms, unless stated otherwise. The crystal lattice was initially randomly seeded with A and B atoms in a $1:1$ ratio (AB stoichiometry) with one of the sites left

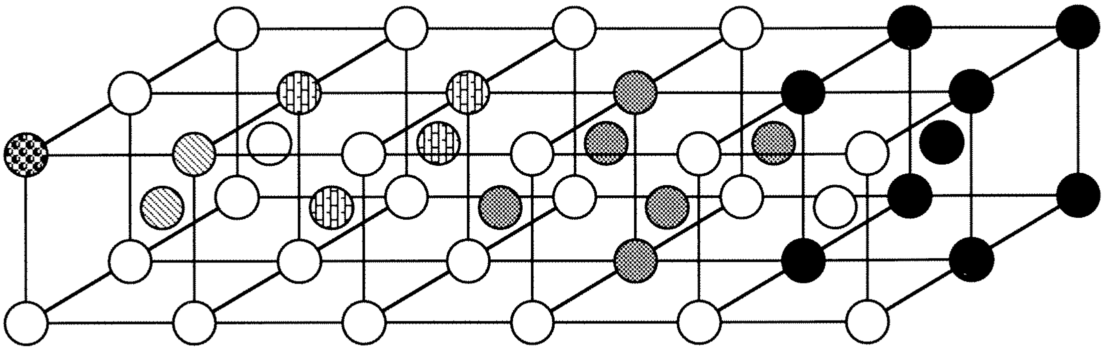

Figure 4.1: A portion of the bcc lattice showing (from left to right) the a) point, b) pair, c) tetrahedron, d) octahedron, and e) cube clusters.

vacant. This latter vacancy served as the agent of the mechanism of ordering. In our vacancy mechanism of ordering, the eight first-nearest neighbors of the vacancy had Boltzmann probabilities for exchanging sites with the vacancy. A pair interaction model using first- (1nn) and second- nearest-neighbor (2nn) pair interactions was used for obtaining the Boltzmann factors, which were used as weights in the random selection of an atom-vacancy interchange. B2 and/or B32 order was allowed to develop in the initially disordered crystal lattice by annealing at a fixed finite temperature below the critical temperature for ordering. During the Monte Carlo simulations, we kept track of the SRO and LRO parameters. The Warren-Cowley SRO parameters were obtained by counting the A–A, B–B, and A–B pairs for each near-neighbor shell and applying the usual formulae. The LRO parameters were obtained from the diffraction pattern of the crystal lattice, calculated by obtaining the three-dimensional Fourier transform of our alloy. The intensities of the $(\frac{1}{2}\frac{1}{2}\frac{1}{2})$ and (100) superlattice diffraction peaks were normalized by that of the (110) fundamental peak and used as measures of the B32 and B2 LRO parameters, respectively.

In addition, we periodically computed the configurational entropy and free energy of the crystal. This was done by counting the frequencies of the various cluster types that enter into the well-known CVM formulae [14] for the entropy. Knowing the value of S in the various cluster approximations, we computed E by summing the energies of the various 1nn and 2nn pairs, and then used Eq. 1 to obtain the corresponding approximations for F. In principle, the statistical accuracy of F is limited by the size of the Monte Carlo crystal being studied. In the present study, we chose to maximize the accuracy by counting all the clusters of a given cluster type in the crystal lattice. This was possible as there were only about half a million atoms in the Monte Carlo crystal. (The number of clusters of any given cluster type is equal to a small integral multiple of the number of atoms.) We had no problems with statistical accuracy or reproducibility, but problems could arise with larger base clusters. The larger the cluster type, the smaller (on average) the individual cluster probabilities for that cluster type, and the more susceptible these are to statistical fluctuations. It could therefore become necessary to use as large a crystal lattice as possible, or to perform ensemble averaging in order to maximize the precision of the estimated S and F.

4.4 Results and Discussion

Using this new computational tool to monitor the free energy in our Monte Carlo simulations, we followed the change in the free energy density as an initially disordered alloy developed order. Figure 4.2 shows the change in the (100) superlattice intensity as a function of Monte Carlo step for an equiatomic binary alloy with $V^1_{\mathrm{AA}} = V^1_{\mathrm{BB}} = 1.00$. The interatomic interaction potentials are in units of $k_B T$, and this particular choice corresponds to a temperature of $0.315\, T_c$. The (100) superlattice intensity increases monotonically until it reaches an approximate plateau at about 250 Monte Carlo steps. This increase of the (100) intensity reflects the growth of B2 order, which is the equilibrium phase for this particular choice of pair interactions. At this point (at $\sim$ 250 Monte Carlo steps) the alloy has reached equilibrium and consists of a single well- ordered B2 domain. (The additional very slight increase in the (100) intensity after 250 Monte Carlo steps is due to the "annealing out" of some of the single-site defects in the alloy [21].) Also shown in Fig. 4.2 are the point (solid line), tetrahedron (dotted line), octahedron (dashed line), and octahedron–cube (dotted dashed line) approximations to the free energy density (in units of $k_B T$). These exhibit the same general trend of a monotonic decrease in F until about 250 Monte Carlo steps, from which point on there is only a barely perceptible additional decrease and the alloy is essentially at equilibrium.

It is interesting to compare the results for the different approximations of F (Fig. 4.2). Initially (at 0 Monte Carlo steps), the configurational entropy density is $\ln 2$ for all levels of approximation. This is because the initial random configuration corresponds to $T = \infty$; and all CVM configurational entropy and free energy expressions are exact in the high-temperature limit [14]. As order evolves in the alloy, however, the free energy curves from the various approximations begin to deviate from each other, although all four curves show the same qualitative trends. In the point-approximation, the free energy density is just the internal energy density offset by $\ln 2$. The free energy densities from the tetrahedron, octahedron, and octahedron–cube approximations are similar to each other, suggesting that they are probably close to the exact value. The deviation among these three curves gives a rough estimate of the error resulting from truncating the approximation at the octahedron–cube level. Another estimate can be obtained from the absolute value of F at equilibrium—for the exact case corresponding to Fig. 4.2, we must have $F \approx 0$ for nearly perfect B2 order because $E \approx 0$ (very few 1nn A–A and B–B bonds) and $S \approx 0$ (nearly perfect order).

The above approximations of F obtained using our hybrid CVM–Monte Carlo technique are in principle quite different from the corresponding approximations using conventional CVM and PPM. This is because while both approaches employ the same level of approximation in obtaining the configurational entropy S, the same is not true of the internal energy E. The internal energy in the hybrid CVM–Monte Carlo method is essentially exact for the large crystal lattices used here, irrespective of the level of cluster approximation used to calculate the configurational entropy. In contrast, the internal energy in conventional CVM and

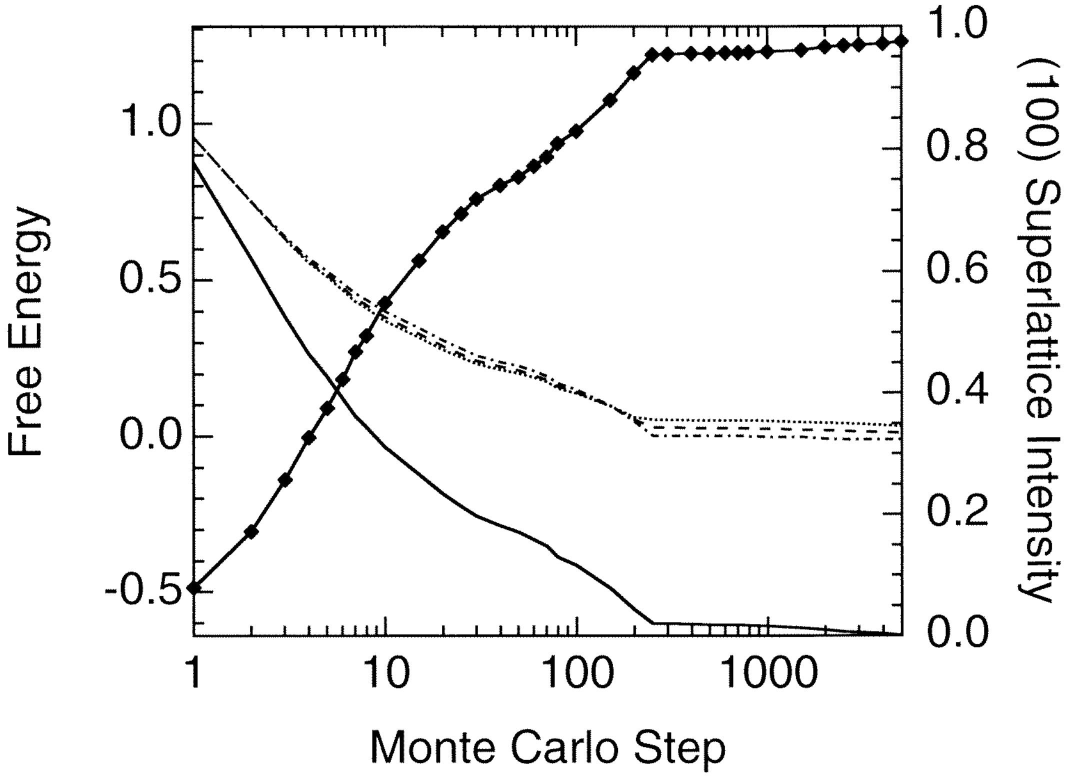

Figure 4.2: Graph showing the growth of the (100) superlattice diffraction intensity (diamonds) as a function of Monte Carlo step for an initially disordered equiatomic binary alloy with $V^1_{\mathrm{AA}} = V^1_{\mathrm{BB}} = 1.00$ (in units of k_BT). Also shown, on the same horizontal axis, are the point (solid line), tetrahedron (dotted line), octahedron (dashed line), and octahedron–cube (dotted dashed line) approximations to the free energy density (in units of k_BT).

PPM is limited by the same level of approximation as is used in calculating the configurational entropy.

Figure 4.3 shows the variation of the $(\frac{1}{2}\frac{1}{2}\frac{1}{2})$ and (100) superlattice diffraction intensities as functions of Monte Carlo step for an equiatomic binary alloy with $V^1_{\mathrm{AA}} = V^1_{\mathrm{BB}} = 1.00$; $V^2_{\mathrm{AA}} = V^2_{\mathrm{BB}} = 0.70$ (in units of k_BT). For this particular choice of pair interaction the equilibrium state is one of B32 order. The $(\frac{1}{2}\frac{1}{2}\frac{1}{2})$ superlattice intensity, which reflects B32 order, increases monotonically until it reaches its equilibrium plateau after about 1500 Monte Carlo steps. (The sharp increase in the $(\frac{1}{2}\frac{1}{2}\frac{1}{2})$ superlattice intensity at about 1000 Monte Carlo steps, just before equilibrium is reached, is due to the annihilation of antiphase domain boundaries.) Meanwhile, the (100) superlattice intensity, which reflects B2 order, increases initially until it reaches its maximum value at about 10 Monte Carlo steps. After that, it begins to decrease monotonically until it has practically vanished by the time equilibrium is reached. Also shown in Fig. 4.3, on the same horizontal axis, is the octahedron–cube (dotted dashed line) approximation to the free energy density, which decreases monotonically until it reaches its equilibrium value of approximately 1.97 (in units of k_BT) after about 1000 Monte Carlo steps. For the exact case corresponding to Fig. 4.3, we would have $F \approx 2.0$ for nearly perfect B32 order because $E \approx 2.0$ (approximately one 1nn A–A bond and one 1nn B–B bond per atom) and $S \approx 0$ (nearly perfect order).

The transient appearance of B2 order in this simulation has analogs in similar studies of disorder→order transformations carried out using analytical techniques such as the master equation method and PPM [22–25]. Such transient states have been termed "pseudostable" elsewhere in the literature [23,24]. In the earlier analytical work, such transient or pseudostable states have been shown to be associated with a stationary point or saddle point in the free energy surface

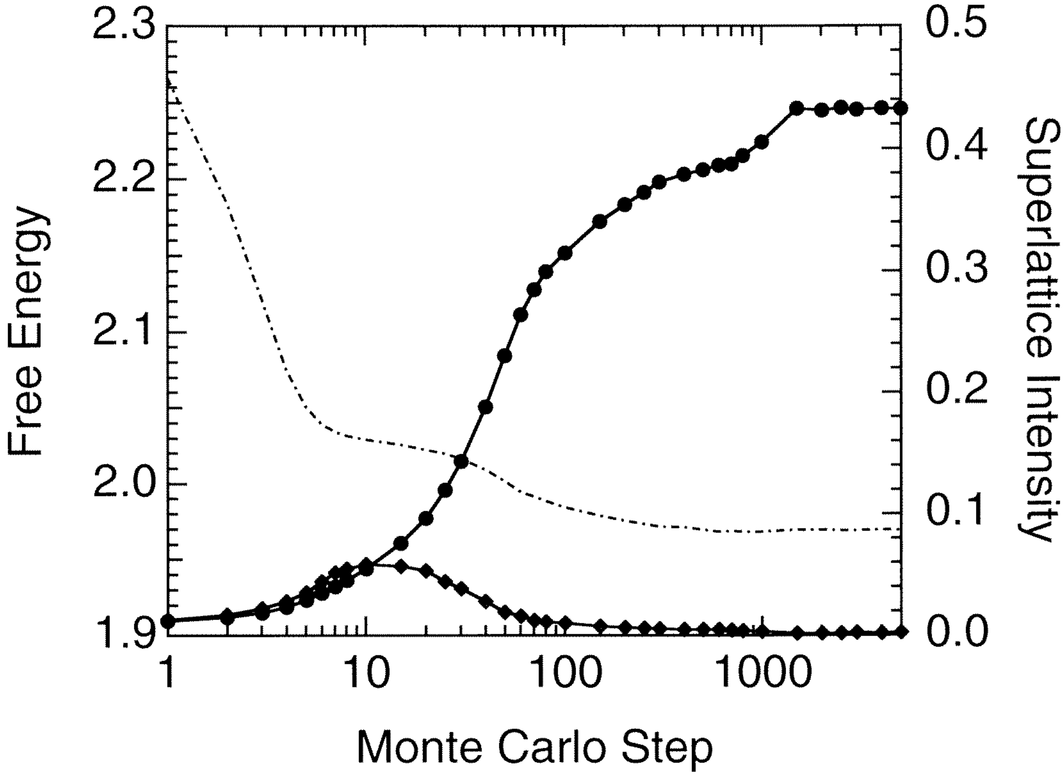

Figure 4.3: Graph showing the variation of the $(\frac{1}{2}\frac{1}{2}\frac{1}{2})$ (circles) and (100) (diamonds) superlattice diffraction intensities as a function of Monte Carlo step for an initially disordered equiatomic binary alloy with $V^1_{\rm AA} = V^1_{\rm BB} = 1.00$; $V^2_{\rm AA} = V^2_{\rm BB} = 0.70$ (in units of k_BT). Also shown, on the same horizontal axis, is the octahedron–cube (dotted dashed line) approximation to the free energy density (in units of k_BT).

[24]. Based on the approximation to the free energy shown in Fig. 4.3, a similar association appears to exist here. As expected, the free energy density decreases monotonically with Monte Carlo step. However, there appears to be an approximate plateau in F where the (100) superlattice intensity reaches its maximum. This is not unlike the behavior of the free energy density reported in Ref. [23]. The often long-lived nature of those transient states was attributed to the vanishing of the free energy gradient, and hence the thermodynamic driving force, in the vicinity of the stationary point in the free energy surface [23,24].

The above results can also be explained heuristically as follows. The phase boundary between B2 and B32 in the ground state ($T = 0$) occurs at $\frac{V^2}{V^1} = \frac{2}{3}$ [26]. This is close to the value of $\frac{V^2}{V^1}$ used in the simulation of Fig. 4.3. We therefore expect the thermodynamic driving forces for the formation of the two types of order, B2 and B32, to be very similar for the conditions of this simulation. The alloy in its initial random configuration is in a highly nonequilibrium state. Its free energy is very much higher than what it would eventually be in the equilibrium B32-ordered state. It can begin to dispose of this excess free energy by forming domains of not only B32 order but B2 order as well. Some local regions in a random alloy are B2-like, and can form B2-type order more expediently than B32. (Although the B2 domains in this simulation may have a higher free energy density than the B32 domains, it is still much less than that of the initial disordered state.) This accounts for the large drop in F in the early stages of the simulation (from 1 to about 10 Monte Carlo steps). In fact, examination of the simulated microstructure of the transient state (at $\sim$ 10 Monte Carlo steps) showed it to consist of small domains of B2 and B32 order of a few lattice constants in diameter. However, once the initial disordered state has been replaced by these microdomains of B2 and B32 order, any further decrease in the free energy can only be achieved by the growth of the B32 domains at the expense of the B2 domains. This is indeed what occurs in the next stage of the simulation (from $\sim$ 10 Monte Carlo steps onwards). As expected, the resulting additional drop in F is much less than that in the first stage because of the presumably much smaller free energy difference between B2 and B32 order.

We repeated the simulation of Fig. 4.3 using a crystal lattice $\frac{1}{8}$ the volume of the previous crystal lattice but performed 8 times with 8 different random number seeds. The resulting aggregate $(\frac{1}{2}\frac{1}{2}\frac{1}{2})$ and (100) superlattice diffraction intensities and free energy density in the octahedron–cube approximation as a function of Monte Carlo step are shown in Fig. 4.4. These can be seen to be essentially identical to the corresponding curves obtained in the previous figure. However, a couple of dissimilarities are worth noting. The sharp increase in the $(\frac{1}{2}\frac{1}{2}\frac{1}{2})$ superlattice intensity which previously occurred at about 1000 Monte Carlo steps in Fig. 4.3 and which we attributed to the annihilation of antiphase domain boundaries appears shifted slightly to the left in Fig. 4.4. Furthermore, the averaging process has also smeared out this previously sharp increase in the $(\frac{1}{2}\frac{1}{2}\frac{1}{2})$ superlattice intensity and made it less distinct. This is because the precise moment when the annihilation of the antiphase domain boundaries occurs varies stochastically from one Monte Carlo run to another when different random number seeds are used. These minor differences aside, the similarities between Figs. 4.3 and 4.4 suggest the feasibility of using ensemble averaging in concert with the methods described above to increase the precision of our free energy estimates. This should be a particularly useful capability when extending our scheme to larger base clusters.

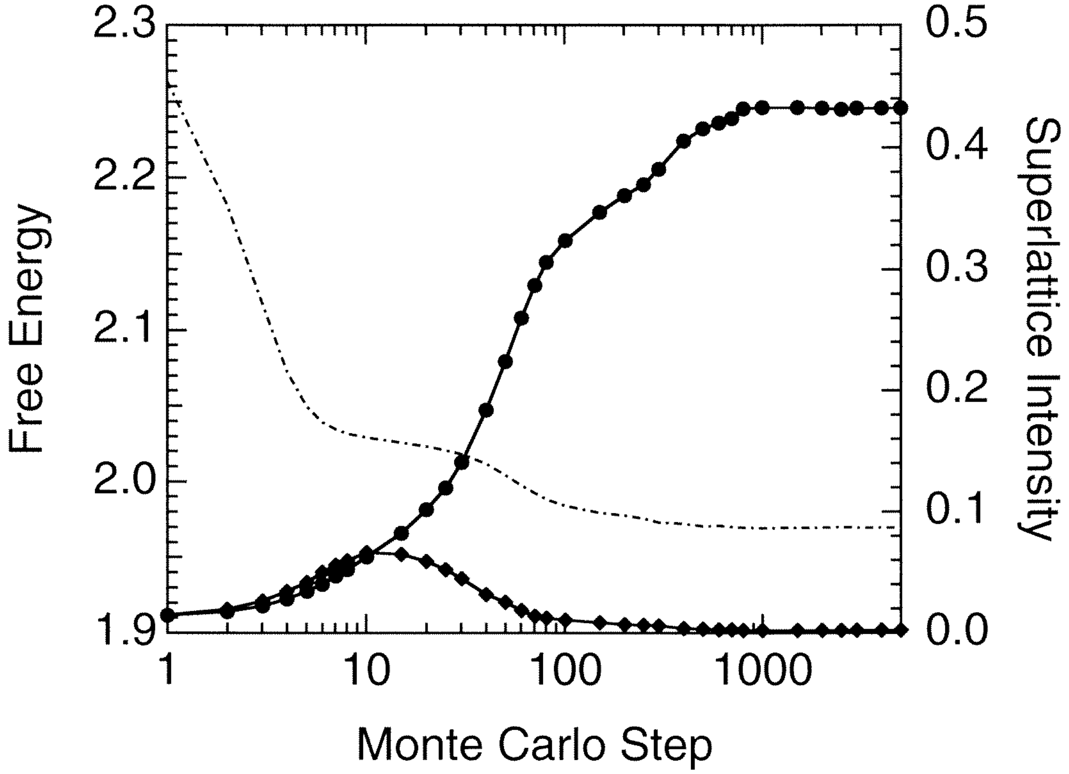

Figure 4.4: Graph showing the variation of the $(\frac{1}{2}\frac{1}{2}\frac{1}{2})$ (circles) and (100) (diamonds) superlattice diffraction intensities as well as the octahedron–cube (dotted dashed line) approximation to the free energy density (in units of k_BT) as a function of Monte Carlo step. The data were obtained under conditions identical to those of Fig. 4.3 except that 8 independent simulations were performed using a crystal lattice $\frac{1}{8}$ the size of that in Fig. 4.3, and their results averaged.

4.5 Conclusions

We have developed and implemented a technique for extracting configurational entropies and free energies from kinetic Monte Carlo simulations. The method uses ideas borrowed from the cluster variation method. The Monte Carlo simulations are carried out in the usual manner; in addition, the simulated lattice was periodically sampled for pertinent cluster probabilities, which were then used in the cluster variation method's free energy expressions. A computer program facilitated the derivation of the coefficients in these free energy expression for any given choice of base clusters. We were able to obtain a range of approximations to the free energy depending on the choice of base clusters used. Using the best of these (the octahedron–cube approximation), we were able to verify that the free energy density decreased monotonically with time as order evolved in an initially disordered alloy. We were also able to show that the free energy versus time curve approximated a plateau in the neighborhood of a transient B2 state in system that exhibited B32 order at equilibrium. Based on these findings, we speculate that this transient B2 state, which appears to be at or near a nonequilibrium stationary point in the free energy surface, could be an example of a psuedostable state.

References

[1] L. Anthony, unpublished results.

[2] R. Kikuchi, *J. Chem. Phys.* **60**, 1071 (1974).

[3] K. Binder, *J. Comp. Phys.* **59**, 1 (1985).

[4] R. Kikuchi, *Ann. Phys.* **10**, 127 (1960).

[5] R. Kikuchi, *Suppl. Prog. Theor. Phys.* **35**, 1 (1966).

[6] R. Kikuchi, *Phys. Rev.* **81**, 988 (1951).

[7] M. Kurata, R. Kikuchi, and T. Watari, *J. Chem. Phys.* **21**, 434 (1953).

[8] A. G. Schlijper and B. Smit, *J. Stat. Phys.* **56**, 247 (1989).

[9] A. G. Schlijper, A. R. D. van Bergen, and B. Smit, *Phys. Rev. A* **41**, 1175 (1990).

[10] C. Bichara and G. Inden, "Gibbs energies and chemical potentials of solid solution phases—a combined Monte Carlo and cluster variation approach," to be published.

[11] D. Gratias, J. M. Sanchez, and D. de Fontaine, *Physica* **113A**, 315 (1982).

[12] J. A. Barker, *Proc. Roy. Soc. A* **216**, 45 (1953).

[13] T. Morita, *J. Math. Phys.* **13**, 115 (1972).

[14] J. M. Sanchez and D. de Fontaine, *Phys. Rev. B* **17**, 2926 (1978).

[15] J. M. Sanchez, F. Ducastelle, and D. Gratias, *Physica A* **128**, 334 (1984).

[16] F. Ducastelle, *Order and phase stability in alloys*, (North-Holland, Amsterdam, The Netherlands, 1991), Section 4.3.

[17] A. G. Schlijper, *J. Stat. Phys.* **40**, 1 (1985).

[18] A. Finel, Thèse de Doctorat d'Etat, Université Paris (1987).

[19] R. Kikuchi, "CVM entropy algebra," to be published.

[20] T. Lindsey and B. Fultz, in *Diffusion in Ordered Alloys*, edited by B. Fultz, R. W. Cahn, and D. Gupta, TMS EMPMD Monograph Series **4** (The Minerals Metals & Materials Society, Warrendale, Pennsylvania, 1993).

[21] B. Fultz, *J. Chem. Phys.* **88**, 3227 (1988).

[22] L. Anthony and B. Fultz, *J. Mater. Res.* **4**, 1132 (1989).

[23] R. Kikuchi, T. Mohri, and B. Fultz, in *Kinetics of Phase Transformations*, edited by M. O. Thompson, M. J. Aziz, and G. B. Stephenson, *Mater. Res. Soc. Symp. Proc.* **205** (Materials Research Society, Pittsburgh, Pennsylvania, 1992).

[24] B. Fultz, *Philos. Mag. B* **67**, 253 (1993).

[25] L. Anthony and B. Fultz, "Kinetics of B2, $D0_3$, and B32 ordering: Results from pair approximation calculations and Monte Carlo simulations," *J. Mater. Res.*, submitted.

[26] M. J. Richards and J. W. Cahn, *Acta Metall.* **19**, 1263 (1971).

Chapter 5

Summary and Perspective

In the previous three chapters, I presented and discussed representative results of kinetic processes obtained using three distinct methods. We were able to distinguish various points of commonality among the results obtained using these different approaches. Furthermore, significant trends were observed as the level of approximation was increased, from the point approximation of the master equation method through the pair approximation of the path probability method to the nearly exact hybrid Monte Carlo–cluster variation method. In this final chapter of the thesis, I shall compare and summarize the main results obtained previously. In the process, I shall present experimental evidence from the Fe_3Al system which is supportive of some of these conclusions. Finally, I shall conclude this chapter by presenting some of my thoughts on the future directions of the research presented in this dissertation.

5.1 Comparison of Analytical and Monte Carlo Results

Using the three kinetic models, we were able to obtain equilibrium critical potentials for B2 and $D0_3$ order as a function of the ratio of 2nn to 1nn interaction strengths. These showed the expected thermodynamic trends. For instance, with only 1nn interactions, the critical potentials for B2 order increased (the critical temperature decreased) with increasing level of approximation. As the ratio of 2nn to 1nn interaction strengths were increased, the critical potentials for B2 order increased, whereas the critical potentials for $D0_3$ order decreased. However, the critical potentials for the path probability method in the pair approximation exhibited pathological behavior for intermediate values of this ratio. This is probably due to the fact that we used chained 1nn pair probabilities to obtain 2nn pair probabilities in an implementation that has only 1nn pairs as the maximal cluster. One possible means of avoiding this problem would be to use larger base clusters, such as 1nn and 2nn pairs together or the tetrahedron cluster. Another possibility might be to obtain the 2nn pair probabilities as products of corresponding point probabilities.

Both analytical methods exhibited strong temperature dependence of kinetic paths through order parameter space. In general, as the temperature was lowered, the evolution from initial disorder to equilibrium order displayed more of a two-stage ordering process. In other words, as the temperature is lowered, the initial growth of one of the two order parameters is suppressed relative to that of the other. This can be understood as a difference in the effective activation energies for the two types of ordering. Lowering the temperature, then, will tend to accentuate the difference in the kinetics of the two types of order.

We were able to obtain transient B32 order along the way to equilibrium $D0_3$ order using all three techniques. As the level of approximation was improved, this transient B32 order became less prominent, and the B32 order parameter showed less of an extended plateau as a function of integration or Monte Carlo step and more of a log-normal peak. We were able to show that during the appearance of this transient order, the free energy was approximately stationary in time. In the case of the point approximation, we were further able to associate this transient state with a saddle point in free energy surface as a function of order parameter. Using the Monte Carlo method, we were able to demonstrate that this transient order was most pronounced near the (equilibrium) phase boundary between the two competing types of order.

5.2 Experimental Evidence

In this section, I shall present some of my experimental work on the temperature dependence of kinetic paths in rapidly solidified powders of Fe_3Al. I shall also present some results obtained by Gao *et al.* which exhibit evidence of transient B32-like order obtained during the early stages of ordering in splat-quenched foils of Fe_3Al.

5.2.1 Temperature Dependence of Kinetic Paths in Fe_3Al

The Fe_3Al materials used in this study were rapidly solidified powders (RSP) made by the Pratt and Whitney Corp. using centrifugal atomization. The cooling rate was estimated to be 10^4 K s^{-1}. Chemical analysis of the powder by inductively coupled plasma analysis gave a composition of 74.0 at. % Fe and 26.0 at. % Al. The powder was sealed under vacuum in borosilicate glass ampules and the ampules were annealed for various times at 200 °C, 250 °C, 300 °C, and 350 °C. These temperatures were chosen because they were well below the critical temperature for $D0_3$ ordering (550 °C). Thus, we would expect the equilibrium LRO parameter at these temperatures for both B2 and $D0_3$ ordering to be very close to unity, and thus also very close to each other. In this way, we can ensure that any "equilibrium effects" are equal for the various temperature series. Any differences in the evolution of LRO in these temperature series could then be attributed to "kinetic effects".

The x-ray diffractometry measurements were performed at room temperature with a GE XRD–5 θ–2θ diffractometer using Cr Kα radiation. To obtain D0_3 and B2 LRO parameters, we used the $(\frac{1}{2}\frac{1}{2}\frac{1}{2})$ and (100) x-ray diffractions, respectively, because these were the most intense peaks indicating those degrees of order. We examined some sample-to-sample variations in the ratios of fundamental peaks in order to identify crystallographic textural effects and found these variations to be small, as expected in powders.

For calibration purposes, we performed calculations of the Cr Kα x-ray diffraction intensities by means of a Rietveld [1] powder diffraction code that was modified to include Lorentz polarization factors and x-ray atomic scattering factors for Cr Kα radiation. Using a model crystal of Fe$_3$Al with stoichiometric composition and perfect D0_3 order, from these calculations we obtained $\left(\frac{I_{\frac{1}{2}\frac{1}{2}\frac{1}{2}}}{I_{110}}\right)_{\text{calc}} = 7.38\%$ and $\left(\frac{I_{100}}{I_{110}}\right)_{\text{calc}} = 3.68\%$ (corresponding to the LRO parameters: $S_{\text{D}0_3} = 1.0$, and $S_{\text{B2}} = 1.0$). We used these results as scaling factors for converting our measurements of superlattice peak intensities into the LRO parameters $S_{\text{D}0_3}$ and S_{B2}. We point out that our principal result of a temperature dependence of the kinetic paths will not be qualitatively affected by inaccuracies in the intensity calculations (such inaccuracies would merely scale the axes of the $(S_{\text{D}0_3}, S_{\text{B2}})$-space in Fig. 5.1).

Intensities of the $(\frac{1}{2}\frac{1}{2}\frac{1}{2})$ and (100) superlattice peaks, and of the (110) fundamental peak, were obtained from the diffraction profiles by integrating the background-corrected peaks. The intensities of the $(\frac{1}{2}\frac{1}{2}\frac{1}{2})$ and (100) superlattice peaks were first divided by the intensities of the corresponding (110) fundamental peaks. The B2 and D0_3 order parameters were then obtained by taking the square roots of the ratios of these normalized intensities to those obtained from the intensity calculations for perfectly ordered stoichiometric Fe_3Al

$$S_{\mathrm{D0_3}} = \left[\left(\frac{I_{\frac{1}{2}\frac{1}{2}\frac{1}{2}}}{I_{110}} \right)_{\mathrm{exper}} \Bigg/ \left(\frac{I_{\frac{1}{2}\frac{1}{2}\frac{1}{2}}}{I_{110}} \right)_{\mathrm{calc}} \right]^{\frac{1}{2}}, \tag{5.1}$$

$$S_{\mathrm{B2}} = \left[\left(\frac{I_{100}}{I_{110}} \right)_{\mathrm{exper}} \Bigg/ \left(\frac{I_{100}}{I_{110}} \right)_{\mathrm{calc}} \right]^{\frac{1}{2}}. \tag{5.2}$$

When the LRO parameters S_{B2} and $S_{\mathrm{D0_3}}$ were plotted against each other, it was found that the relative rates of increase of S_{B2} and $S_{\mathrm{D0_3}}$ had a significant temperature dependence. Figure 5.1 presents our experimental data on the temperature dependence of the kinetic paths of the order parameters S_{B2} and $S_{\mathrm{D0_3}}$. The straight line represents a linear least squares fit to the experimental data obtained for that particular annealing temperature. It is possible to quantify this temperature dependence of the relative rates of increase of S_{B2} and $S_{\mathrm{D0_3}}$ in terms of a difference in the activation energies of the two types of ordering. We write the rates of change of the LRO parameters, $\dot{S}_{\mathrm{B2}}$ and $\dot{S}_{\mathrm{D0_3}}$, as

$$\dot{S}_{\mathrm{B2}} = \dot{S}^0_{\mathrm{B2}} \exp(-Q_{\mathrm{B2}}/RT), \tag{5.3}$$

$$\dot{S}_{\mathrm{D0_3}} = \dot{S}^0_{\mathrm{D0_3}} \exp(-Q_{\mathrm{D0_3}}/RT), \tag{5.4}$$

where Q_{B2} and $Q_{\mathrm{D0_3}}$ are the activation energies for B2 and $D0_3$ ordering respectively. It follows that

$$\frac{\dot{S}_{\mathrm{B2}}}{\dot{S}_{\mathrm{D0_3}}} = \frac{\dot{S}^0_{\mathrm{B2}}}{\dot{S}^0_{\mathrm{D0_3}}} \exp(\Delta Q/RT), \tag{5.5}$$

and

$$\frac{dS_{\mathrm{B2}}}{dS_{\mathrm{D0_3}}} = \frac{\dot{S}^0_{\mathrm{B2}}}{\dot{S}^0_{\mathrm{D0_3}}} \exp(\Delta Q/RT), \tag{5.6}$$

where $\Delta Q \equiv Q_{\mathrm{D0_3}} - Q_{\mathrm{B2}}$.

The slopes of the lines in Fig. 5.1 correspond to $dS_{\mathrm{B2}}/dS_{\mathrm{D0_3}}$ in Eqn. 5.6. These slopes decrease with increasing temperature, suggesting an Arrhenius-type dependence. We performed an Arrhenius analysis of data by plotting $\log(dS_{\mathrm{B2}}/dS_{\mathrm{D0_3}})$

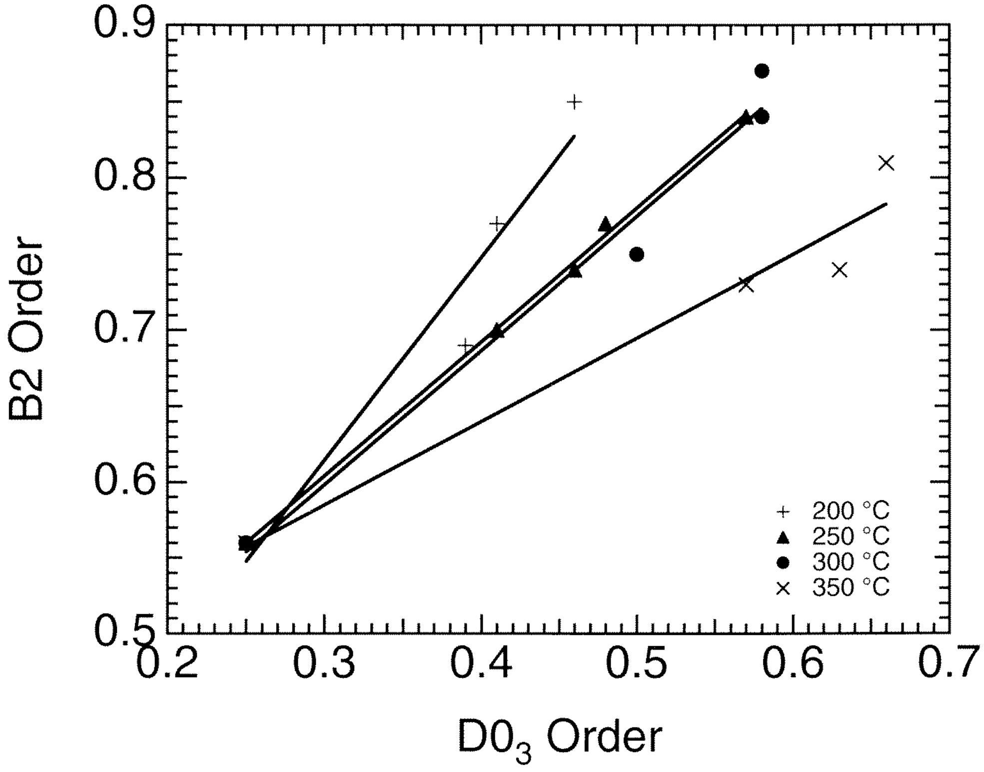

Figure 5.1: Dependence of kinetic paths through $(S_{\mathrm{D0_3}}, S_{\mathrm{B2}})$ order parameter space on annealing temperature for initially disordered Fe_3Al powders. Lines shown are linear fits to data obtained at a given temperature [2].

vs. $(RT)^{-1}$ (not shown). From the slope of the linear fit to the data, we obtain a value of 11.2 kJ mol^{-1} or 2.7 kcal mol^{-1} for ΔQ. (The activation energy for D0$_3$ ordering is higher than that for B2 ordering by this amount.) These temperature-dependent kinetic paths were not reported in a previous study [3], perhaps because the annealings in this previous study were performed at the two rather similar temperatures of 363 and 380 °C.

5.2.2 Transient B32 Order in Fe$_3$Al

Foils of Fe$_3$Al were prepared as chemically disordered bcc solid solutions by piston-anvil quenching and annealed at 300 °C to induce order. The evolution of order was measured using x-ray diffractometry and Mössbauer spectrometry. Figure 5.2 shows the growth of the $(\frac{1}{2}\frac{1}{2}\frac{1}{2})$ and (100) x-ray superlattice diffraction peaks in one of these initially piston-anvil quenched foils that had been annealed at 300 °C for increasing lengths of time. During the first 5 minutes of annealing, the $(\frac{1}{2}\frac{1}{2}\frac{1}{2})$ and (100) peaks increase in the approximately 2 : 1 ratio expected for D0$_3$ order. However, between 5 minutes and 120 minutes, the $(\frac{1}{2}\frac{1}{2}\frac{1}{2})$ peak shows a nearly two-fold increase in intensity while the (100) peak intensity is virtually unchanged. This growth of the $(\frac{1}{2}\frac{1}{2}\frac{1}{2})$ peak without any increase in the (100) peak is indicative of the development of transient B32 long range order. Further annealing of the sample to 2800 minutes recovers the approximately 2 : 1 intensity ratio as equilibrium D0$_3$ order is achieved.

Figure 5.3 shows the ^{57}Fe hyperfine magnetic field distributions obtained from Mössbauer spectrometry of piston-anvil quenched Fe$_3$Al foils for various annealing times at 300 °C. The numbers at the top of the figure identify resonances from ^{57}Fe atoms with different numbers of Al neighbors. The as-quenched sample exhibits an approximately binomial distribution of 1nn Al atoms for the ^{57}Fe atom, as

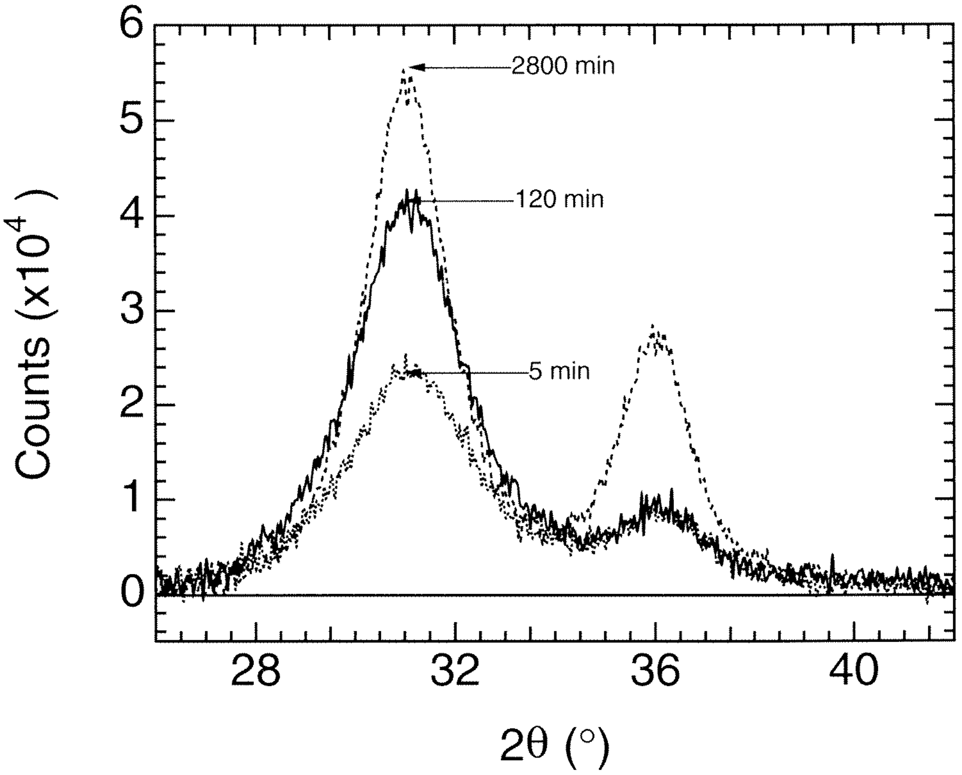

Figure 5.2: Growth of the $(\frac{1}{2}\frac{1}{2}\frac{1}{2})$ (left) and (100) (right) superlattice diffraction peaks in an initially piston-anvil quenched foil of Fe_3Al annealed at 300 °C for various lengths of time [4].

expected for a random solid solution of Fe and Al. During the first 10 minutes of annealing, there is an increase in the 4- and 0-Al peaks in the approximately 2 : 1 ratio expected for $D0_3$ order. However, between 10 minutes and 100 minutes, the hyperfine magnetic field distribution is virtually unchanged. It turns out that the hyperfine magnetic field distributions for a random solid solution and for B32 order are very similar, and we may possibly attribute the stationary hyperfine magnetic field distribution during this time to the transient formation of B32 order from chemical disorder. At any rate, this would be consistent with the x-ray diffractometry data of Fig. 5.2. Further annealing of the sample for longer times than 100 minutes recovers the approximately 2 : 1 intensity ratio of the 4- and 0-Al peaks as equilibrium $D0_3$ order is obtained. The above x-ray diffractometry and Mössbauer spectrometry evidence of transient B32 order are supportive of similar theoretical results obtained in Chapters 2 through 4.

5.3 Future Efforts

From Chapter 2, it is apparent that going from a point approximation to a pair approximation involves a significant increase in the number of state variables (nominally, from 12 to 36) and the complexity of the resulting rate equations. Extending the analytical techniques to even higher cluster approximations should be correspondingly more complicated. As a matter of fact, I must confess that I have attempted to extend the path probability method of Chapter 2 to the tetrahedron approximation, but the difficulties involved have forced me to shelve the project, at least temporarily. However, I take some solace in the knowledge that the tetrahedron approximation has proved to be a worthy challenge to greater minds than mine [5]. At least part of the reason for the difficulty in extending the path probability method of Chapter 2 to the tetrahedron approximation lies in

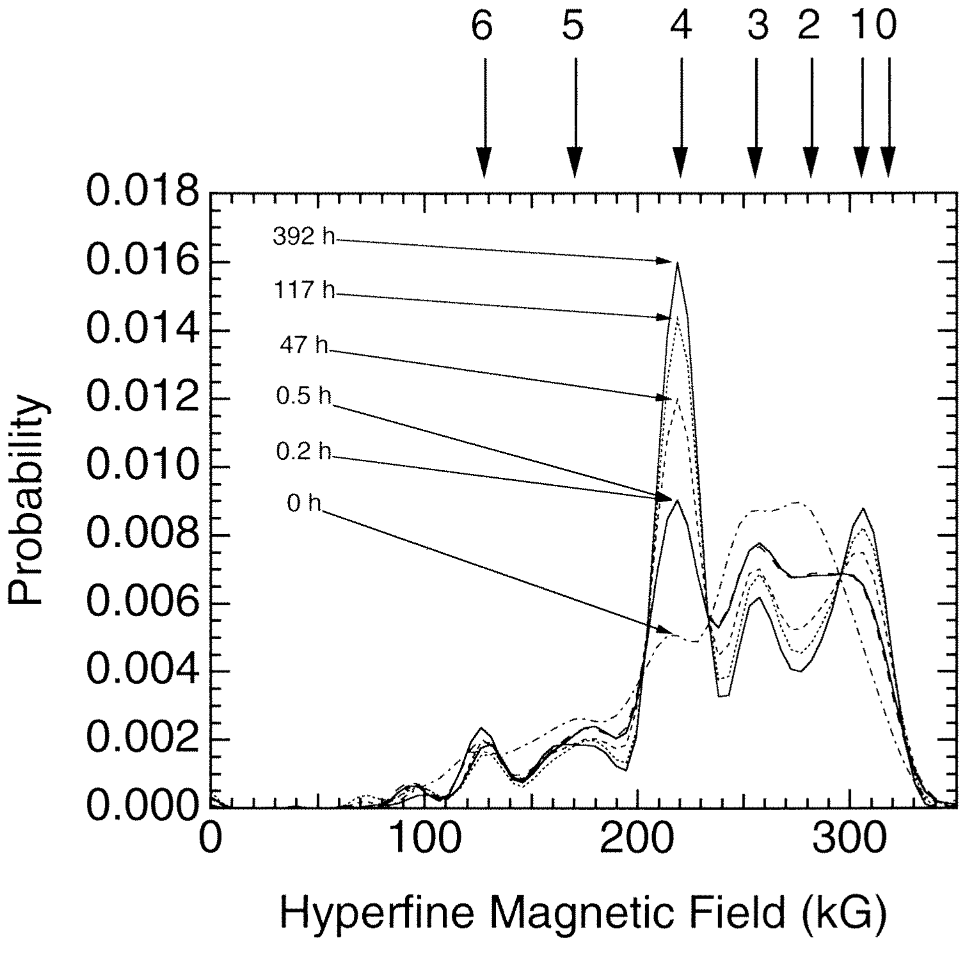

Figure 5.3: Hyperfine magnetic field distributions for Fe_3Al foils as piston-anvil quenched and after annealing at 300 °C for various lengths of time. The numbers at the top of the figure identify resonances from ^{57}Fe atoms with different numbers of Al neighbors [4].

the use of a vacancy mechanism of ordering. The presence of vacancies effectively introduces a third species, and contributes to the proliferation of state and path variables in the path probability method. More than that, however, the vacancy is unlike the other species (say, the A and B atoms in a binary alloy) in that it mediates the ordering process and therefore has to be given special treatment in the derivation of the rate equations. Removing this asymmetry in the formulation of the rate equations should greatly simplify matters. As a matter of fact, Mohri has successfully implemented the path probability method in the tetrahedron as well as octahedron approximations in fcc systems by using a pair exchange mechanism without the need for vacancies [6]. In going from the vacancy mechanism to the pair exchange mechanism, the number of species is reduced by one; but more importantly, the rate equations for the remaining species have a similarity of form, making them much easier to derive and implement.

Even though the analytical techniques presented in Chapter 2 are not as accurate as the Monte Carlo simulations of Chapters 3 and 4, they were able to provide provide us with much valuable insight. For instance, the relative ease with which we were able to calculate and visualize the free energy surface in the point approximation of Section 2.1 provided us with an intuitive thermodynamic interpretation of the occurrence of certain transient states during the evolution of order in an initially disordered alloy. In comparison, attempting to map out such a free energy surface as a function of the long-range order parameters in the case of the Monte Carlo simulations should prove to be a much more involved task, even assuming that such a free energy surface can be uniquely determined. One possible way of doing so would be to use the hybrid Monte Carlo–cluster variation method of Chapter 4. For a given set of interatomic potentials, we may choose different initial conditions for the alloy and thus obtain different kinetic paths in order parameter space. Since we are able to obtain an estimate of the free energy at any point along any of the kinetic paths, we can, in principle, map out at least a portion of the free energy surface as a function of the order parameters, specifically those regions of order parameter space that happen to be accessible via our kinetic paths.

It would be interesting to see how a free energy surface obtained in this manner compares to that obtained using a low order cluster approximation, such as the point approximation of Section 2.1. For instance, will we be able to associate the transient states obtained in Chapters 3 and 4 using Monte Carlo simulations with saddle points or other stationary points in such a free energy surface? To what extent will such a free energy surface depend on the choice of base clusters in the hybrid Monte Carlo–cluster variation method? In Section 1.2 we discussed how convexities in the equilibrium free energy function were suppressed as the order of the cluster approximation (the size of the base cluster) was increased, and vanished in the rigorous limit. Does a similar fate await the free energy surface obtained using the hybrid Monte Carlo–cluster variation method?

Extending the hybrid Monte Carlo–cluster variation method to even larger clusters on the bcc lattice, such as the 15-point stellated cube cluster, should improve the accuracy of the free energy estimates. The effect of the choice of base cluster sequences on the convergence of the free energy estimates is also worth investigating. It should also be relatively straightforward to apply the hybrid Monte Carlo–cluster variation method to other crystal lattices, such as the fcc, square, and triangle lattices.

References

[1] H. M. Rietveld, *Acta Cryst.* **20**, 508 (1966).

[2] L. Anthony and B. Fultz, *J. Mater. Res.* **4**, 1140 (1989).

[3] K. Oki, M. Hasaka, and T. Eguchi, *Jpn. J. Appl. Phys.* **12**, 1522 (1973).

[4] Z. Q. Gao and B. Fultz, "Transient B32-like order during the early stages of ordering in undercooled Fe_3Al," *Philos. Mag. B*, in press.

[5] R. Kikuchi, unpublished results.

[6] T. Mohri, *Acta Metall. Mater.* **38**, 2455 (1990).